DTU Library

Wave energy conversion in the Faroe Islands

Joensen, Bárdur

Publication date:
2023

Document Version
Publisher's PDF, also known as Version of record

Citation (APA):
Joensen, B. (2023). *Wave energy conversion in the Faroe Islands*. Technical University of Denmark. DCAMM Special Report No. S327

DTU Construct
Department of Civil and Mechanical Engineering

Wave energy conversion in the Faroe Islands

Bárdur Joensen

PhD Thesis

Wave energy conversion in the Faroe Islands

Bárdur Joensen
DTU Civil & Mechanical Engineering
Section of Fluid Mechanics, Coastal and Maritime Engineering
Technical University of Denmark

Main supervisor: Professor Harry B. Bingham
Co-supervisors: Associate Professor Bárdur A. Niclasen
Senior Engineer Jan Odmarsson

February 2023

Preface

This thesis is submitted as one of the requirements for obtaining the Doctor of Philosophy degree from the Department of Civil and Mechanical Engineering, Technical University of Denmark.

The work has been carried out in the period November 1st 2018 and February 28th 2023. The work has been carried out in the Section of Fluid Mechanics, Coastal and Maritime Engineering under the supervision of Professor Harry B. Bingham and at LBF Consulting Engineers in the Faroe Islands under the supervison of senior engineer Jan Odmarsson and Associate Professor Bárdur A. Niclasen from the University of the Faroe Islands, as part of the Faroese industrial Ph.D. Programme. Part of the work has been carried out during a research visit of three months at the Faculty of Science and Technology, University of the Faroe Islands, under the supervision of Associate Professor Knud Simonsen.

This thesis covers the main aspects of consideration when discussing the potential of wave energy conversion device deployment. The bulk of the thesis consists of five papers which I've first-authored - starting with numerical modelling tools and wave resource characterization, through wave energy conversion device evaluation, to experimental and numerical modelling of the hydrodynamics, while the closure deals with economic feasibility of wave energy conversion.

The financial support for this work was provided by the Research Council of the Faroe Islands (grant no. 02010), public utility company SEV, Betri Research Support Foundation, Bakkafrost Farming, Føroyagrunnurin, Faroese Metereological Institute, Hiddenfjord and MOWI Faroes.

Bárður Joensen
Tórshavn, February 2023

Acknowledgements

First of all I would like to thank my principal supervisor Harry B. Bingham for his support and immense guidance throughout this project, along with many fruitful discussions. I would also like to thank co-supervisors Jan Odmarsson and Bárður A. Niclasen for their support and guidance throughout the project. Furthermore, I would like to thank Robert W. Read from the Section of Fluid Mechanics, Coastal and Maritime Engineering, DTU Construct for his support and guidance regarding experimental and numerical modelling of wave energy converters. Also, Kim Nielsen from Rambøll for collaboration and many good discussions on wave energy. A thanks will go out to Jokin Brito Trevino for his contribution regarding the experimental measurements conducted during this project.

Thanks to all the Ph.D.'s and Post. Doc's from the Section of Fluid Mechanics, Coastal and Maritime Engineering for the many interesting and giving talks and discussions during our weekly cake club meetings.

A thanks to Knud Simonsen for his hospitality and advice during my research visit at the Faculty of Science and Technology, University of the Faroe Islands.

A very special thanks to my wife Rakul for her endless love and support throughout this project, without which I would not have finished this work. Also to my four sons - Óðin, Eiri, Askur and Bragi for being a constant reminder of the importance for doing research in renewable energy for a healthier and cleaner future planet.

Abstract

The need for developing robust and efficient technologies for capturing power from renewable energy sources grows by the minute as we see the damaging effects from greenhouse gas emissions and climate change. A potential candidate for this is wave power which has been deemed one of the more promising technologies for power capture as the amount of energy enclosed in ocean waves is tremendous.

The overall aim of this thesis is to explore the possibilities of using wave power for energy production in the Faroe Islands. This aim is approached by considering the key aspects for potential wave energy conversion device deployment.

The wave energy resource is assessed and characterized by use of third-generation spectral wave modelling for a large scale regional area. The numerical model is thoroughly validated through wave buoy observations and the wave energy resource is assessed in terms of spatial and temporal variability around the Faroe Islands.

The demonstration of various wave energy absorption technologies is evaluated for the coastal waters surrounding the Faroe Islands, while also considering key factors such as device type, device size and device deployment site.

An optimization strategy in the form of a non-return valve system is implemented for the existing wave energy conversion principle oscillating water column. This will enhance the power production and potentially lower the cost of energy.

An assessment in terms of economic feasibility is conducted for existing wave energy conversion technologies currently under development, in order to demonstrate the important aspect of economics and cost of energy when considering wave energy conversion device deployment. The cost of energy is the main factor when considering device deployment for energy extraction. Furthermore, this is an important aspect when considering competitiveness with other forms of renewable energy.

Results show that the waters around the Faroe Islands are high in wave energy density and the Faroe Islands are a suitable location for wave energy conversion deployment, both compared to other places in the world and compared to other offshore renewable energy sources.

Resumé

Der er et voksende behov for at udvikle robuste og effektive teknologier til at fange energien fra vedvarende energikilder, da vi ser de skadelige effekter fra udledning af drivhusgasser og klima forandringer. En potentiel kandidat for en sådan teknologi er bølgeenergi, som er anses for at være en af de most lovende teknologier for energi udvinding, fordi mængden af energi indesluttet i havbølger er enorm.

Det overordnede mål med denne afhandling er at udforske mulighederne for at bruge bølgekraft til energi produktion på Færøerne. Dette mål nås ved at overveje de vigtigste aspekter til installation af potentielle bølgeenergi konverteringsenheder.

Bølgeenergiressourcen vurderes og karakteriseres ved brug af tredje generations spektral bølgemodellering for et storskala regionalt område. Den numeriske model er grundigt valideret gennem bølgebøje observationer og bølgeenergiressourcen vurderes i forhold til rumlig og tidsmæssig variation omkring Færøerne.

Demonstrationen af forskellige bølgeenergi absorptionsteknologier evalueres for kystnære farvande omkring Færøerne, samtidig med at der tages højde for nøglefaktorer som f.eks enheders type, størrelse og implementeringssted.

En optimeringsstrategi i form af et kontraventilsystem implementeres for det allerede eksisterende bølgeenergikonverteringsprincip - oscillerende vandsøjle. Dette vil forbedre elproduktion og potentielt sænke energiomkostningerne.

Der foretages en vurdering med hensyn til økonomisk gennemførlighed for eksisterende bølgeenergikonverterings teknologier i øjeblikket under udvikling, for at demonstrere det vigtige aspekt omkring økonomi og energiomkostninger, når man overvejer at implementere bølgeenergi. Omkostningerne til energi er den vigtigste faktor, når man overvejer enhedsimplementering til energiudvinding. Dette er desuden et vigtigt aspekt, når man tænker på konkurrencedygtighed med andre former for vedvarende energi.

Resultater viser, at farvandene omkring Færøerne har høj bølgeenergitæthed og Færøerne er et velegnet sted for bølgeenergikonvertering, både sammenlignet med andre steder i verden og sammenlignet med andre offshore vedvarende energi kilder.

Contents

Chapter 1

Introduction

1.1 Motivation

As the world's population continues to grow, the energy demand will follow this same growth. Together with the damaging effects from green house gas emissions, there is a need for alternatives to fossil fueled energy sources. These alternative, renewable energy sources come in many different varieties: wind energy, solar energy, tidal energy, hydro power, ocean thermal energy and wave energy. The one thing all of these sources have in common is that they are all generated from the Earth's natural physical processes.

The wind energy industry and solar power industry have experienced rapid growth over the past years [1] and hydro power is a well established technology proven to be efficient for electricity production [2].

As the world society intends to moves from stable energy production from fossil fuel energy sources to unstable renewable energy sources, there is a need to invest a lot of effort in stabilizing the electricity which is fed into the electrical grid. However, Ref [3] shows that a reasonable distribution of renewable energy sources leads to a more stable electricity generation.

A potential candidate to include in the renewable energy mix is wave energy. The amount of energy contained in ocean waves is vast and this has been classified as one of the most promising renewable energy sources [4, 5]. These aforementioned references have both mapped out the global distribution of wave energy. Both studies have shown that the particular hot spots for wave energy are located in the Pacific Northwest, Northeast Atlantic Ocean, south coast of Australia, South Indian Ocean and the South Pacific Ocean.

Many studies have attempted to analyze and characterize the wave energy potential for the possibility of wave energy converter deployment. Ref. [6] reviews the most recent resource characterizations from observations (in situ and satellite) and refined numerical simulations specifically dedicated to wave power assessments. However, there is no mention of any studies involving the wave resource characterization of the Faroe Islands.

Being located in the middle of the Northeast Atlantic Ocean, the Faroe Islands could prove a viable candidate for the world's first commercial utility scale wave energy farm. One attempt has been made in the past in order to implement wave energy in the electricity generation in the Faroe Islands, e.g. the SeWave project [7], but this was never realised. As part of the front-end-engineering-design (FEED), the wave power resource was characterized around the Faroe Islands, in a somewhat simple manner - with four offshore wave buoys [8] and a simple procedure to transfer waves from offshore to nearshore.

The wave climate around the Faroe Islands has been assessed earlier in [9]. However, the focus of this study was aimed at operational safety of vessels around the Faroe Islands, so mainly the wave heights were presented here and no information of wave periods or wave power.

Fundamental knowledge about the Faroe Islands' suitability for wave energy converter device deployment is thus still lacking, which has inspired this thesis.

1.1.1 Contributions and Novelty

The novel contributions of this Ph.D. dissertation are as follows:

- An assessment of the capability of the spectral wave model MIKE 21 SW to capture the nonlinear physical processes for waves travelling from deep to shallow water, by comparison with the fully nonlinear potential flow wave model OceanWave3D.
- An assessment of the wave power potential around the Faroe Islands by use of numerical spectral wave model and validated by wave measurements.
- Evaluation of the performance of wave energy converters in Faroese coastal waters building on the main working principles of wave energy absorption. Furthermore, the importance of careful site investigation before wave energy conversion device deployment is emphasized.
- Experimental and hydrodynamic analysis of a novel oscillating water column wave energy conversion concept, only utilizing half of the wave cycle in order to obtain higher absorbed power compared to the conventional oscillating water column concept.
- Estimate of the levelised-cost-of-energy, annual energy production and the capacity factor in Faroese waters for a number of wave energy conversion devices currently under commercial development.

Each of the above mentioned contributions roughly correspond to one of the papers presented in the thesis.

1.2 Background

This section will provide an overview regarding the research and development efforts within the sub-branches in the wave energy conversion industry. In order to avoid too much repetition, this background section will provide an overview of the different aspects considered in this thesis, as each of the papers contains a literature review addressed at each of the respective subjects of the papers.

Wave resource characterization

The world's oceans have been a food source for fishermen and have been important trade routes for several thousand years. Recently the oceans have become an important source for energy. Necessary information on the dynamics of the oceans is therefore of crucial importance. In [10] a nice overview is given over the historical timeline of the study of ocean wave dynamics, where some studies mentioned date all the way back to Aristotle in ancient Greece, up to Leonardo da Vinci in the Renaissance and to Benjamin Franklin in the United States in the late 1700's. Furthermore, interest in wave predictions vastly grew during World War II due to the practical need of knowledge on sea states during landing operations. Based on the work of Sverdrup and Munk [11] the first operational wave predictions introduced a parametric description of the sea state and used empirical wind sea and swell laws. Advances continued with the work of Pierson et. al. [12] by introduction of the wave spectrum and the work of the JONSWAP project group [13] by introduction of fetch-limited wave spectra. The work of the WAM group [14] resulted in the development and implementation of the third-generation spectral wave model WAM [15], which laid the foundation for the development of other versions of third-generation spectral wave models, e.g. SWAN [16], WaveWatch III [17], MIKE 21 SW [18] and TOMAWAC [19]. These models are widely used tools for wave resource characterization.

The attention towards exploitation of ocean wave energy received considerable attention after the first oil crisis in 1973, where a lot of research and development was conducted to effectively utilize this vast energetic resource [20]. In the publication of Stephen Salter's spine duck [21] the author reports a scatter diagram of the distribution of wave heights and wave periods from observations along with a parametric calculation of the wave power. In [22] the author discusses the potential of wave power and the methods to harness this energy source. The wave power potential is assessed through observations. At the IUTAM Symposium held in Lisbon, Portugal in 1985 [23], many of the papers involve the assessment and characterization of the wave power resource for energy exploitation. In [24] the author discusses some of the assessments made, mostly in Europe, in order to characterize the wave energy resource. The types of assessments all rely on direct measurements of wave heights and periods in the ocean, or from the measurement of wind speed and subsequent prediction of wave height and period. In [25] the authors developed an atlas for the European offshore wave energy resource by use of wave data implemented in the routine operation of the European Centre for Medium Range Weather Forecasts (ECMWF), in addition to directional wave measurements from the Norwegian offshore waters. In [26] a nice overview is given the different techniques available for characterizing the wave energy resource.

Studies concerning wave resource characterization, have received a great deal of attention in the past and still are. The numbers of publications of these types of studies emphasize this. In [6] the authors gathered all literature associated with wave energy estimation from use of numerical wave models, with a special attention to scientific studies that integrated an extended description of the calibration and validation procedures. Here they found over one hundred publications, while the authors also provide a graph showing the distribution among these studies in terms of their regional focus, with a European regional focus the leading continent in this regard with 58%.

In [27] the authors give a review of wave energy resource assessment studies conducted for the Mediterranean Sea, and here there are found to be as many as 34 only for the Mediterranean - some focus on parts of the Mediterranean, while others focus on the entire Mediterranean Sea.

A brief search on the popular search engines within scientific publications, for the keywords ”wave energy assessment”, ”wave resource assessment” and ”wave power assessment” yields several hundreds of publications, highlighting the large interest in this area of energy exploitation.

Given all of these conducted studies regarding the characterization of wave resource for wave energy exploitation, none exist for the waters surrounding the Faroe Islands.

Wave energy conversion device research and development

The first recorded attempt aimed at producing energy from ocean waves dates all the way back to 1799 when the first patent was filed for extracting energy from ocean waves [28]. Although the idea dates all the way back to the end of the 18th century, this type of energy conversion technology did not receive considerable attention until 1947 when the Japanese started to construct ocean buoys for navigation powered from the energy from waves [29], under the supervision of Yoshio Masuda, a Japanese naval officer. However, *Scientific American* reported in 1885, that there were 34 whistling buoys operating along the U.S. coast, operating through the oscillating water column (OWC) concept [29]. The work of Masuda in the mid 1940's resulted in a later commercialization of the navigational buoys in 1965 in Japan [30].

As mentioned earlier, following the first oil crisis in 1973, research and development around wave energy received a considerable boost by an article by Dr. Stephen Salter published in the scientific journal *Nature* in 1974 [21]. This article described a rather innovative design of a pitching terminator wave energy device, which was able to absorb about 80 % of the incident wave power. Following the intense efforts in research and development in wave energy conversion devices, the following two decades experienced a reduction in the efforts, which was then followed by renewed interest in the beginning of the current millennium [20].

Many books and review papers have been published with the focus on research and development within the wave energy sector, both in terms of wave resource characteristics, but mainly also on hydrodynamics and performance of devices and their implementation in the energy mix. Examples of these are [28], [26], [20] and [31]. In [32] the author describes the many mathematical and physical aspects of wave energy converter modelling, with a sharpened focus on oscillating water columns. A review on the hydrodynamic modelling technologies of wave energy conversion is given in [33]. The author discusses the fundamental understanding of wave energy conversion, the reliablility of numerical and experimental modelling techniques for wave energy converters, and how to optimize the power-take-off to maximize power absorption.

In [31] the author discusses the many aspects of wave energy conversion, with a high focus on hydrodynamic modelling, model testing and control. Furthermore, the author discusses the wide variety of wave energy technologies, and identifies the many different ways in which energy can be absorbed from waves. He states that in recent reviews, as many as about one hundred wave energy projects are currently at various stages of development. Ref. [31] discusses the different main working principles of wave energy conversion devices, which I also will briefly present here: Oscillating water column, wave activated bodies and overtopping devices, where they all contain different deployment types. The oscillating water columns and wave overtopping devices can be fixed structures offshore, on the coastline or integrated into breakwaters. Alternatively, they can be deployed as floating offshore structures. The wave overtopping devices can be deployed in the same manner as the oscillating water column. The wave activated bodies are mainly deployed as three different categories - attenuator, terminator or point absorber. The attenuator devices are usually in length of about half the wavelength to one wavelength and oriented perpendicular to the incoming wave fronts. Wave terminator devices are usually also long devices, but are oriented parallel to the incoming wave front. Point absorbers are small compared to the incoming wave length and most often can absorb power from waves coming from all directions. The attenuator and terminator devices are directionally dependent, while the point absorbers are not.

From the above mentioned wave energy converter types, the oscillating water column (OWC) is probably the one which has received the most attention [34] and is one of the more promising types. This is further emphasized by the number of review works available on oscillating water columns, e.g. [35], [29], [36], [37], [38] and [39]. Along with these review papers the early attention towards oscillating water columns, which was mentioned in the beginning of this section, where whistling buoys operating on the oscillating water column principle were active along the U.S. coast in 1885. Furthermore, in the trough era and explosion era of wave energy conversion defined in [40] the majority of the full scale operating deployed wave energy conversion devices were based on the oscillating water column principle. These devices were the Kværner column in Norway [41], the OSPREY OWC [42], the Pico OWC plant in the Azores [43], the LIMPET plant [44], the Mutriku OWC wave power plant [45] to name a few.

In the fourth paper of this thesis [46] we give a review on the many different efforts that have been made in order to improve the efficiency of oscillating water columns. The big advantage of the oscillating water column, is that is does not have any moving parts submerged in the water. However, one of the drawbacks is the efficiency of the turbines usually equipped in oscillating water columns as these have generally a low efficiency. The Wells turbine, invented by Dr. Arthur Wells in 1976 [47], is probably the most widely used type of air turbine for oscillating water columns. However, a popular alternative to the Wells turbine is the impulse turbine patented in 1975 by Ivan A. Babintsev in 1975 [48] as mentioned in [35]. Although the oscillating water column has many attractive features, the complex design of the air-turbines proves it to be difficult for this type wave energy converter to really kick off to commercialization.

The improvements proposed for oscillating water columns have often focused on the improvement of the air turbines used for electricity generation [49], [50] and [51]. Some have also focused on the geometric outlay of the oscillating water column itself, with [52] and [53] proposing the use of U-shaped column chambers to improve the efficiency of the device. In [54] the authors propose three different alterations of the main geometry of the oscillating water column in order to improve efficiency, compared to the conventional geometric design. One of the designs led to a significant improvement of the absorbed power of the device. Furthermore, in [55] the authors propose a more streamlined design in an inclined wall oscillating water column.

The idea of introducing non-return valves in the design of oscillating water columns has also been introduced. Some examples of such devices are the LEANCON device [56] and the Seabreath device [57]. The motivation behind the introduction of the non-return valves is to improve the overall efficiency of the device by rectifying the air flow. Other examples are the Tupperware device [58] and [59], which is a floating spar-buoy type oscillating water column device, with a low pressure and a high pressure chamber in extension to the conventional type, with a uni-directional turbine and a non-return valve. One device currently under commercial development, UniWave200, developed by Wave Swell Energy [60] also incorporates non-return valves and uses a unidirectional air turbine as the power-take-off. Some scientific works have been published regarding this type of device, e.g. [61], [62] and [63]. The development of the UniWave200 device and the preliminary results on this device from this references found that the one-way energy absorption strategy can absorb more power compared to the conventional energy absorption strategy. This work has largely inspired the work covered in the fourth paper [46]. The works published around the UniWave200 device rely on experimental modelling and only incorporating one of the half-cycles of the wave, whereas we in [46] have done experimental modelling on both half-cycles and compared to conventional two-way power absorption. Furthermore, we have compared these experimental results with numerical calculations performed in the frequency domain and the time domain.

Economic feasibility of wave energy converters

The economic feasibility of wave energy converters is a topic which has not received the same level as attention as the two above. However, some studies have been conducted in the past in order to determine whether it is feasible for wave energy conversion to be part of the renewable energy mix. Furthermore, some reviews have been published as well to underline the importance of considering the economical aspects of wave energy converters before deployment.

An important aspect to consider when discussing the potential wave energy conversion device deployment is the economic angle of this sort of project. If a commercial project is to be considered, it is of great importance to drive the cost of energy as far down as possible. In [20] the authors give a good overview on the different aspects to consider which are associated with the economic assessment of wave energy devices.

Some early reviews on the economics of wave energy have been published. In [64] the authors analyze the economics of wave energy and reach to the conclusion that the economic prospects of wave energy are poor, both compared to other renewable energy plants and thermal plants using fossil fuels. The wave energy sector has come a long way since this was published in 1984 and there have been improvements on the cost calculation models, along with the optimization of the devices considered. In [65] the author analyzes the technical and non-technical aspects involved in wave energy conversion, with some focus on the economics of wave energy converters. Here some promising results are presented in terms of cost of energy for wave energy converters.

In [66] the authors give a review of the economics of wave energy by exploring the different aspects involved when considering wave energy device deployment. They concluded that a potential wave energy conversion farm would only be economically viable through subsidies.

In [67] the authors propose a guidance for the economic assessment of wave energy devices at early development stages, where they analyze all the possible aspects included in the economic calculation of a wave energy project. Furthermore, they propose a strategy in order to meet a certain levelised-cost-of-energy target.

In the fifth paper [68] we give a review of the existing studies directly related to the economic feasibility of wave energy conversion deployment. Studies exist for many places around the globe and the results vary from place to place. While some studies are performed in neighbouring regions to the Faroe Islands, none exist for the waters around the islands. This emphasizes the need for undertaking the type of work which is done in the fifth paper.

1.3 Problem statement

As can be seen from the background search regarding the different aspects of wave energy conversion, no studies directly relate to wave energy conversion device deployment in the Faroe Islands. This leads to the following main research question:

- *Are the Faroe Islands a suitable location for consideration of wave energy conversion deployment?*

This main research question will be answered through the following five specific research questions:

- *What tool can be used to describe the transformation of waves from deep to intermediate or shallow water in order to characterize the wave climate around the Faroe Islands, while capturing the important physical effects associated with this transformation?*
- *What is the wave power potential around the Faroe Islands, in terms of overall wave energy flux, along with the spatial and temporal variability of wave energy flux?*
- *How does the performance of various wave power devices vary in terms of deployment location and size in the Faroe Islands?*
- *Which strategies can be used in order to optimize and improve existing technologies to enhance power production and lower the costs?*
- *How economically feasible are currently developed wave energy conversion devices in Faroese waters?*

The posted research questions will be answered through the papers presented in the following section.

1.4 Outline

The bulk of this thesis consists of a collection of papers which I have first-authored. Their publication status is indicated as they are presented in the following. Each paper stands as a chapter in itself and to make the papers more digestible, a short description of each of the papers is given in the following, along with their connection with each other and the most important conclusions.

The first paper (under review as Joensen and Bingham [69]) is presented in chapter 2 and compares the third-generation spectral wave model MIKE 21 SW [18] (used in the second paper in chapter 3) with the fully nonlinear potential flow wave model OceanWave3D [70]. The aim is to compare how well the spectral wave model captures the nonlinear physical processes as waves travel from deep to shallow water. Both models are forced with a JONSWAP wave spectrum, with the wave spectrum directly implemented in the boundary condition of the spectral wave model, while in the OW3D model an irregular wave time-series is constructed and introduced at the boundary.

The second paper (published as Joensen et. al. [71]) presented in chapter 3, deals with assessing the wave climate around the Faroe Islands with a special focus on wave power through large scale spectral wave modelling, thoroughly validated by physical wave buoy observations. The study shows that the spectral wave model is capable of representing the wave climate around the Faroe Islands accurately. Furthermore, the wave climate around the islands is harsh with fairly large wave heights and contains large amounts of wave energy. This leads to the conclusion that the waters around the Faroe Islands are well suited for wave energy conversion deployment. The wave energy assessment in this study will provide the basis for the evaluation of wave energy absorption concepts analyzed in the third and fifth papers.

The third paper (published as Joensen et. al. [72]) presented in chapter 4, evaluates the power performance of different wave energy conversion concepts potentially suitable for deployment in Faroese coastal waters. The focus of the paper is to analyze the power performance in terms of size and scaling at different locations around the Faroe Islands. We here looked at four concepts which are representative of a majority of the wave energy converters being developed worldwide, i.e. the majority of working principles are considered here. Furthermore, we chose devices where their capture-width-ratios (non-dimensional power absorption) were represented as functions of wave period or wave frequency in existing literature. This way it was possible to upscale the size of the devices by evaluating their performance as a function of the size of the respective devices at each analyzed location. We concluded here that the output power from two devices of the same size could vary from location to location. Also, that a careful site investigation is needed prior to any wave energy device deployment.

The fourth paper (under review as Joensen et. al. [46]) presented in chapter 5, deals with the hydrodynamic analysis of a novel concept oscillating water column, which utilizes one-way energy absorption contrary to the conventional two-way energy absorption. The rationale for giving such special attention to oscillating water column wave energy devices is two-fold: 1) the oscillating water column working principle is known in the company (LBF Consulting Engineers), and 2) the power-take-off system of an oscillating water column has no moving parts submerged in the water, which is also mentioned in the paper, being an advantage for potential deployment in Faroese waters which contain large extreme waves. Implementing a valve system, proved to increase the power absorption in the numerical calculations compared to having no valve, while the experiments did not show this same increase in power absorption.

The fifth paper (under review as Joensen et. al. [68]) presented in chapter 6, analyzes the economic feasibility of nine different wave energy conversion principles currently under development for nine potential deployment sites in the Faroe Islands. The analyzed wave energy conversion devices perform at different levels - both in terms of energy production, but also in terms of cost of energy. Furthermore, the suitability of each device deployment is highly location dependent.

In the last chapter an overall conclusion of this thesis is given.

Apart from the presented papers above, the author has first-authored and co-authored the following papers during the PhD project:

- Bárdur Joensen et al. "Performance predictions of one-way energy capture by an oscillating water column device in Faroese waters". In: *Proceedings of the 14th European Wave and Tidal Energy Conference.* Ed. by D.M. Greaves. ISSN: 2309-1983. 2021

- M. Rosati et al. "A data-based modelling approach for a vented oscillating water column wave energy converter". In: *Trends in Renewable Energies Offshore.* Ed. by C. Guedes Soares. Marine Technology and Ocean Engineering Series. Proceedings of the 5th International Conference on Renewable Energies Offshore (Renew 2022). CRC Press, 2023, pp. 339–350. ISBN: 978-1-032-42003-5

Chapter 2

Comparison of a spectral wave model with a fully nonlinear potential flow wave model

The paper entitled ”Comparison of a spectral wave model with a fully nonlinear potential flow wave model” has been submitted to journal of Ocean Engineering as:

Bárdur Joensen and Harry B. Bingham. “Comparison of a spectral wave model with a fully nonlinear potential flow wave model”. Submitted.

Comparison of a spectral wave model with a fully nonlinear potential flow wave model

Bárður Joensen[a,b,*], Harry B. Bingham[b]

[a] LBF Consulting Engineers, Niels Finsensgøta 10, FO-110 Tórshavn, Faroe Islands
[b] Technical University of Denmark, Department of Civil & Mechanical Engineering, Section for Fluid Mechanics, Coastal and Maritime Engineering, Nils Koppels Allé building 404, 2800 Kgs. Lyngby, Denmark

Abstract

This study evaluates the performance of the MIKE 21 Spectral Wave (SW) model by comparing the evolution of the spectrum with the fully nonlinear potential flow model OceanWave3D. We test only the shoaling, nonlinear wave-wave interaction and whitecapping terms by considering a two-dimensional shoaling problem on a mild slope bottom without wind, or bottom friction effects and before reaching the breaking zone at the beach. A JONSWAP spectrum is introduced at the deep-water boundary and allowed to propagate freely up to a relatively shallow shelf. The peak wave is in relative water depth $kh = 4$ at the deep water boundary where $k = 2\pi/\lambda$ is the wave number, λ the wavelength and h the water depth. For the peak relative water depth less than about $kh = 0.8$, the spectrum agrees well with the fully nonlinear results, but below this value significant differences appear. In particular, the long-wave difference frequency effects are mostly absent, indicating a need for improvement in the triad interaction model.

Keywords: Numerical modelling, ocean waves, spectral wave model, fully-nonlinear potential flow model

1. Introduction

Accurate representation of physical wave parameters is crucial for a number of ocean engineering applications - design of offshore and coastal structures, coastal protection, offshore wind turbine foundations, wave energy covnerters, etc. Many different wave models have been utilized in the past to accurately represent the physical parameters associated with wave-structure interaction. Usually, these numerical models are compared to physical model scale experiments to verify and validate the physical processes. Apart from this, many studies have relied on comparing different numerical wave models to see how well these capture the physics.

In [1] the authors use two spectral wave models - MIKE 21 SW [2] and SWAN [3] - together with observations to evaluate the accuracy of the models by analysing waves in an estuary with three detached breakwaters at the mouth of the estuary. The authors found that the models were consistent with the observations during storms. Ref. [4] evaluated two third generation spectral wave models, SWAN and WaveWatchIII (WWIII) [5] for the characterization of the wave energy resource off the coast of Oregon, USA. Both models performed well at the test bed site and exhibited similar modelling fidelity.

In [6] the authors compare the wave field behind single wave energy converters and multiple wave energy converters (WECs), generated by the spectral action balance code, SNL-SWAN [7] to the linear wave boundary element method code WAMIT [8]. The authors assess the performance of the two wave models, both in

*Corresponding author
Email address: bajoe@mek.dtu.dk (Bárður Joensen)

the near-field behind the WECs and the far-field behind the WECs. According to this study, the difference between the two models in the near-field is relatively large, while in the far-field the difference is minimal.

In [9] the authors compare the performance of two spectral wave models, MIKE 21 SW and SWAN, for wave hindcasting in the MacKenzie Delta, Canada. The authors found that the two models were in agreement for the investigated study area.

Ref. [10] compared three third generation spectral wave models, MIKE 21 SW, SWAN and STWAVE [11], for modelling wave conditions along the coast of Portugal. The results show that the models have a similar behavior and are statistically comparable.

In [12] the authors compare the performance of three wave models, with different types of governing equations - REF/DIF S [13], SWAN and MIKE 21 BW - where SWAN is a phase averaging model and REF/DIF S and MIKE 21 BW are phase resolving models. SWAN uses the wave action balance equation, REF/DIF S uses the parabolic mild-slope equation and MIKE 21 BW uses Boussinesq-type equations. The authors compared the numerical models with experimental measurements and found that MIKE 21 BW showed the best performance, where the other two models showed discrepancies compared to the experiments.

Apart from comparing different numerical models, a lot of research has been done in comparing wave models with wave measurements - especially spectral wave models compared to measurements. In general, the third-generation formulations of the spectral wave models tend to be statistically in agreement with the measurements. Some examples of studies of this type are [14], [15], [16], [17] and [18]. In general, the results from these studies show that the numerical models are capable of capturing the physics at an acceptable level. While these studies all focus on large-scale regions, a number of studies have also been conducted on smaller scale regions using deterministic models to represent the physical processes in ocean waves. Here the scale is typically limited by the relatively large computational effort to run these types of models [19, 20] In a recent study by [21] relatively large-scale wave transformation in a Norwegian fjord is computed using the fully nonlinear potential flow wave model REEF3D:FNPF [22]. Comparison of the spectral parameters is also made to predictions using the spectral wave model SWAN.

1.1. Contributions and Novelty

In this paper we test the ability of the spectral wave model MIKE 21 SW [23] to capture shoaling-induced nonlinear wave-wave interaction by comparing calculations with the fully nonlinear potential flow wave model OceanWave3D [24, 25]. The main objective here is to use a simple two-dimensional (2D) shoaling test case to compare the development of the wave energy spectra predicted by the two wave models as an irregular wave train travels from deep to shallow water. To our knowledge this type of comparison study has not been conducted in the past. By comparing the evolution of the wave energy spectrum at 12 different water depths, we are able to identify limitations in the accuracy of the nonlinear source terms in the spectral wave model. This highlights a need for improved models to capture triad interaction effects in shallow water.

2. Numerical models

2.1. Test domain

In this fairly simple comparison study analysis, the study area is a 2D model domain with deep water conditions at the left end and gradually shifting towards shallow water conditions, when moving from left to right, see Fig. 1.

2.2. MIKE 21 SW

When modeling waves at scales where instationary wave growth is important, the standard approach is to use spectrally averaged wave models. These models predict the growth, transformation and decay of ocean waves, due to their interaction with ocean surface winds and bathymetry. In the present study, such a

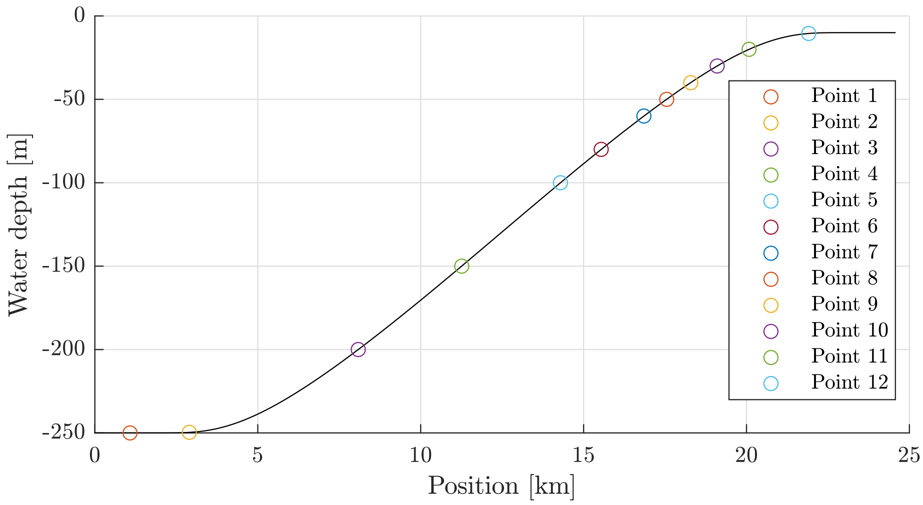

Figure 1: Model domain together with the comparison points.

spectral wave model is used. The underlying concept of spectral wave models is the energy balance equation, where the evolution of the wave spectrum is given by:

$$\frac{\partial E}{\partial t} + \frac{\partial}{\partial x}(c_x E) + \frac{\partial}{\partial y}(c_y E) + \frac{\partial}{\partial \sigma}(c_\sigma E) + \frac{\partial}{\partial \theta}(c_\theta E) = S_{tot} \tag{1}$$

where $E(\sigma, \theta)$ is the wave energy spectrum, t is time, σ is the intrinsic angular frequency, θ is the wave direction, c_x and c_y are the propagation velocities in the geographical space, while c_σ and c_θ are the propagation velocities in the spectral space. The first term represents the local rate of change of energy density in time. The second and third terms represent the geographic propagation of energy density in the (x,y)-space. The fourth term represents the shifting of the frequency due to depth variations, and the fifth and last term is related to depth-induced refraction with propagation velocity c_θ in the θ-space. In short, the left hand side of equation (1) constitutes the propagation of a large sum of independent linear waves.

The right hand side of Equation (1) represents the effects of generation, dissipation, and nonlinear wave-wave interaction. The total source term is expressed as

$$S_{tot} = S_{in} + S_{nl} + S_{ds} + S_{bot} + S_{surf} \tag{2}$$

where S_{in} is the momentum transfer of wind energy to wave generation, S_{nl} is the nonlinear wave-wave interaction (triad and quadruplet), S_{ds} is the dissipation of energy due to white-capping, S_{bot} is the dissipation of energy due to bottom friction and S_{surf} is the dissipation of energy due to depth-induced wave breaking. In deep water the evolution of the spectrum is dominated by the balance between S_{in}, S_{ds} and the quadruplet part of S_{nl}. In shallower water the triad part of S_{nl}, S_{bot} as well as S_{surf} become increasingly important parts of the evolution. The input term S_{in} works at all depth ranges, increasing the amplitudes of wave components traveling in a similar direction to the wind, but with lower phase speeds.

The MIKE 21 SW [23] model discretizes the governing equations in geographical and spectral space using a cell-centered finite volume method. In the geographical domain an unstructured mesh technique is used. The time integration is performed using a fractional step approach where a multi-sequence explicit method is applied for the propagation of wave action [2].

The source functions S_{in}, S_{nl}, and S_{ds} are similar to those in the WAM Cycle 4 model [26]. The wind input is based on Janssen's ([27], [28]) quasi-linear theory of wind-wave generation, where the momentum transfer from the wind to the sea not only depends on the wind stress, but also on the sea-state. The quadruplet wave-wave interaction is based on the computationally efficient Discrete Interaction Approximation (DIA) proposed in [29] and the S_{ds} term is based on the formulation of white-capping in [26]. The triad wave-wave interactions state a resonance condition which requires that the sums of frequencies and wave-number vectors of two freely propagating wave components are equal to the frequency and wave number, respectively, of a third freely propagating wave component:

$$f_1 + f_2 = f_3 \tag{3a}$$

$$\overrightarrow{k_1} + \overrightarrow{k_2} = \overrightarrow{k_3} \tag{3b}$$

In the MIKE 21 SW model the triad-wave interaction is modelled using the simplified approach proposed by [30, 31]. In spectral form this is:

$$S_{nl}(\sigma,\theta) = S_{nl+}(\sigma,\theta) + S_{nl-}(\sigma,\theta) \tag{4}$$

where

$$S_{nl+}(\sigma,\theta) = \max(0,\ \alpha_{EB} 2\pi c_g J^2 |\sin(\beta)|(cE^2(\sigma_-,\theta) - 2c_- E(\sigma_-,\theta)E(\sigma,\theta)) \tag{5}$$

$$S_{nl-}(\sigma,\theta) = -2S_{nl+}(\sigma_+,\theta) \tag{6}$$

For a more detailed description of the different terms in the above equations, the reader is refered to [32].

In order to focus on the accuracy of the nonlinear and white capping term, we turn off wind forcing and bottom friction and only consider the spectral evolution before the wave reaches the surf zone.

2.3. OceanWave3D

OceanWave3D is an open source, high-order finite difference solution of the fully nonlinear potential flow formulation for surface wave propagation on a variable depth fluid [33]. Full details and analysis of the method can be found in [24, 25], so here we only provide a brief outline.

A Cartesian coordinate system is adopted with the xy-plane located at the still water level and the z-axis pointing upwards. The still water depth is given by $h(\mathbf{x})$ with $\mathbf{x} = (x, y)$ the horizontal coordinate. The position of the free surface is defined by $z = \eta(\mathbf{x}, t)$ and the gravitational acceleration $g = 9.81$ m^2/s is assumed to be constant. Assuming an inviscid fluid and an irrotational flow, the fluid velocity $(\mathbf{u}, w) = (u, v, w) = (\nabla\phi, \partial_z\phi)$ is defined by the gradient of a scalar velocity potential $\phi(\mathbf{x}, z, t)$, where $\nabla = (\partial_x, \partial_y)$ is the horizontal gradient operator. The evolution of the free surface is governed by the kinematic and dynamic boundary conditions

$$\partial_t\eta = -\nabla\eta\cdot\nabla\tilde{\phi} + \tilde{w}(1+\nabla\eta\cdot\nabla\eta), \tag{7a}$$

$$\partial_t\tilde{\phi} = -g\eta - \frac{1}{2}(\nabla\tilde{\phi}\cdot\tilde{\phi} - \tilde{w}^2(1+\nabla\eta\cdot\nabla\eta)), \tag{7b}$$

which are expressed in terms of the free surface quantities $\tilde{\phi} = \phi(\mathbf{x}, \eta, t)$ and $\tilde{w} = \partial_z\phi|_{z=\eta}$. To find $\tilde{w}$ and evolve these equations forward in time requires solving the Laplace equation in the fluid volume with a known $\tilde{\phi}$ and η, together with the kinematic bottom boundary condition

$$\phi = \tilde{\phi}, \qquad z = \eta, \tag{8a}$$

$$\nabla^2\phi + \partial_{zz}\phi = 0, \qquad -h \le z < \eta, \tag{8b}$$

$$\partial_z\phi + \nabla h\cdot\nabla\phi = 0, \qquad z = -h. \tag{8c}$$

At the structural boundaries of the domain, the flow field must be everywhere parallel to the boundary surfaces, implying that the velocity potential ϕ must satisfy the no-normal flow condition (expressed here in physical coordinates)

$$\mathbf{n}\cdot(\nabla, \partial_z)\phi = 0, \qquad (\mathbf{x}, z) \in \partial\Omega, \tag{9}$$

where $\mathbf{n} = (n_x, n_y, n_z)$ is an outward pointing normal vector to the solid boundary surfaces $\partial\Omega$. It is assumed that all structural boundaries except the fluid bottom are vertical and aligned with one of the horizontal coordinates, but the extension to general boundaries is implementation-wise conceptually identical to the treatment of the bottom boundary.

Since the free surface is a time-dependent moving boundary with an *a priori* unknown position, it is convenient to make a change of variable in the vertical which maps the solution to a time-invariant domain using the following (non-conformal) σ-coordinate transformation

$$\sigma \equiv \frac{z + h(\mathbf{x})}{\eta(\mathbf{x}, t) + h(\mathbf{x})} \equiv \frac{z + h(\mathbf{x})}{d(\mathbf{x}, t)}. \tag{10}$$

The Laplace problem in the transformed computational domain becomes

$$\Phi = \tilde{\phi}, \quad \sigma = 1, \tag{11a}$$

$$\nabla^2\Phi + \nabla^2\sigma(\partial_\sigma\Phi) + 2\nabla\sigma \cdot \nabla(\partial_\sigma\Phi) + (\nabla\sigma \cdot \nabla\sigma + (\partial_z\sigma)^2)\partial_{\sigma\sigma}\Phi = 0, \quad 0 \leq \sigma < 1, \tag{11b}$$

$$(\partial_z\sigma + \nabla h \cdot \nabla\sigma)(\partial_\sigma\Phi) + \nabla h \cdot \nabla\Phi = 0, \quad \sigma = 0, \tag{11c}$$

where $\Phi(\mathbf{x}, \sigma, t) = \phi(\mathbf{x}, z, t)$ and the derivatives of the coordinate σ can be written as

$$\nabla\sigma = \frac{1-\sigma}{d}\nabla h - \frac{\sigma}{d}\nabla\eta, \tag{12a}$$

$$\nabla^2\sigma = \frac{1-\sigma}{d}\big(\nabla^2 h - \frac{\nabla h \cdot \nabla h}{d}\big) - \frac{\sigma}{d}\big(\nabla^2\eta - \frac{\nabla\eta \cdot \nabla\eta}{d}\big) - \frac{1-2\sigma}{d^2}\nabla h \cdot \nabla\eta - \frac{\nabla\sigma}{d} \cdot (\nabla h + \nabla\eta), \tag{12b}$$

$$\partial_z\sigma = \frac{1}{d}. \tag{12c}$$

Note that all of these nonlinear coefficients can be determined from the known free surface and bottom positions. In the σ-coordinates, the structural boundary conditions takes the form

$$\mathbf{n} \cdot (\nabla, \partial_z\sigma\partial_\sigma)\phi = 0, \quad (\mathbf{x}, \sigma) \equiv \partial\Omega. \tag{13a}$$

Having obtained a solution for the function Φ in the σ-domain, the physical internal flow characteristics are obtained via the chain rule

$$\mathbf{u}(\mathbf{x}, z) = \nabla\phi(\mathbf{x}, z) = \nabla\Phi(\mathbf{x}, \sigma) + +\nabla\sigma\partial_\sigma\Phi(\mathbf{x}, \sigma), \tag{14a}$$

$$w(\mathbf{x}, z) = \partial_z\phi(\mathbf{x}, z) = \partial_\sigma\Phi(\mathbf{x}, \sigma)\partial_z\sigma. \tag{14b}$$

The sigma domain is now discretized using a structured grid with a possibly non-uniform spacing in each direction. Arbitrary order finite difference schemes are applied to approximate all partial derivatives and the resulting linear system of equations is solved iteratively using the Generalized Minimum Residual (GMRES) method preconditioned from the left by one multigrid V-cycle based on the linearized, second-order version of the system matrix. The classical explicit fourth-order, four-step Runge-Kutta method is used to integrate the free surface boundary conditions in time. Further details can be found in [25].

3. Numerical results and discussion

The test case applies a JONSWAP wave spectrum with significant wave height $H_{m0} = 4.5\,\mathrm{m}$ and $T_p = 15.15\,\mathrm{s}$ at the deep-water boundary. To ensure grid-independent results, we perform a convergence study of the MIKE 21 SW model. The spatial and temporal resolution of the OceanWave3D is $\Delta x = 1.5\,\mathrm{m}$ and $\Delta t = 0.0316\,\mathrm{s}$, and sixth-order finite difference schemes to approximate the spatial derivatives. Based on the analyses from [24, 25], this will ensure an accurate representation of the nonlinear wave dynamics down to a

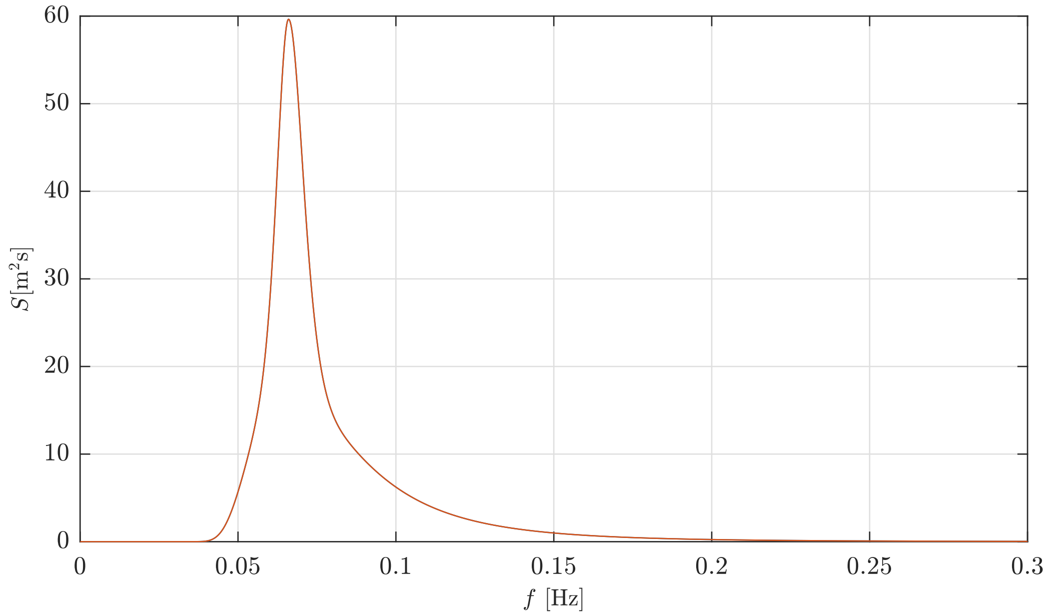

Figure 2: The JONSWAP wave spectrum with $H_s = 4.5$m and $T_p = 15.15$s applied at the deep-water boundary.

wavelength of approximately 15m which corresponds to a linear wave frequency of $f = 0.32$Hz at the shallow end of the domain. Thus we are sure to capture all significant wave energy during the simulation, as can be seen from Fig. 2. As the waves shoal, some mild breaking will occur, and based on previous studies using this model [34, 35, 36], the simple breaking model discussed in those references is able to accurately capture this effect on the spectral evolution. The breaking model monitors the downward Lagrangian particle acceleration of the free surface and when this exceeds $0.5g$, filtering is applied to extract energy until the acceleration falls below the threshold.

3.1. Convergence of MIKE 21 SW model

In order to do a reasonable comparison between the two wave models, it is essential that we ensure that the spectral wave model has converged. This means that by refining the spatial- and temporal domain further, we do not experience any improvement in the accuracy of the model. Table 1 shows a number of different runs of the MIKE 21 SW model, where the refinement of the model in both temporal and spatial regards have been increased in order to achieve convergence. Fig. 3 shows the significant wave height (H_{m0}) on the left y-axis, the water depth on the right y-axis and the position on the x-axis.

Fig. 3 shows that after the fourth refinement, the solution has converged, and it is therefore not necessary to refine the resolution of the model domain any further. However, further refinements are shown in order to visualize that the solution does not change any further by further refinement.

The MIKE 21 SW is run with the fully spectral formulation and the instationary temporal formulation. The spectral discretization of the model is with four directions (since we look at waves travelling in only one direction, four is the minimum), and 45 frequencies with the minimum frequency at 0.01 Hz and a logarithmic frequency distribution and a maximum frequency at 0.66 Hz.

3.2. Model comparison results

In order to test the accuracy of the nonlinear and white capping terms in the MIKE 21 SW model, we extract the wave spectrum at different points along the model domain (Fig. 1) moving from deep to shallow

Table 1: Convergence runs - spatial and temporal parameters.

# Run	Δx	Δt
[-]	[m]	[s]
1st	983	5
2nd	491.5	2.5
3rd	245.75	1.25
4th	122.875	0.625
5th	61.44	0.3125
6th	30.72	0.15625
7th	15.36	0.078125
8th	7.68	0.0390625

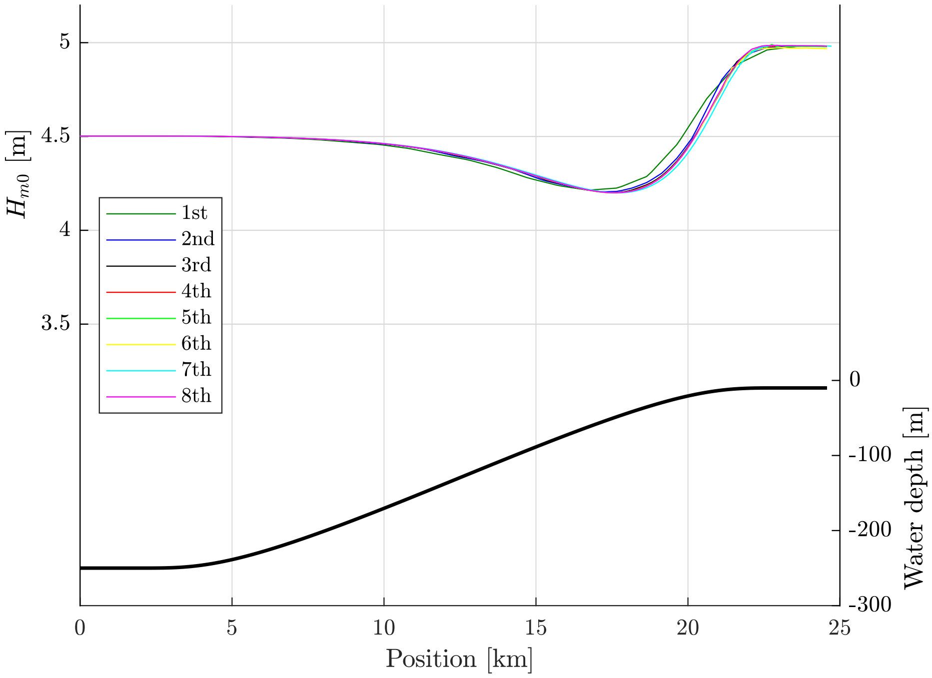

Figure 3: Convergence test of the MIKE 21 SW model.

water. Table 2 shows the water depth and distance from zero for each extraction point.

3.2.1. Spectral analysis

A Fast-Fourier Transform is used to compute the energy spectrum. Specifically, we use the built-in function in MATLAB [37] "`fft`" to find the Fourier coefficients of the wave signal. Due to the high frequency resolution of the results from the OW3D model, there are large fluctuations in the results - we therefore apply a smoothing filter (windowing) to ease the comparison with the spectral results from the MIKE 21 SW model. An example of the smoothing is seen in Fig. 4

We here use a Savitsky-Golay filter [38] of first order and a framelength of 101. This is done in order to "smooth out" the fluctuations in the spectral function derived from the OceanWave3D time-series. However, to ensure that the filtering of the raw signal does not have an affect on the energy spectrum, we integrate

Table 2: Extraction points.

Point	d	h	$k_p h$
[-]	[m]	[m]	[-]
1	1080	250	4.38
2	2900	249	4.36
3	8084	200	3.51
4	11260	150	2.65
5	14290	100	1.84
6	15540	80	1.53
7	16850	60	1.24
8	17550	50	1.09
9	18290	40	0.94
10	19100	30	0.80
11	20080	20	0.63
12	21910	10.5	0.44

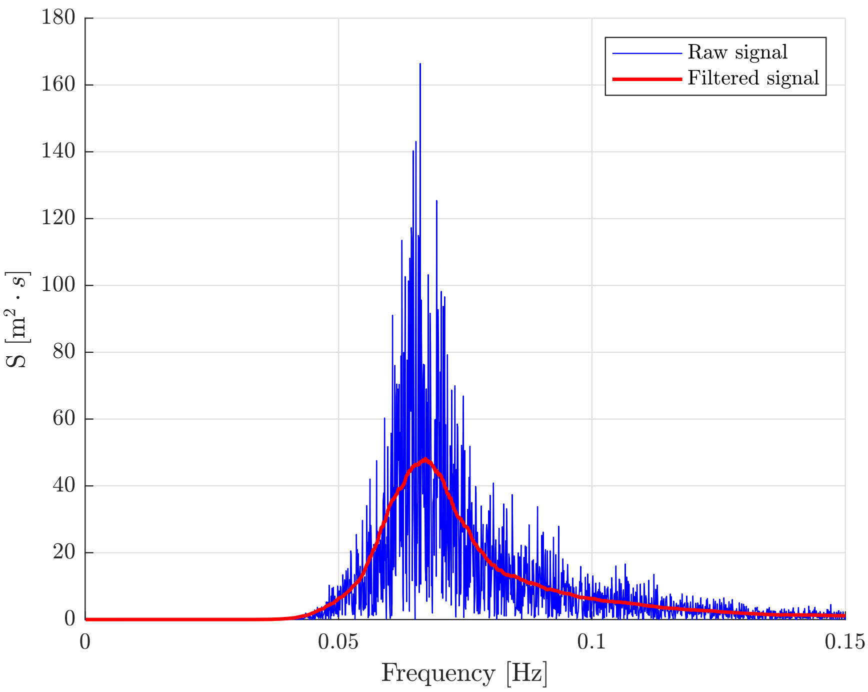

Figure 4: Raw spectral signal versus filtered spectral signal.

the energy spectrum before filtering for all represented frequencies and compare to the integrated energy spectrum after the filter has been applied. These are accurate to the fourth decimal, which we therefore can conclude that the filter does not affect the actual results, but merely improves to visual representation of the energy spectrum.

Regarding the comparison between the two models, we will use the filtered signal from the OW3D spectral analysis results to compare with results from the MIKE 21 SW model. The results from both models are compared at each of the points listed in Table 2. The last column of this table shows the relative water depth of the peak wave, $k_p h$, according to linear theory. Fig. 5, Fig. 6 and Fig. 7 show the spectral density as a function of the wave frequency.

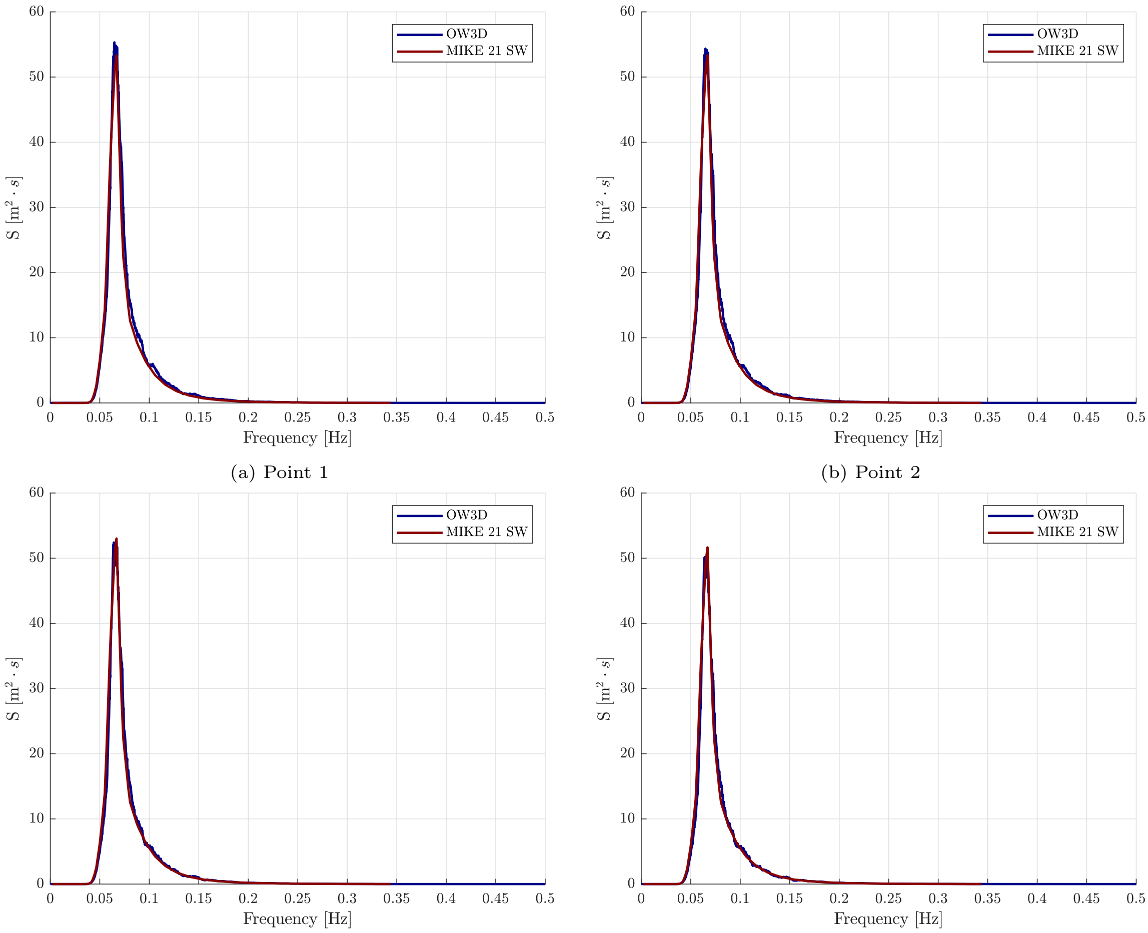

(a) Point 1 (b) Point 2 (c) Point 3 (d) Point 4

Figure 5: Comparison of the two models in points 1 to 4.

The comparison points show that there is good agreement between the models at points 1-10, corresponding to values of $k_p h >\approx 0.8$. For points 11 and 12, with $k_p h < 0.8$, there are deviations between the two models which are most evident at point 12. As the waves travel from deep water to shallow water, the waves become increasingly nonlinear and wave-wave interaction effects slowly change from being dominated by quartet interactions to triad interactions.

It is noticeable that the MIKE 21 SW model is able to capture some of the nonlinear physical effects, even though it can't capture them all. In Fig. 7 (c) we can see that there is a second, higher frequency peak in the spectrum slowly evolving, indicating that there are super-harmonics present in the wave signal. In Fig. 7 (d) it is even more evolved and for the OceanWave3d model spectrum, the peak occurs at a lower frequency both compared to the MIKE model and the previous point.

It is interesting to notice, that the OW3D model is able to capture low-frequency sub-harmonic contribu-

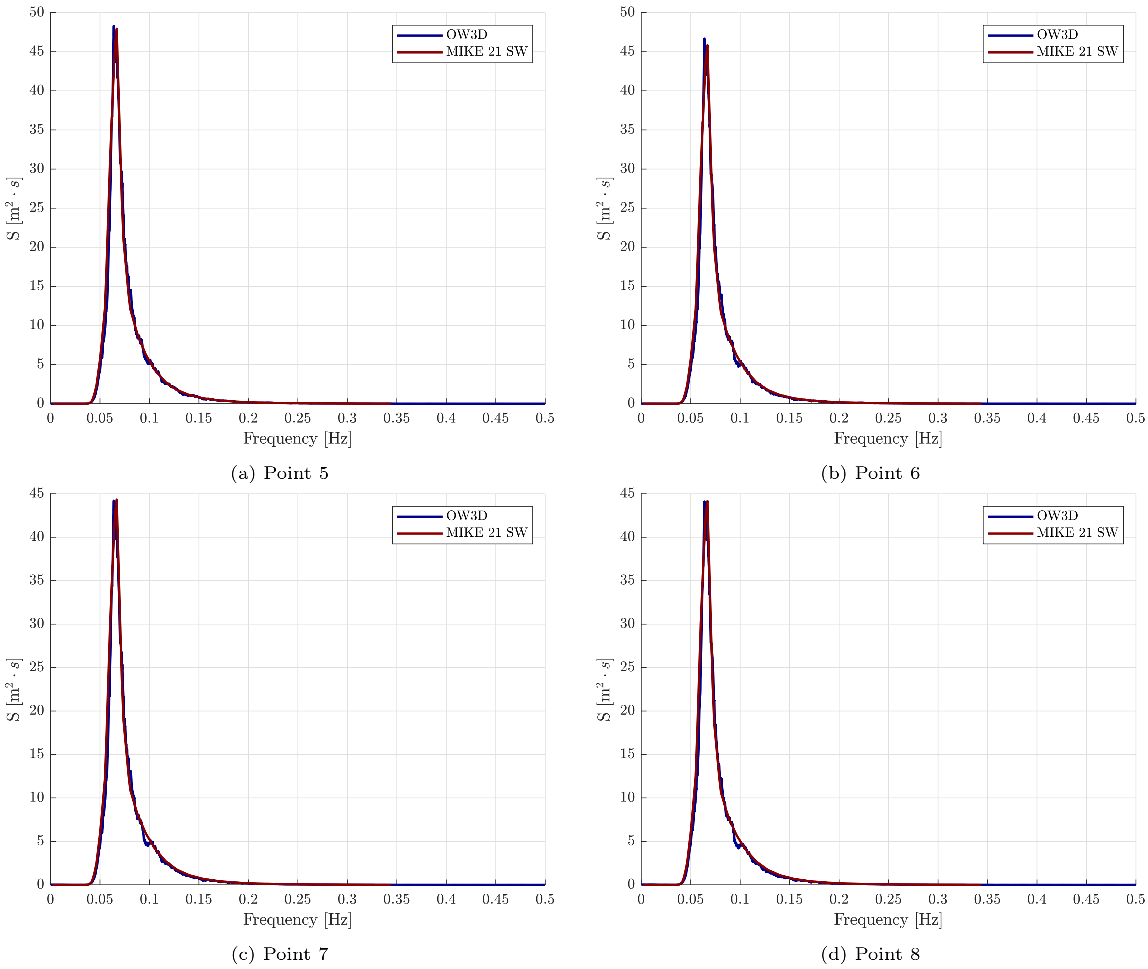

(a) Point 5 (b) Point 6

(c) Point 7 (d) Point 8

Figure 6: Comparison of the two models in points 5 to 8.

tion from the nonlinear energy transfer, while the MIKE model doesn't capture this at all. This is presumably because spectral wave models have only recently begun to model low-frequency infra-gravity waves [39, 40]. As pointed out by [41] the impacts from infra-gravity can be quite significant, emphasizing the importance of improving this aspect of spectral wave modelling.

Even though there are shortcomings in the MIKE 21 SW compared to the OceanWave3D model, the MIKE 21 SW model is able to capture the majority of the physical processes in deep and intermediate water. Furthermore, the MIKE 21 SW model took approximately 20 minutes to run, while the OceanWave3D model took approximately 6 days to run. So the computational efficiency of the spectral model is quite attractive.

4. Conclusions

A simple 2D, shoaling problem has been used to investigate the performance of the Mike 21 SW spectral wave model by comparison with the fully nonlinear potential flow solver OceanWave3D. Based on previous studies comparing calculations with experimental measurements, the OceanWave3D model is considered to

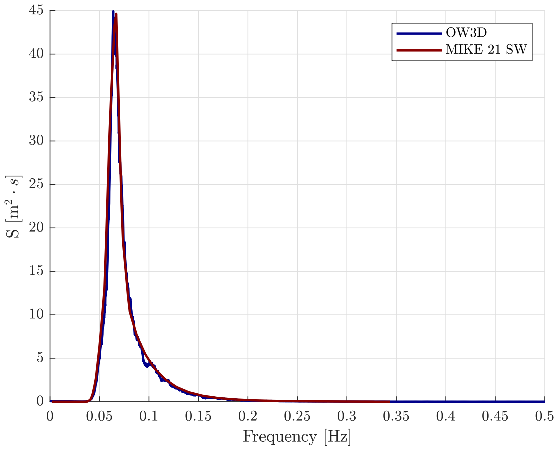

(a) Point 9

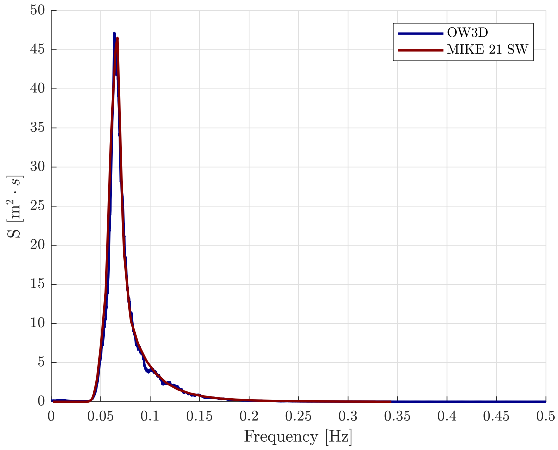

(b) Point 10

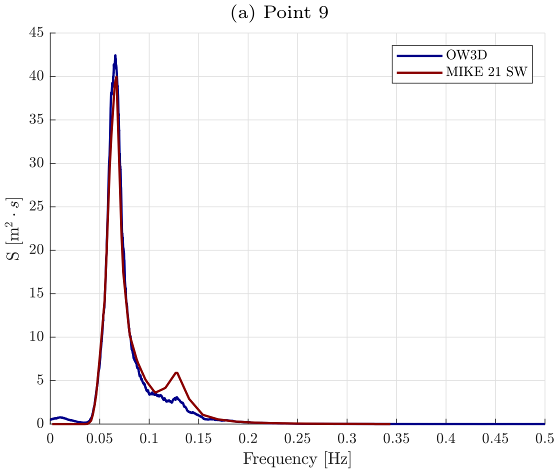

(c) Point 11

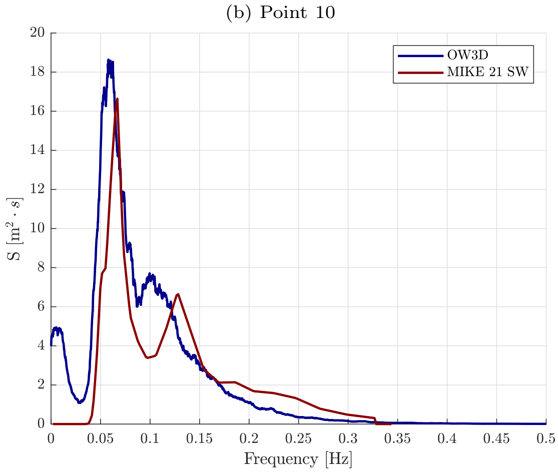

(d) Point 12

Figure 7: Comparison of the two models in points 9 to 12.

be an accurate benchmark with the adopted resolution. A convergence study of the MIKE 21 SW model was run to ensure grid-independent results.

As the waves propagate from deep to shallow water, the two models agree well until $k_p h \approx 0.8$. However, for $k_p h < 0.8$ increasingly large deviations can be seen in the super-harmonics and the position of the spectral peak, while sub-harmonic effects are entirely absent from the MIKE 21 SW results. This indicates a need to improve this aspect of the nonlinear wave-wave interaction modelling in this spectral wave model.

CRediT author contribution statement

Bárður Joensen: Methodology, Validation, Formal analysis, Investigation, Data curation, Numerical model setup, Writing – original draft, Writing – review & editing, Funding acquisition. **Harry B. Bingham:** Numerical model setup, Writing - original draft, Writing - review & editing, Supervision, Project administration.

Declaration of competing interests

The authors declare that they have no known competing financial interests or personal relationships that could have appeared to influence the work reported in this paper.

Acknowledgements

This study is based on project supported by the Research Council of the Faroe Islands, grant number 02010. The same project is also financially supported by Betri Research Foundation, SEV, Bakkafrost Farming, MOWI Faroes and Hiddenfjord.

References

[1] A. Ilia, J. O'Donnell, An assessment of two models of wave propagation in an estuary protected by breakwaters, Journal of Marine Science and Engineering 6 (4) (2018) 145. doi:10.3390/jmse6040145.

[2] DHI, MIKE 21 Spectral waves FM, user guide., DHI, Agern Allé 5, 2970 Hørsholm, Denmark (2022).

[3] R. C. Ris, L. H. Holthuijsen, N. Booji, A third-generation wave model for coastal regions: 2. verification, Journal of Geophysical Research: Oceans 104 (C4) (1999) 7667–7681. doi:10.1029/1998jc900123.

[4] Z. Yang, V. S. Neary, T. Wang, B. Gunawan, A. R. Dallman, W.-C. Wu, A wave model test bed study for wave energy resource characterization, Renewable Energy 114 (2017) 132–144. doi:10.1016/j.renene.2016.12.057.

[5] The WAVEWATCH III ® Development Group, User manual and system documentation of WAVEWATCH III ® version 5.16, Tech. Note 329, NOAA/NWS/NCEP/MMAB, 326 pp. + Appendices (2016).

[6] J. C. McNatt, A. Porter, K. Ruehl, Comparison of numerical methods for modeling the wave field effects generated by individual wave energy converters and multiple converter wave farms, Journal of Marine Science and Engineering 8 (3) (2020) 168. doi:10.3390/jmse8030168.

[7] K. Ruehl, A. Porter, C. Chartrand, H. Smith, G. Chang, J. Roberts, Development, verification and application of the snl-swan open source wave farm code, in: Proceedings of the 11th European Wave and Tidal Energy Conference, Nantes.

[8] J. N. Newman, C.-H. Lee, Wamit; a radiation-diffraction panel program for wave-structure interactions.

[9] M. A. Hoque, W. Perrie, S. M. Solomon, Evaluation of two spectral wave models for wave hindcasting in the mackenzie delta, Applied Ocean Research 62 (2017) 169–180. doi:10.1016/j.apor.2016.11.009.

[10] R. B. Fonseca, M. Gonçalves, C. G. Soares, Comparing the performance of spectral wave models for coastal areas, Journal of Coastal Research 332 (2017) 331–346. doi:10.2112/jcoastres-d-15-00200.1.

[11] T. C. Massey, M. E. Anderson, J. M. Smith, J. Gomez, R. Jones, Stwave: Steady-state spectral wave modeluser's manual for stwave, version 6.0, Tech. rep., US Army Corps of Engineers, Engineer Research and development Center.

[12] S.-H. Oh, K.-D. Suh, S. Y. Son, D. Y. Lee, Performance comparison of spectral wave models based on different governing equations including wave breaking, KSCE Journal of Civil Engineering 13 (2) (2009) 75–84. doi:10.1007/s12205-009-0075-y.

[13] J. Kirby, H. Özkan, Documentation and user's manual,combined refraction/diffraction model for spectral wave conditions,ref/dif s, version 1.1.

[14] V. Venugopal, R. Nemalidinne, Wave resource assessment for Scottish waters using a large scale North Atlantic spectral wave model, Renewable Energy 76 (2015) 503–525. doi:10.1016/j.renene.2014.11.056.

[15] P. Pilar, C. G. Soares, J. Carretero, 44-year wave hindcast for the north east atlantic european coast, Coastal Engineering 55 (11) (2008) 861–871. doi:10.1016/j.coastaleng.2008.02.027.

[16] E. Rusu, C. G. Soares, Wave energy pattern around the madeira islands, Energy 45 (1) (2012) 771–785. doi:10.1016/j.energy.2012.07.013.

[17] R. C. Lisboa, P. R. Teixeira, C. J. Fortes, Numerical evaluation of wave energy potential in the south of Brazil, Energy 121 (2017) 176–184. doi:10.1016/j.energy.2017.01.001.

[18] B. Joensen, B. A. Niclasen, H. B. Bingham, Wave power assessment in faroese waters using an oceanic to nearshore scale spectral wave model, Energy 235 (2021) 121404. doi:10.1016/j.energy.2021.121404.

[19] E. Rusu, C. G. Soares, Modeling waves in open coastal areas and harbors with phase-resolving and phase-averaged models 29 (6) 1309. doi:10.2112/jcoastres-d-11-00209.1.

[20] P. Smit, M. Zijlema, G. Stelling, Depth-induced wave breaking in a non-hydrostatic, near-shore wave model 76 1–16. doi:10.1016/j.coastaleng.2013.01.008.

[21] W. Wang, C. Pákozdi, A. Kamath, S. Fouques, H. Bihs, A flexible fully nonlinear potential flow model for wave propagation over the complex topography of the norwegian coast, Applied Ocean Research 122 103103. doi:10.1016/j.apor.2022.103103.

[22] H. Bihs, W. Wang, C. Pakozdi, A. Kamath, REEF3d::FNPF—a flexible fully nonlinear potential flow solver, Journal of Offshore Mechanics and Arctic Engineering 142 (4). doi:10.1115/1.4045915.

[23] DHI, MIKE 21 Wave modelling, spectral waves FM, short description, DHI, Agern Allé 5, 2970 Hørsholm, Denmark (2022).

[24] H. B. Bingham, H. Zhang, On the accuracy of finite-difference solutions for nonlinear water waves, Journal of Engineering Mathematics 58 (1-4) (2006) 211–228. doi:10.1007/s10665-006-9108-4.

[25] A. Engsig-Karup, H. Bingham, O. Lindberg, An efficient flexible-order model for 3d nonlinear water waves, Journal of Computational Physics 228 (6) (2009) 2100–2118. doi:10.1016/j.jcp.2008.11.028.

[26] G. J. Komen, L. Cavaleri, M. Donelan, K. Hasselmann, S. Hasselmann, P. A. E. M. Janssen, Dynamics and Modelling of Ocean Waves, Cambridge University Press, 1994. doi:10.1017/cbo9780511628955.

[27] P. Janssen, Wave induced stress and the drag of airflow over sea waves., Journal of Physical Oceanography 19 (1989) 745–754.

[28] P. Janssen., Quasi-linear theory of wind wave generation applied to wave forecasting., Journal of Physical Oceanography. 19 (1991) 1631–1642.

[29] S. Hasselmann, K. Hasselmann, J. Allender, T. Barnett, Computations and parameterizations of the nonlinear energy transfer in a gravity wave spectrum. Part ii: Parameterizations of the nonlinear transfer for application in wave models, Journal of Physical Oceanography 15 (11) (1985) 1378–1391.

[30] Y. Eldeberky, J. Battjes, Parameterisation of triad interactions in wave energy models, in: Coastal Dynamics' 95, ASCE, pp. 140–148.

[31] Y. Eldeberky, J. A. Battjes, Spectral modeling of wave breaking: Application to boussinesq equations, Journal of Geophysical Research: Oceans 101 (C1) (1996) 1253–1264.

[32] DHI, MIKE 21 Spectral Wave Module, Scientific documentation (2022).

[33] A. P. Engsig-Karup, H. B. Bingham, O. Lindberg, B. T. Paulsen, OceanWave3D; an efficient coastal engineering tool for nonlinear waves., https://github.com/apengsigkarup/OceanWave3D-Fortran90 (2023).

[34] F. Pierella, O. Lindberg, H. Bredmose, H. B. Bingham, R. W. Read, A. P. Engsig-Karup, The derisk database: Extreme design waves for offshore wind turbines 80 (2021) 103046. doi:https://doi.org/10.1016/j.marstruc.2021.103046.

[35] A. Ghadirian, H. Bredmose, Investigation of the effect of bed slope on extreme waves using First Order Reliability Method, Marine Structures 67 (102627) (2019).

[36] S. Schløer, H. Bredmose, A. Ghadirian, Experimental and numerical statistics of storm wave forces on a monopile in uni- and multidirectional seas, Ocean Renewable Energy 10 (2017) V010T09A073.

[37] MathWorks, Matlab (Accessed 2023-02-27).
URL https://se.mathworks.com/

[38] R. Schafer, What is a savitzky-golay filter? [lecture notes] 28 (4) 111–117. doi:10.1109/msp.2011.941097.

[39] F. Ardhuin, A. Rawat, J. Aucan, A numerical model for free infragravity waves: Definition and validation at regional and global scales, Ocean Modelling 77 20–32. doi:10.1016/j.ocemod.2014.02.006.

[40] A. Reniers, M. Zijlema, SWAN SurfBeat-1d, Coastal Engineering 172 104068. doi:10.1016/j.coastaleng.2021.104068.

[41] X. Bertin, A. de Bakker, A. van Dongeren, G. Coco, G. André, F. Ardhuin, P. Bonneton, F. Bouchette, B. Castelle, W. C. Crawford, M. Davidson, M. Deen, G. Dodet, T. Guérin, K. Inch, F. Leckler, R. McCall, H. Muller, M. Olabarrieta, D. Roelvink, G. Ruessink, D. Sous, É. Stutzmann, M. Tissier, Infragravity waves: From driving mechanisms to impacts, Earth-Science Reviews 177 774–799. doi:10.1016/j.earscirev.2018.01.002.

Chapter 3

Wave power assessment in Faroese waters using an oceanic to nearshore scale spectral wave model

The paper entitled ”Wave power assessment in Faroese waters using an oceanic to nearshore scale spectral wave model” has been published in the Journal of Energy as:

Bárður Joensen, Bárður A. Niclasen, and Harry B. Bingham. “Wave power assessment in Faroese waters using an oceanic to nearshore scale spectral wave model”. In: *Energy* 235 (Nov. 2021), p. 121404. DOI: 10.1016/j.energy.2021.121404

Energy 235 (2021) 121404

Contents lists available at ScienceDirect

Energy

journal homepage: www.elsevier.com/locate/energy

Wave power assessment in Faroese waters using an oceanic to nearshore scale spectral wave model

Bárður Joensen [a, b, *], Bárður A. Niclasen [c], Harry B. Bingham [b]

[a] LBF Consulting Engineers, Niels Finsensgøta 10, FO-110 Tórshavn, Faroe Islands
[b] Technical University of Denmark, Department of Mechanical Engineering, Section for Fluid Mechanics, Coastal and Maritime Engineering, Nils Koppels Allé building 404, 2800, Kgs. Lyngby, Denmark
[c] University of Faroe Islands, Department of Science & Technology, Vestara Bryggja 15, FO-100 Tórshavn, Faroe Islands

ARTICLE INFO

Article history:
Received 2 January 2021
Received in revised form
8 May 2021
Accepted 1 July 2021
Available online 8 July 2021

Keywords:
Wave power
Spectral wave model
MIKE 21 SW
Wave hindcasting
Faroe Islands

ABSTRACT

It is expected that wave power will first become an economically competitive energy source in isolated electrical grids located in exposed regions. One such candidate is the Faroe Islands. The goal of this paper is to map the local wave power potential around the Faroe Islands using the spectral wave model MIKE 21 SW. A model is set up for the entire North Atlantic Ocean. The model is forced by 10 years of ERA5 reanalysis wind data and is validated against several directional offshore wave buoys along with nearshore acoustic Doppler current profile measurements. The results show that the wave climate is dominated by waves from south-to-west and to a lesser extent from northerly directions, while waves from other directions are more moderate and infrequent. The average wave energy flux at nearshore locations to the west and north is 45–55 kW/m, while significantly lower flux of 10–25 kW/m is found at eastern locations. The results show that the maximum significant wave heights are 12–14 m to the west, 9–13 m to the north and 8–9 m to the east. This energy assessment will provide the basis for an evaluation of wave energy absorption concepts suitable for deployment in the Faroese waters.

1. Introduction

Due to a heavy dependence on fossil fuels and the threatening side effects of greenhouse gasses, governments are called upon to take action, and significantly increase energy production from renewable energy sources. The Faroese government, together with the local electricity company (SEV), have announced that they aim to achieve 100% carbon emissions-free land-based energy production by 2030. In recent years the local share of renewable production has been 40% from hydro- and wind-power, with 60% coming from oil. The relatively high dependence on imported oil makes the electricity price, among the highest in the world [1]. The high cost of production is a hidden asset in the transformation towards a 100% renewable energy system, as projects based on renewable sources can have a lower price of energy relative to existing oil based production. Recent developments and plans for variable renewable production, aided by pumped storage systems support the realization of renewable land-based energy production [2,3], but with restrictions for further development of hydro-power,

* Corresponding author. Technical University of Denmark, Department of Mechanical Engineering, Section for Fluid Mechanics, Coastal and Maritime Engineering, Nils Koppels Allé building 404, 2800, Kgs. Lyngby, Denmark.
E-mail address: bajoe@mek.dtu.dk (B. Joensen).

https://doi.org/10.1016/j.energy.2021.121404

there could be a need for additional alternatives to wind and solar power to achieve 100% production from renewable sources [4].

ρ	Density of water [kg/m^3]
σ	Intrinsic angular frequency [rad/s]
$c(\sigma, \theta)$	Propagation velocity in spectral space
c_x	Propagation velocity in x-direction [m/s]
c_y	Propagation velocity in y-direction [m/s]
Dir_p	Peak wave direction [deg]
$E(\sigma, \theta)$	Wave energy spectrum [m^2 s/rad]
g	Gravitational acceleration $[\mathrm{m/s^2}$
h	Water depth [m]
H_{m0}	Significant wave height [m]
k_e	Wave number based on energy period [m^{-1}]
N	Wave action density
P	Wave energy flux [kW/m]
P_{annual}	Annual mean wave energy [MWh/m]
p_{hourly}	Hourly occurrence of sea state [−]
S_{bot}	Bottom friction dissipation
S_{ds}	White-capping dissipation
S_{in}	Momentum transfer of wind to wave generation
S_{nl}	Nonlinear wave-wave interaction
S_{surf}	Depth-induced wave breaking
S_{tot}	Total source term
t	Time variable [s]
T_e	Energy period [s]
T_p	Peak wave period [s]
θ	Wave direction [rad]
ADCP	Acoustic Doppler Current Profiler
CDS	Climate Data Store
DIA	Discrete Interaction Approximation
ECMWF	European Center for Medium Range Weather Forecast
ERA5	5th generation ECMWF reanalysis dataset for global climate and weather
GEBCO	General Bathymetric Chart of the Oceans
HIRLAM	High Resolution Limited Area Modeling
MIKE 21 NSW	DHI's Near-shore spectral wind-wave model (no longer available)
MIKE 21 SW	DHI's 3rd generation spectral wave model
NCAR	National Center for Atmospheric Research
NCEP	National Centers for Environmental Prediction
PNJ	Pierson-Neumann-James wave prediction method
R	Correlation coefficient
RMSE	Root-mean-square error
SI	Scatter index
SMB	Sverdrup-Munk-Bretschneider wave prediction method
SWAN	3rd generation spectral wave model developed by Delft University
WAM	3rd generation ocean wave prediction model
WaveWatch III	3rd generation ocean wave model

Recent developments in wave power production look both interesting and promising. Furthermore, there is a lot of investment in research and development of wave energy conversion concepts/techniques [5]. A lot of work has been performed to assess the potential for wave power production worldwide. This generally involves running numerical spectral wave model hindcasts, which are validated against measured data. Locations such as Northeast Asia [6], Sri Lanka [7] and the South China Sea [8] have been studied. For the aforementioned studies, SWAN [9] was used to develop the wave model, and was forced using wind data from the Japan Meteorological Agency [10]. Furthermore, many studies have been performed that analyze the coasts of North America in terms of wave energy assessment [11–14]. Refs. [12–14] used WaveWatch III [15], while [11] ran nested simulations in WaveWatch III and used SWAN to run high resolution simulations for the nearshore climate. With a more global perspective [16], compiled an atlas of the global wave energy resource, using WaveWatch III. This showed that the North Atlantic Ocean, specifically the Northeast Atlantic Ocean, holds high amounts of wave energy. The Bay of Biscay and the Iberian Peninsula are locations which have been studied extensively for wave energy potential assessment. Ref. [17] developed a wave model using SWAN and forced at the offshore boundary using wave measurement buoys. Refs. [18] and [19] both used WAM [20], while [18] used global atmospheric data from (NCEP) and (NCAR) [19,21] used the HIRLAM [22] numerical model for atmospheric data. Refs. [23,24], and [25] developed an offshore model using WAM, and ran nested simulations to feed in to a coastal SWAN model, while [26] only used SWAN to develop their model. Furthermore, Scottish waters have also been an area under consideration [27]. This study used MIKE 21 SW [28], a sub model in DHI's MIKE 21 model suite, and forced the model using wind data from ECMWF [29].

There exist several studies on the wave power potential in island communities in the North Atlantic Ocean e.g. Refs. [30–34], but none on the high resolution mapping of the wave energy potential on the Faroe Shelf. A few local studies have been conducted to analyze wave conditions around the islands. Ref. [35] used analytical methods, such as the SMB method (Sverdrup-Munk-Bretschneider) [36], Wilson's method [36] and the PNJ method (Pierson-Neumann-James) [37]. Ref. [38] used MIKE 21 NSW (Near-shore spectral wind-wave model) forced by local wave buoy measurements to analyze the wave climate around the islands. Also short time hindcasts from an operational wave model [39] using SWAN, forced by wind have been used to estimate the wave climate. However, none of these have focused on mapping the wave energy potential, although some introductory estimates have been derived based on local measurements [40]. The previous local studies on the wave climate around the Faroe Islands, have shown that there are large wave heights present. The western and northern coasts are dominated by larger wave heights, compared to the eastern coasts. Ref. [41] showed values of an estimated 10-year maximum significant wave height of 16 m at the western and northern coasts. However, none of the previous studies show any details on the wave periods, and the information on the wave energy is very limited.

By taking advantage of faster computers and the ability to run a wave model with an unstructured mesh, which is coarse offshore but with high resolution nearshore, it is now for the first time feasible to map the local wave power potential with high resolution for the waters surrounding the Faroe Islands, without any simplifying assumptions on the forcing, wave field or wave model physics. Compared to other local studies, this investigation is also validated against more data and over a longer time-span.

The objective of the present work is to evaluate and assess the wave climate around the Faroe Islands. This is done by using wave buoy measurements and numerical wave modelling. The numerical wave model used in this study is MIKE 21 SW. The area around the Faroe Islands holds a vast amount of wave energy, making it a viable candidate for wave energy conversion. Wave energy content is high but this is also a challenge, as the Faroe Islands are located close to one of the harshest recorded wave climates in the world [42]. This is challenging, due to the potentially large forces associated with large and steep waves making the design of the proposed wave energy devices more expensive.

2. Model overview

When modeling waves at scales where instationary wave growth is important, the standard approach is to use spectrally averaged wave models. These models predict the growth, transformation and decay of ocean waves, due to their interaction with ocean surface winds and bathymetry. In the present study, such a spectral wave model is used. The underlying concept of spectral wave models is the energy balance equation, where the evolution of the wave spectrum is given by:

$$\frac{\partial E}{\partial t}+\frac{\partial}{\partial x}(c_x E)+\frac{\partial}{\partial y}(c_y E)+\frac{\partial}{\partial \sigma}(c_\sigma E)+\frac{\partial}{\partial \theta}(c_\theta E)=S_{tot} \tag{1}$$

where $E(\sigma,\ \theta)$ is the wave energy spectrum, t is time, σ is the intrinsic angular frequency, θ is the wave direction, c_x and c_y are the propagation velocities in the geographical space, while c_σ and c_θ are the propagation velocities in the spectral space. The first term represents the local rate of change of energy density in time. The second and third terms represent the geographic propagation of energy density in the (x,y)-space. The fourth term represents the shifting of the frequency due to depth variations, and the fifth and last term is related to depth-induced refraction with propagation velocity c_θ in the θ-space. In short, the left hand side of Equation (1) constitutes the propagation of a large sum of independent linear waves.

The right hand side of Equation (1) represents the effects of generation, dissipation and nonlinear wave-wave interaction. The total source term is expressed as

$$S_{tot}=S_{in}+S_{nl}+S_{ds}+S_{bot}+S_{surf} \tag{2}$$

where S_{in} is the momentum transfer of wind energy to wave generation, S_{nl} is the nonlinear wave-wave interaction (triad and quadruplet), S_{ds} is the dissipation of energy due to white-capping, S_{bot} is the dissipation of energy due to bottom friction and S_{surf} is the dissipation of energy due to depth-induced wave breaking. In deep water the evolution of the spectrum is dominated by the balance between S_{in}, S_{ds} and the quadruplet part of S_{nl}. In shallower water the triad part of S_{nl}, S_{bot} as well as S_{surf} become increasingly important parts of the evolution. The input term S_{in} works at all depth ranges, increasing the amplitudes of wave components traveling in a similar direction to the wind, but with lower phase speeds.

For this particular study the third-generation spectral wave model MIKE 21 SW has been used for modeling the waves [43]. This model discretizes the governing equations in geographical and spectral space using a cell-centered finite volume method. In the geographical domain an unstructured mesh technique is used. The time integration is performed using a fractional step approach where a multi-sequence explicit method is applied for the propagation of wave action [28].

The source functions S_{in}, S_{nl}, and S_{ds} are similar to those in the WAM Cycle 4 model [44]. The wind input is based on Janssen's ([45,46]) quasi-linear theory of wind-wave generation, where the momentum transfer from the wind to the sea not only depends on the wind stress, but also on the sea-state. The quadruplet wave-wave interaction is based on the computationally efficient Discrete Interaction Approximation (DIA) proposed in Ref. [47] and the S_{ds} term is based on the formulation of white-capping in Ref. [44].

There is also the possibility of including variations due to wave-current interactions and time-varying water depth, in which the wave action density N becomes the dependent parameter. Since no wave-current interactions and time-varying water depth are considered in this study, this will not be described here.

3. Model set-up

This section provides details on how the model has been set up. Bathymetry, mesh, model forcing and physical processes will be reviewed here.

3.1. Bathymetry and mesh

As mentioned previously, the study area is the waters around the Faroe Islands. Fig. 1 shows the oceanic scale computational domain (left), together with the refined grid around the Faroe Islands (right). An unstructured computational mesh has been used for the computational domain. This is constructed using the MIKE mesh-generator, and it covers the area 70°W to 10°E and 5°N to 80°N. Swells generated in the Atlantic Ocean travel long distances and reach the Faroe Islands with little loss of wave energy. This is a positive feature for the extraction of energy from waves. In order to catch all the swells traveling from the Atlantic, it was necessary to use a large computational model, even though, the area of interest is mainly around the Faroe Islands. Bathymetry data was acquired from the General Bathymetric Chart of the Oceans (GEBCO) [48], and these were used to generate the mesh for the model domain.

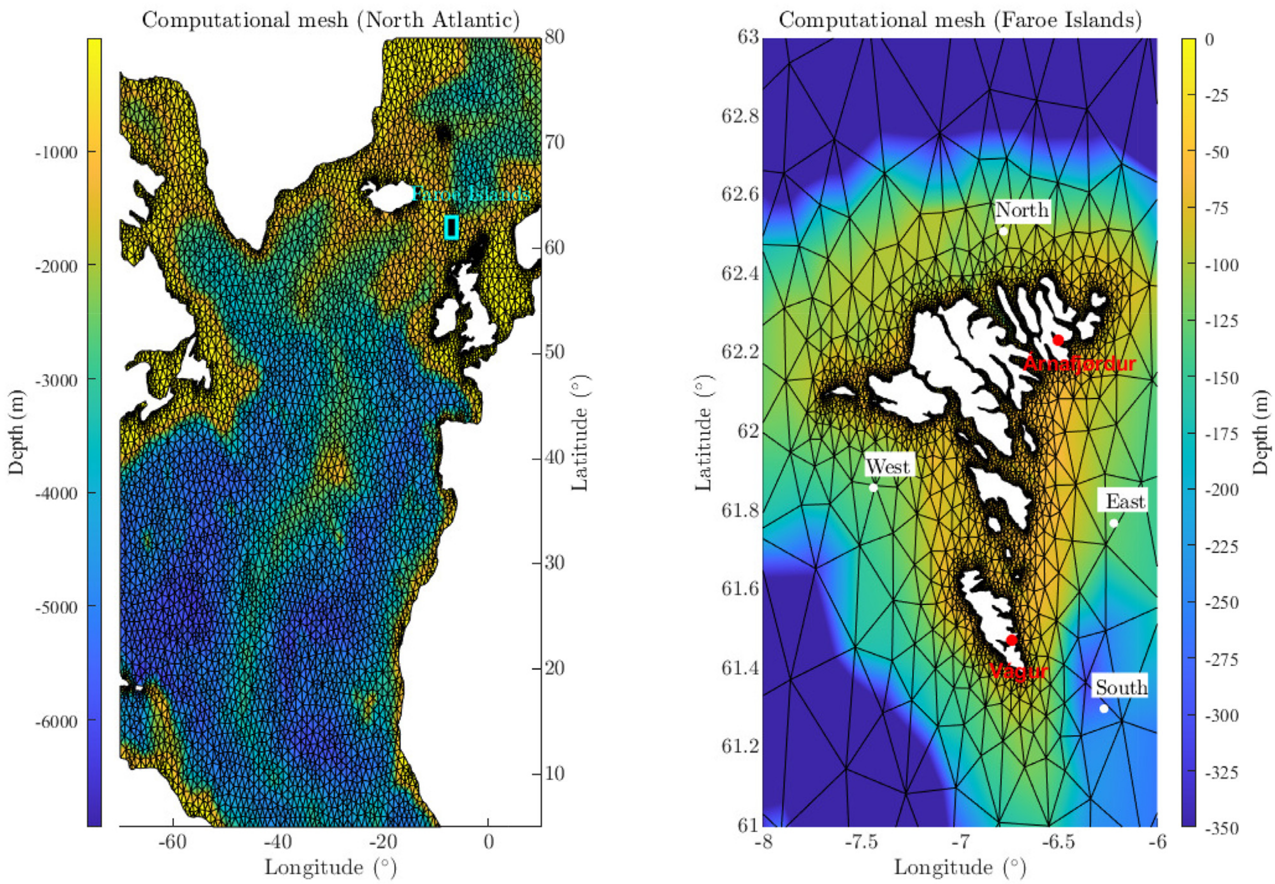

(a) North Atlantic computational mesh and bathymetry.

(b) Mesh and bathymetry around the Faroe Islands.

Fig. 1. The computational domain and mesh for the study area. (a) The North Atlantic, (b) the Faroe Islands together with wave measurement points.

Due to computational constraints, high resolution was only applied for the area around the Faroe Islands, where local bathymetry data was used [49], consisting of 100 m by 100 m data points. It was desirable to have a higher resolution of data, however this was not available. A filter was applied for the whole area (excluding 8°W to 6°W and 61°N to 63°N), such that the resolution of the bathymetric data for the rest of the North Atlantic was 1° latitude by 1° longitude.

The model domain consists of 19983 elements at various mesh resolutions, with the area around the Faroe Islands having the finest resolution and the North Atlantic ocean with the coarsest resolution. The mesh element area varies from $1.9 \cdot 10^4 \text{km}^2$ to $3.7 \cdot 10^{-3} \text{km}^2$ and the grid for the output results is the same resolution as the input mesh in Fig. 1 (b).

3.2. Model forcing and model settings

The model was forced with data for the wind speed at 10 m above sea level and its direction, acquired from the re-analysis dataset (ERA5) from the European Center for Medium range Weather Forecast (ECMWF) climate data store (CDS) [29]. This has a spatial resolution of 0.25°x0.25° and a temporal resolution of 1 hour. The ERA5 model reanalysis results will be used as an accepted state of the art reference for our region, since it is a model known to give acceptable local forecasts [50].

For the frequency discretization, a logarithmic discretization is used with a minimum frequency of 0.035 Hz, with 40 frequencies and a frequency factor of 1.1, see Ref. [28] for further details. For the directional discretization, 24 directions are used with each direction covering 15°.

As a default setting for the instationary formulation solution technique a 'lower order' geographical space discretization algorithm is used, with 'maximum number of levels in transport' of 32, where 'lower order' means a first order upwinding numerical

Table 1
Model forcing and physical processes activated in model.

Physical process/Set up	Value
Spectral formulation	Fully spectral
Time formulation	Instationary
Number of directions	24
Number of frequencies	40
Water level variation	No
Current conditions included	No
Ice coverage	No
Diffraction	No
Quadruplet wave interaction	Yes
Triad wave interaction	Yes
Wind forcing	ERA5 0.25x0.25° 10 m speed & direction
Depth-induced wave breaking	$H/h = 0.8$
Bottom friction	Nikuradse roughness, $k_N = 0.04$
White-capping	$C_{dis} = 1.9$ & $\delta_{dis} = 0.6$
Initial conditions	Zero spectra

scheme. No water level variation, current conditions, ice coverage or diffraction were included in the model. A point, located a few hundred meters south of the southernmost island was used for comparison for initial test runs to see the effect of including the diffraction. There was basically no difference in the significant wave height, peak wave period, wave direction or the wave power.

As a starting point, default settings were applied to the model. However, for the white-capping source term, the recommendation from Ref. [51] was applied, since we are dealing with a combination of wind-sea and swell. Initial model runs with the recommended value showed that the model underestimated the significant wave height, showing that the dissipation of energy due to white-capping was initially too high. Therefore, the dissipation coefficient C_{dis} was changed from the recommended value of 2.1 to 1.9. Table 1 shows the model forcing and physical processes activated in the model.

3.3. Wave data measurements used for validation of the model

All of the near-shore data used, has been provided by Fiskaaling (www.fiskaaling.fo). This data is collected with Acoustic Doppler Current Profilers (ADCP). These are mainly used for current measurements, but they can be used, for wave measurements as well. They are deployed in shallow water, since the measuring device has to be submerged at a limited depth in order to measure with sufficient accuracy [52].Four offshore 0.9 m diameter directional Datawell Waverider buoys are also used in the validation, see Fig. 1 (b). The first wave buoys were deployed in 1980 [53,54], and these have been a part of the local operational services for fishermen.

3.4. Validation of the MIKE 21 SW model

A comparison between the calculations from MIKE 21 SW and the measurements made at different locations around the islands is crucial in order to quantify the validity of the wave model. The Árnafjørdur and Vágur measurement locations are nearshore locations, while the east, north, west and south locations are offshore locations. The first two are associated with aquaculture in the Faroe Islands, and the others are owned and operated by Landsverk [55]. Fig. 1 (b) shows a map of the locations of the performed measurements. The model validations are performed over different time periods, because the nearshore location data only spans a few months recorded over a few different periods, while the measurements from Landsverk are large datasets which cover several decades. To quantify the validity of the wave model, statistical parameters such as bias, root-mean-square error (RMSE), scatter index (SI) and correlation coefficient (R) are calculated.

$$\text{Bias} = \frac{1}{N}\sum_{i=1}^{N}(x_{m_i} - x_{o_i}) \tag{3}$$

$$\text{RMSE} = \sqrt{\frac{1}{N}\sum_{i=1}^{N}(x_{m_i} - x_{o_i})^2} \tag{4}$$

$$\text{SI} = \frac{\text{RMSE}}{\bar{x}_o} \tag{5}$$

$$\text{R} = \frac{\sum_{i=1}^{N}(x_{m_i} - \bar{x}_m)(x_{o_i} - \bar{x}_o)}{\sqrt{\sum_{i=1}^{N}(x_{m_i} - \bar{x}_m)^2(x_{o_i} - \bar{x}_o)^2}} \tag{6}$$

where x_o is the observed (measured) data and x_m is the model data with mean values $\bar{x}_o$ and $\bar{x}_m$ respectively. Bias gives information on whether the model over- or underestimates the modeled parameter, RMSE gives information on the differences between the observed and modeled values (residuals). The scatter index SI puts the RMSE in a relative frame (non-dimensional), the correlation coefficient R measures the linear correlation between the modeled and measured values. The validation parameters for the wave direction are not calculated using a linear approach, which might yield misleading results, especially when considering waves traveling from a northern direction (0° and 360°). Instead, a vectorial approach is applied, taking the distance between each wave direction component (modeled and measured) to calculate the validation parameters.

Table 2
Validation parameters for measurements and MIKE model comparison.

Site	Parameters	Bias	RMSE	SI	R
East	H_{m0} [m]	−0.06	0.37	0.17	0.95
	T_p [s]	−0.56	1.78	0.20	0.75
	Dir_p [°]	24.71	32.29	0.26	0.68
West	H_{m0} [m]	−0.19	0.52	0.19	0.98
	T_p [s]	−0.23	2.05	0.20	0.70
	Dir_p [°]	22.17	30.33	0.12	0.64
North	H_{m0} [m]	−0.19	0.47	0.19	0.96
	T_p [s]	−0.22	1.48	0.15	0.82
	Dir_p [°]	21.05	28.63	0.14	0.62
South	H_{m0} [m]	−0.11	0.42	0.17	0.97
	T_p [s]	−0.26	1.37	0.14	0.85
	Dir_p [°]	20.30	28.23	0.15	0.60
Árnafj.	H_{m0} [m]	0.05	0.23	0.26	0.96
	T_p [s]	0.10	2.00	0.24	0.53
	Dir_p [°]	22.95	32.26	0.26	−0.18
Vágur	H_{m0} [m]	−0.03	0.15	0.24	0.96
	T_p [s]	0.61	2.49	0.32	0.47
	Dir_p [°]	23.78	30.01	0.32	0.35

Table 2 shows the validation parameters for the considered locations (see Fig. 1(b)). H_{m0} is the significant wave height, T_p is the peak wave period and Dir_p is the peak wave direction. For the east and south locations there is agreement between the modeled and measured significant wave height, however the model slightly under predicts the significant wave height. For the peak wave period, there is some discrepancy between the modeled and measured data. There is a reasonably low scatter value and a fairly high correlation. For the west and north location, there is some deviation between the modeled and measured data, for both the significant wave height and the peak wave period. However, the scatter index is quite low and there is generally a good correlation between modeled and measured data.

For the Árnafjørdur and Vágur locations, agreement is found between the modeled and measured data, however for the peak wave period some deviations are found. Wave direction shows larger discrepancies between modeled and measured, compared to offshore locations.

Fig. 2(a) and Fig. 2(b) show scatter plots for significant wave height and peak wave period for the east and west locations, for the time period 01-01-2012 to 31-12-2012. The figures show that the model is capable of capturing the measured significant wave height data quite well. The majority of the peaks in significant wave height are captured by the model, however for some of the sharp peaks the model underpredicts the significant wave height. For the peak wave period there is more scatter, but the majority of the data is well-captured by the model.

Fig. 2(c) and (d) show scatter plots of the modeled and measured significant wave height and peak wave period at the north and south locations, for the period 01-04-13 to 31-12-13. The model captures the significant wave height well at both

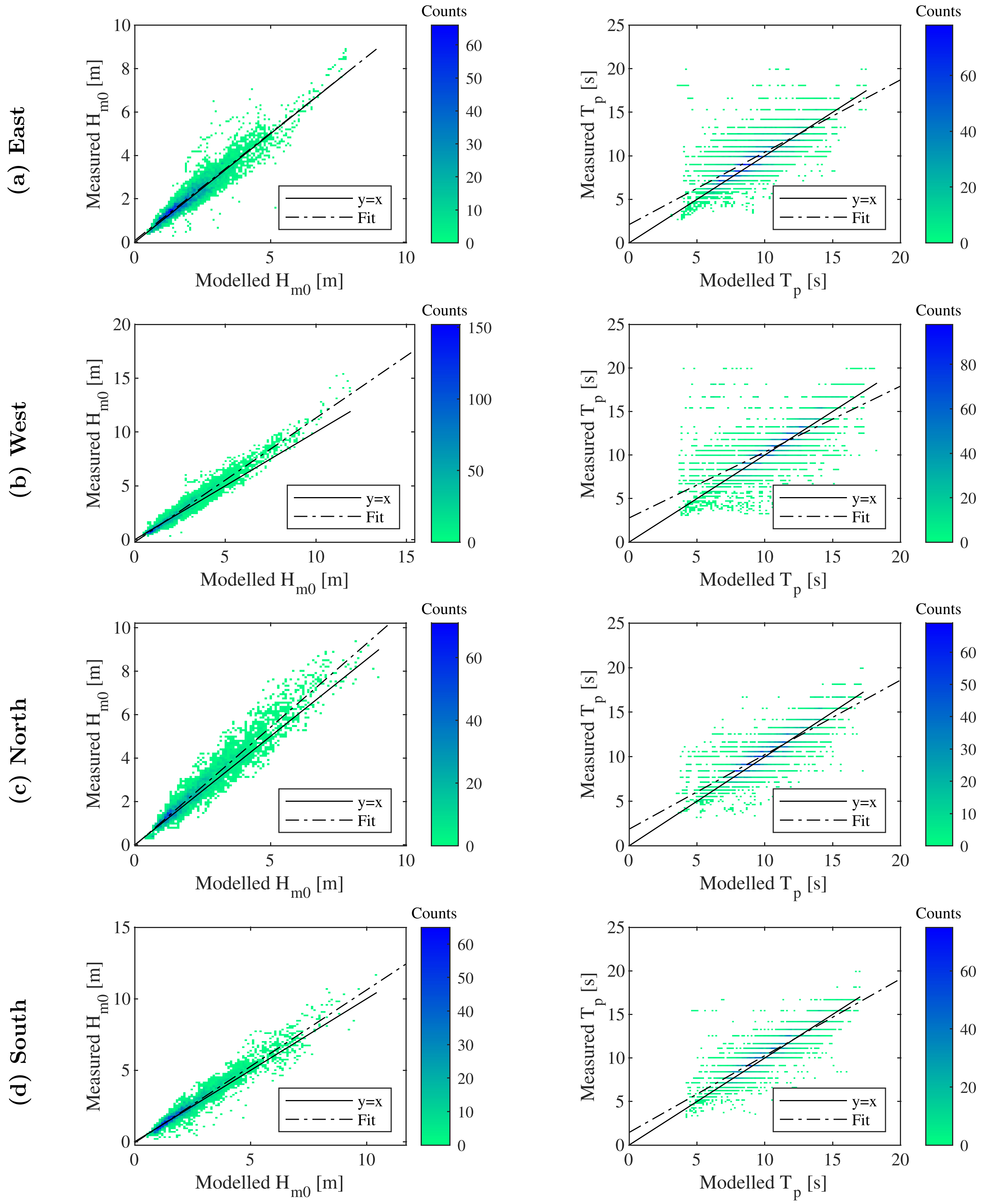

Fig. 2. Scatter plots. (a) Significant wave height H_{m0} (left) and peak wave period (right) for the east location, (b) Significant wave height H_{m0} (left) and peak wave period (right) for the west location, (c) Significant wave height H_{m0} (left) and peak wave period (right) for the north location, (d) Significant wave height H_{m0} (left) and peak wave period (right) for the south location.

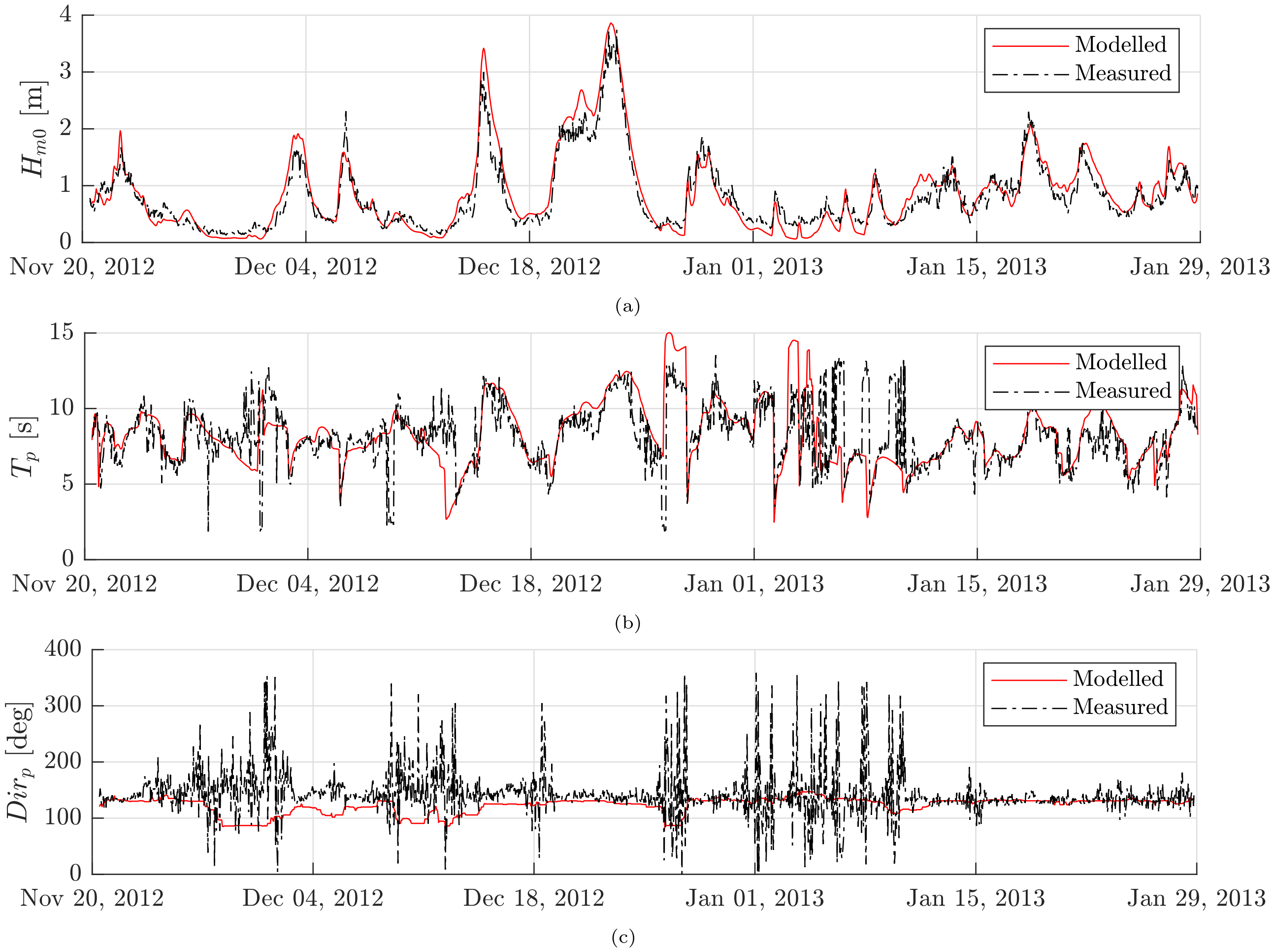

Fig. 3. Time-series of modeled and measured (a) significant wave height, (b) peak wave period and (c) peak wave direction for the Árnafjørdur location, model validation phase.

measurement locations. However, some of the peaks in the wave height are underpredicted by the model. For the peak wave period there is a bit more scatter in the comparison data, but the majority is captured by the model.

The validation statistics at the offshore buoys show comparable levels of accuracy at the different sites around the islands. However, there are discrepancies in the peak wave direction, especially for bias and RMSE. The east site has the highest level of sheltering, so an undershoot in the modeled peak wave period could indicate that the modeled sheltering was too strict compared to reality.

Fig. 3 and Fig. 4 show the time-series of the significant wave height, peak wave period and the peak wave direction for the Árnafjørdur and Vágur locations used for validating the model. The figures show agreement between model and measurements, and the majority of the peaks in significant wave height are captured by the model. There are discrepancies for the peak wave period at both locations. For the wave direction at the Árnafjørdur location, the model captures this for the majority of the time. However, in the measurements, there is a lot of spreading in the wave direction for the smaller significant wave heights. This could be caused by the fact that when a state of small waves is present, the measurement device captures waves coming from many more directions, than what is captured in the model, or that the device needs a certain signal to noise ratio, i.e. wave height, before making valid wave direction measurements. Figs. 3 and 4 show that the larger wave heights contain a more consistent wave direction, compared to the smaller wave heights. Fig. 4 shows the same phenomenon as described above for the Vágur location. However, there are larger deviations at the Vágur location than at the Árnafjørdur location. The mean wave directions in the Árnafjørdur and Vágur locations are 138° and 112°, respectively. Keeping in mind that the Árnafjørdur fjord's opening, faces in a southeastern direction and the Vágur fjords opening faces an east-southeast direction, it makes sense that the majority of the waves travel from these above mentioned directions.

One thing all of the above mentioned validation studies have in common, is the comparison quality of the peak wave direction. In all of the cases, there is quite a large deviation between the measured and the modeled data. The peak wave direction is a sensitive parameter, as it describes where the most energetic wave comes from. Furthermore, there is usually a lot of scatter associated with the peak wave direction. Unfortunately, the mean wave direction was not available from the measurements (only peak wave direction was available), as this would have introduced a more consistent wave direction, and probably given less scatter.

Mesh resolution might also play a role in the accuracy of the modeled direction compared to the measured, considering that sheltering zones might need an even higher resolution than what was applied here.

As mentioned earlier, it is of great importance to ensure the quality of the model results. Parameters such as bias and RMSE are often used for quality checks. Ref. [27] found bias values for H_{m0} ranging from −0.16 m to 0.27 m and RMSE as high as 0.45 m. Ref. [30] found bias values for H_{m0} around −0.06 m and RMSE as high as

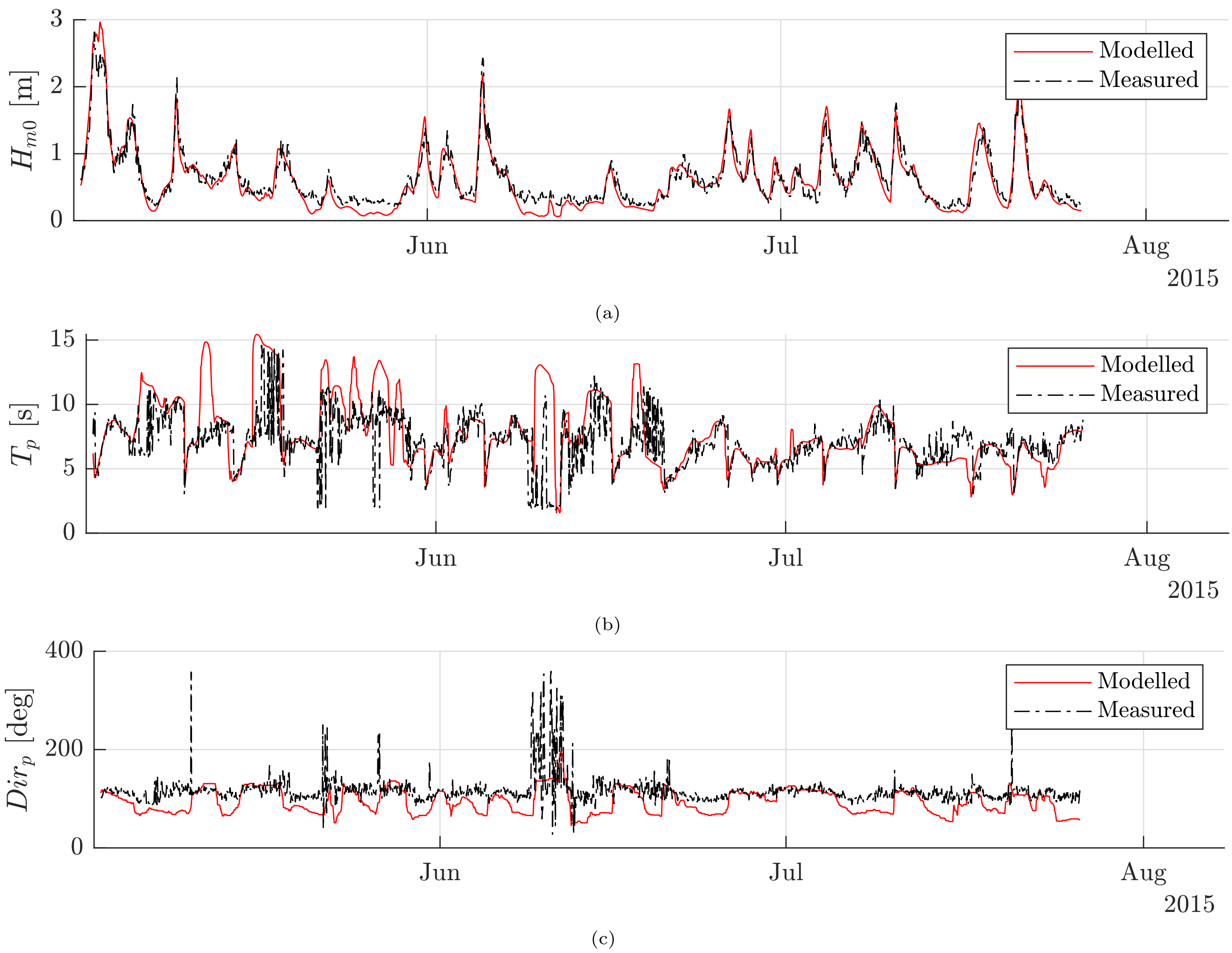

Fig. 4. Time-series of modeled and measured (a) significant wave height, (b) peak wave period and (c) peak wave direction for the Vágur location, model validation phase.

0.71 m. Ref. [31] found bias values for H_{m0} ranging from −0.01 m to −0.13 m and RMSE as high as 0.60 m. The present study shows bias values from 0.06 m to 0.19 m for the offshore locations and −0.05 m to 0.03 m for the nearshore locations. RMSE values ranging from 0.37 m to 0.52 m for the offshore locations and RMSE values of 0.15 m and 0.23 m for the nearshore locations, respectively. This leads us to conclude that the model quality is comparable to similar recent studies in the literature.

4. Results and discussion

4.1. Wave hindcasting

As the model is thoroughly validated and is able to predict the wave parameters efficiently, the next step is to investigate the spatial variation of the wave climate around the Faroe Islands. This is represented in terms of the significant wave height and the average wave energy flux. These parameters will be presented as annual mean and maximum, together with seasonal mean variation.

Fig. 5 shows the mean significant wave height for the ten year period 01-01-2009 to 31-12-2018 for the Faroese waters. The figure shows that the western and northern coasts contain higher waves than the eastern coasts. Values of about 2.4 m−3.0 m significant wave height on the western and northern coasts, and values of about 1.2 m−2.0 m in the eastern coasts.

Fig. 6 shows the maximum significant wave height for the period 01-01-2009 to 31-12-2018. A similar trend is seen here as in Fig. 5, higher waves on the western and northern coasts compared to the eastern coast. Values of about 12−14 m at the western coasts, 9−13 m at the northern coasts and about 8−9 m at the eastern coasts. We note that these results compare well with what was found in Ref. [41].

The wave energy flux, or wave power, in a sea state in arbitrary water depth, can be expressed as

$$P = \rho g \int_0^{2\pi} \int_0^{\infty} E(\sigma, \theta) c(\sigma, \theta) \mathrm{d}\sigma \mathrm{d}\theta \tag{7}$$

where $E(\sigma, \theta)$ is the energy density, $c(\sigma, \theta)$ is the group velocity, ρ is the density of water and g is the gravitational acceleration. Fig. 7 shows the mean wave energy flux calculated from Equation (7). This figure shows the same trends as the previous figures. The wave energy flux at the western and northern coasts contain a higher amount of energy than the eastern coasts. Values of wave energy flux at the western and northern coast vary from 45 kW/m to 55 kW/m. At the eastern coast the values vary from 10 kW/m to 25 kW/m.These results for the wave energy flux correspond well with what is presented in Ref. [40] in terms of the spatial variation of wave energy flux. The results in Ref. [40] are derived from the four wave measurement buoys west, south, east and north shown

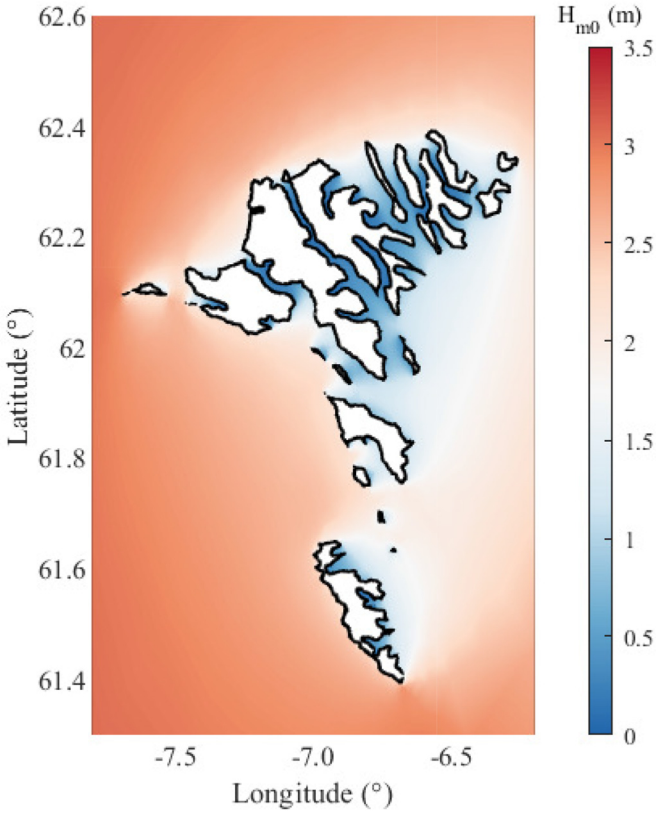

Fig. 5. Mean significant wave height for January 2009 to December 2018.

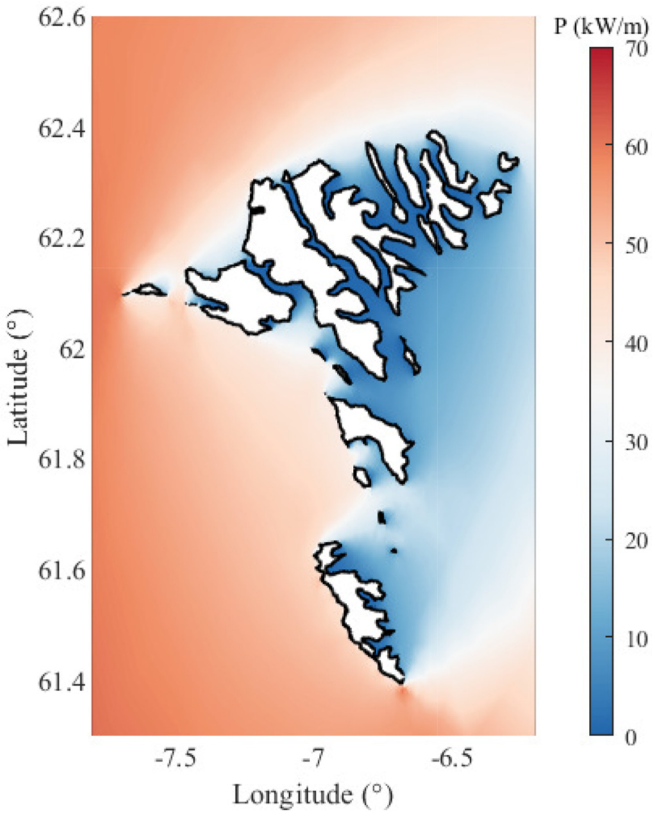

Fig. 7. Mean wave energy flux for January 2009 to December 2018.

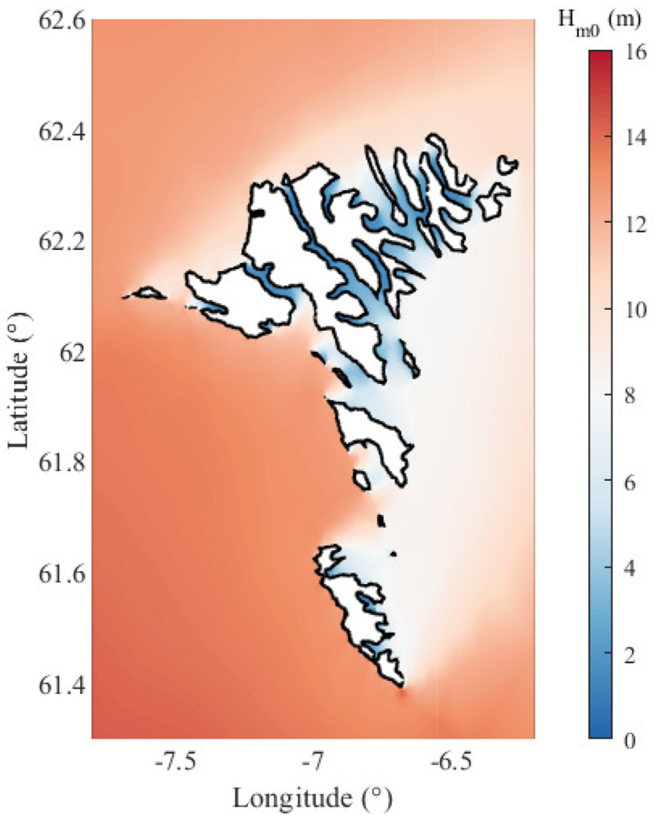

Fig. 6. Maximum significant wave height for January 2009 to December 2018.

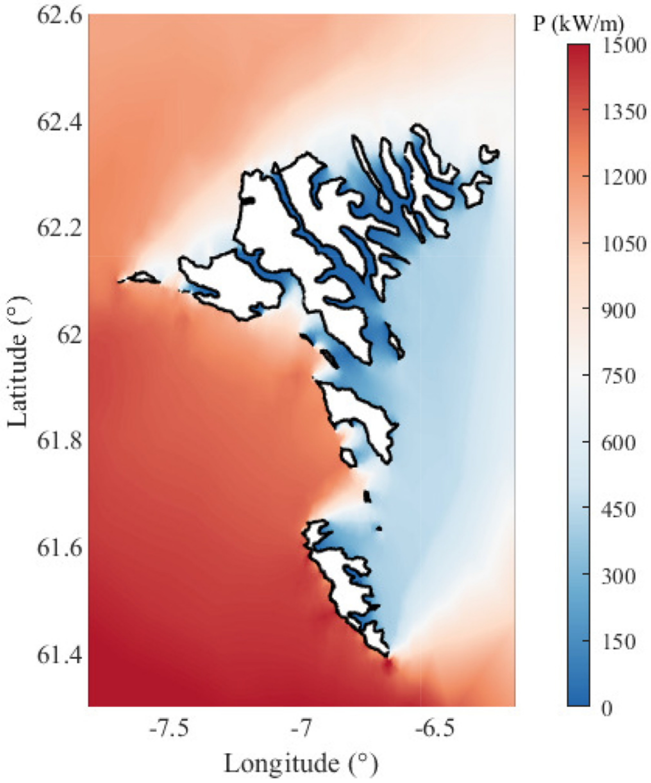

Fig. 8. Maximum wave energy flux for January 2009 to December 2018.

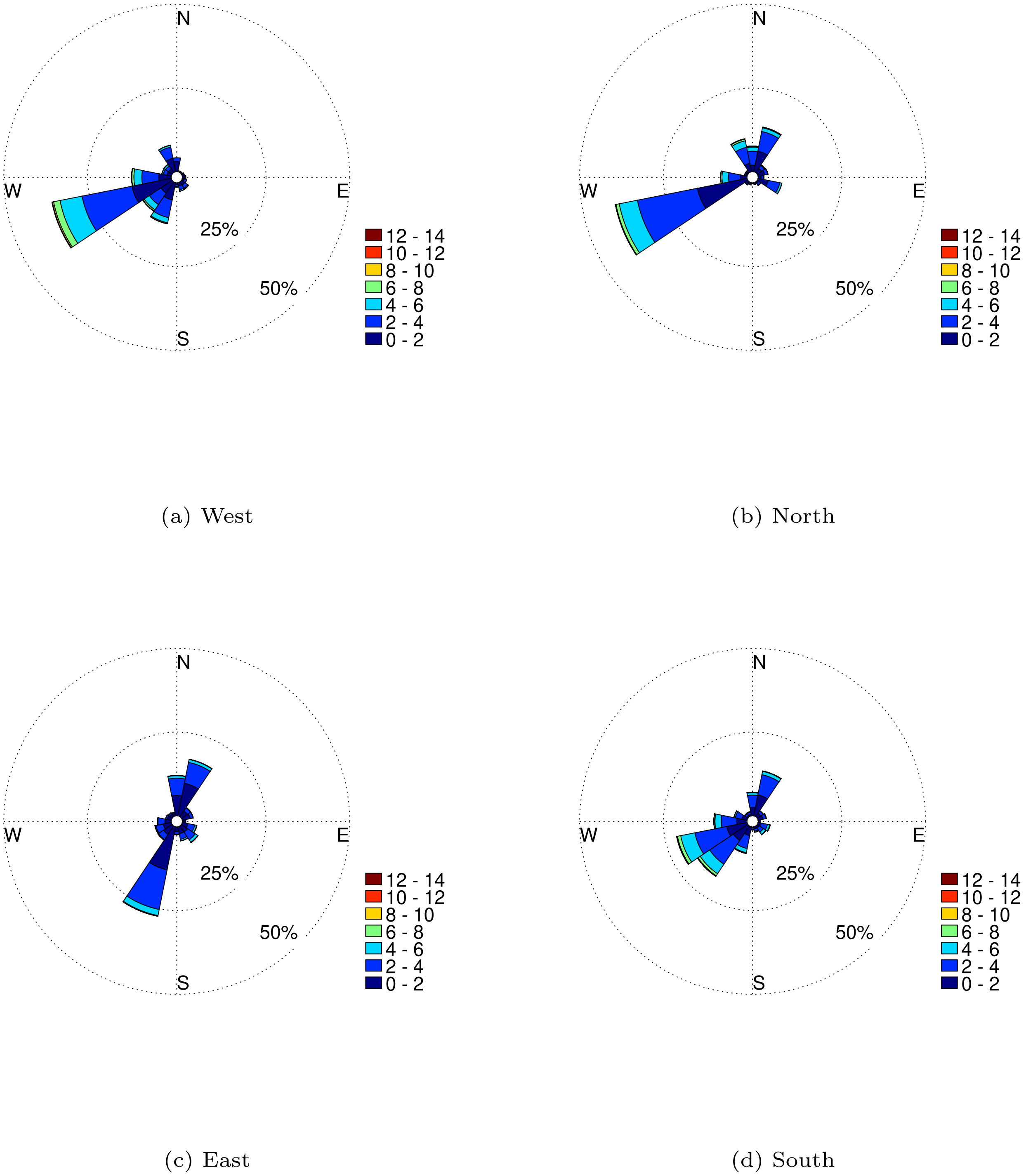

Fig. 9. Wave rose plots for the four offshore buoy locations - model results. (a) West, (b) North, (c) East and (d) South.

in Fig. 1(b).

Venugopal et al. [27] presented maps of average wave energy flux for Scottish waters. Keeping in mind that the Faroe Islands are located directly north of Scotland, the statistical values in that study are aligned with what is found in the present study. However, the values for average wave energy flux in the present study are higher closer to shore.

Fig. 8 shows the maximum wave energy flux around the Faroe Islands. Values of 1200–1500 kW/m along the western coast, 600–1000 kW/m on the northern coast and on the eastern coast, values of 300–600 kW/m.

4.2. Wave direction

As this is a study of wave power potential and it investigates the possibilities of deploying wave energy devices in the Faroe Islands, it is important to look at which direction the waves come from. To this end, wave rose plots have been compiled in order to visualize where the majority of the waves travel from.

Fig. 9 shows wave rose plots for the four offshore locations - west, east, south and north. For the west and south location, the majority of the waves travel from a west and southwesterly direction. This makes sense, since the majority of the storms that hit the Faroes travel from the mid North Atlantic Ocean. For the north location the majority of the waves travel from the west and north. The north buoy measurement location is not in a sheltered zone, when storms travel from the mid North Atlantic (southwest direction), hence the large number of occurrences from the west. The north location also shows high occurrence from the north, while the west and south locations do not to the same extent. This is natural, since these buoys are largely sheltered from waves coming from the north.

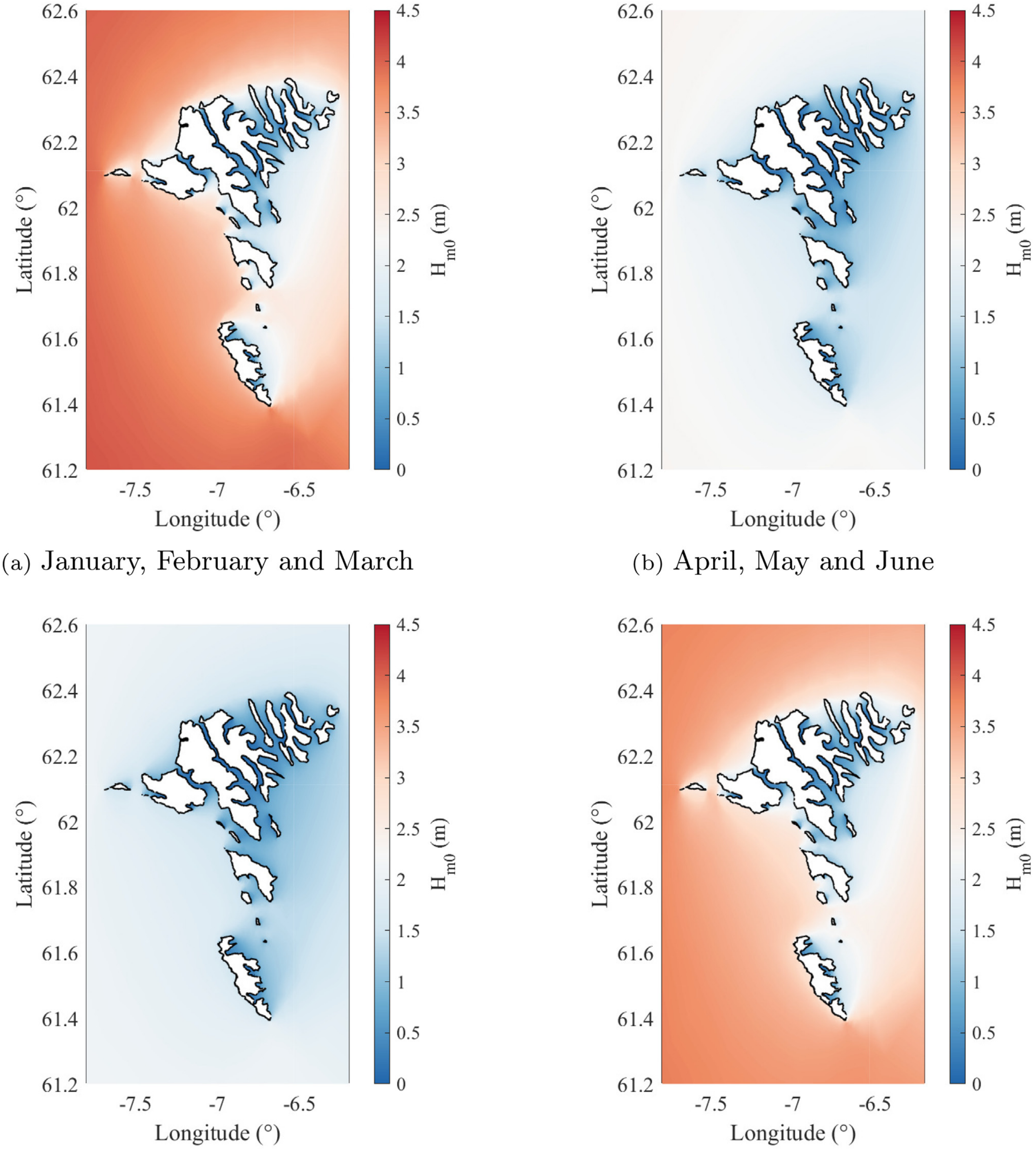

(a) January, February and March
(b) April, May and June
(c) July, August and September
(d) October, November and December

Fig. 10. The seasonal variation of the mean significant wave height of the four considered seasons. (a) January, February and March, (b) April, May and June, (c) July, August and September, (d) October, November and December.

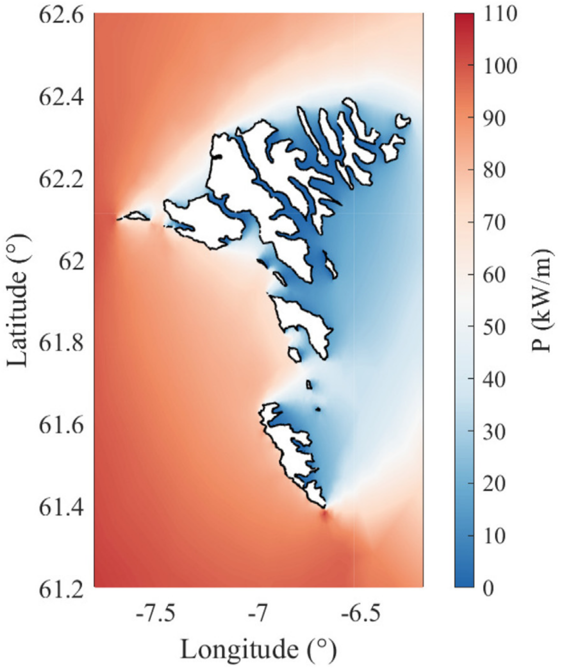

(a) January, February and March

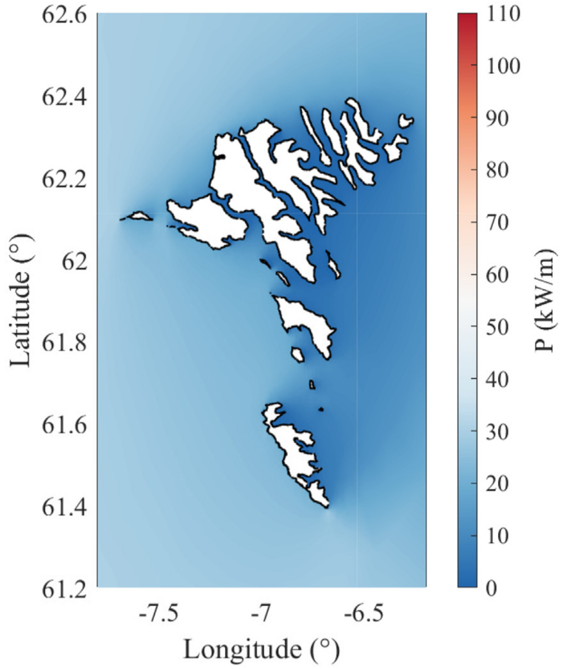

(b) April, May and June

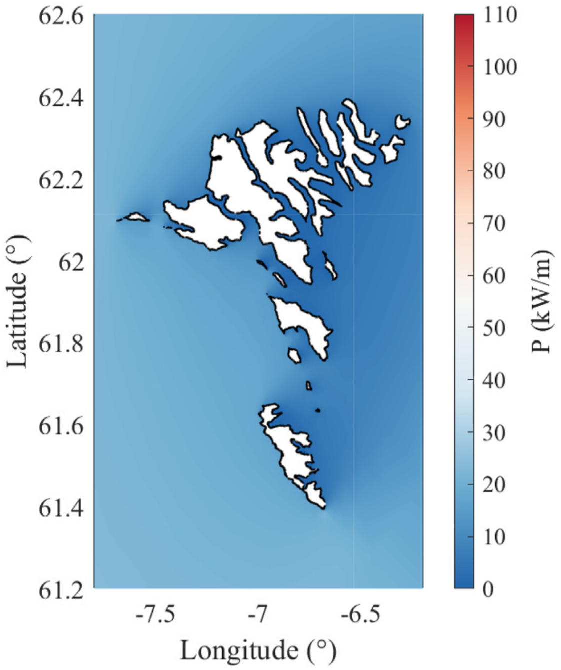

(c) July, August and September

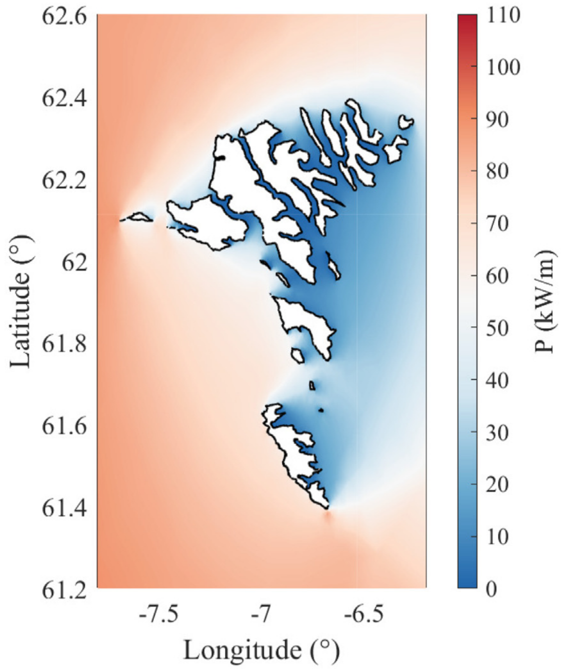

(d) October, November and December

Fig. 11. The seasonal variation of the mean wave energy flux of the four considered seasons. (a) January, February and March, (b) April, May and June, (c) July, August and September, (d) October, November and December.

For the east location the majority of the waves come from the north and south directions. If waves travel to the Faroes from a southwestern direction these will be refracted around the southern most island and be seen on the east location as traveling from a nearly southerly direction.

4.3. Seasonal variation

As the Faroe Islands are located in the North Atlantic Ocean, there are relatively large seasonal variations in the wave climate. Harsh and rough seas are normal in autumn and winter, while towards the end of spring and in summer, the seas are usually much calmer. Therefore, it is of great interest to analyze how large these variations in the wave climate are from season to season. In this study we look at each season as a three month period, starting with January. Fig. 10 shows the variation in the mean significant wave height, in each season.The figure shows, that the mean significant wave height in the winter and autumn period is much higher than in the spring and summer months. For the winter and autumn months, the mean significant wave height is 3–4 m at the western and northern coasts and 1.5–2.5 m at the eastern coasts. In the spring and summer months, the mean significant wave height is 1.5–2 m at the western and northern coasts and 0.8–1.4 m at the eastern coasts.

The seasonal variation of the average wave energy flux around the islands is shown in Fig. 11. It is clear that the wave energy flux is higher in the autumn and winter months, compared to the spring and summer months.The values are 70–80 kW/m on the western and northern coasts during the autumn and winter months, and 25–35 kW/m on the eastern coasts. The wave energy flux in the spring and summer months varies between 20 kW/m and 30 kW/m along the western and northern coasts, and at the eastern coasts the wave energy flux is 5–10 kW/m.

4.4. Evaluation of the local energy potential

Information on the energy content, peak periods and wave direction is vital, at the first stage of consideration of potential wave energy device deployment. As a first step, we have selected a series of target deployment locations where we evaluate the local energy potential. Here only 3 points are investigated in more detail, as these are representative for the given offshore areas. One point is selected in the western waters, one point in the eastern waters and one point in the northern waters. In practical terms, it is important to know how much each sea-state contributes to the total available wave energy. Figs. 12–14 show the yearly average energy at each of the selected locations, along with the energy period (T_e) and the significant wave height (H_{m0}). The intensity of the colorbar shows the annual energy contribution in (MWh/m) and the numbers on the figure show the yearly average occurrence frequency of each sea-state. Isolines for the average wave energy flux are also shown.

The occurrence frequency of each sea-state is calculated by ordering the energy period (T_e) and the significant wave height (H_{m0}) in bins and counting how frequently these occur on average per year for the time period 2009–2018. The average wave energy flux is calculating using a parametrized version of Equation (7), depending on the energy period (T_e), the significant wave height (H_{m0}), the wave number based on the energy period (k_e) and the water depth h.

$$P = \frac{\rho g^2}{64\pi} H_{m0}^2 T_e \left(1 + \frac{2k_e h}{\sinh(2k_e h)}\right) \tanh(k_e h) \tag{8}$$

For the annual mean wave energy in (MWh/m) the average wave energy flux is multiplied by the hourly occurrence p_{hourly} of each sea state (H_{m0}, T_e).

$$P_{annual} = P \cdot p_{hourly} \tag{9}$$

Figs. 12–14 show that there is a higher energy content in the western and northern coasts, compared to the eastern coast. The occurrence of sea-states with shorter and smaller waves are more frequent in the eastern lying point, compared to sea-states with longer wave periods and larger wave heights dominating at the western and northern points. As a starting point, it is of course beneficial to consider sites with high energy content as these will yield a high energy production. However, considering the scatter diagram in Fig. 12, we see that the high energy content is contained in sea-states with long wave periods and large wave heights. This will in the end lead to larger wave forces, leading to stricter design considerations. Preferably, we would want the high energy content located in the "milder" sea-states, leading to a more stable production of energy.

Considering the different types of concepts for wave energy

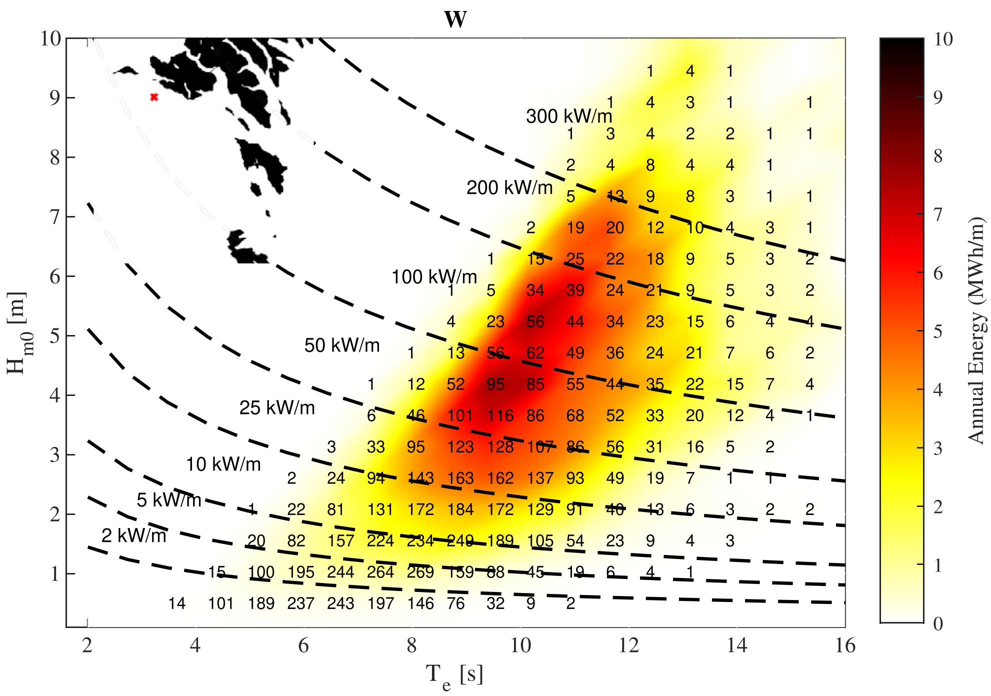

Fig. 12. Annual mean wave energy in (MWh/m) at point W, presented in terms of significant wave height H_{m0} and energy period T_e. The numbers on the plot show the occurrence per year of each sea state.

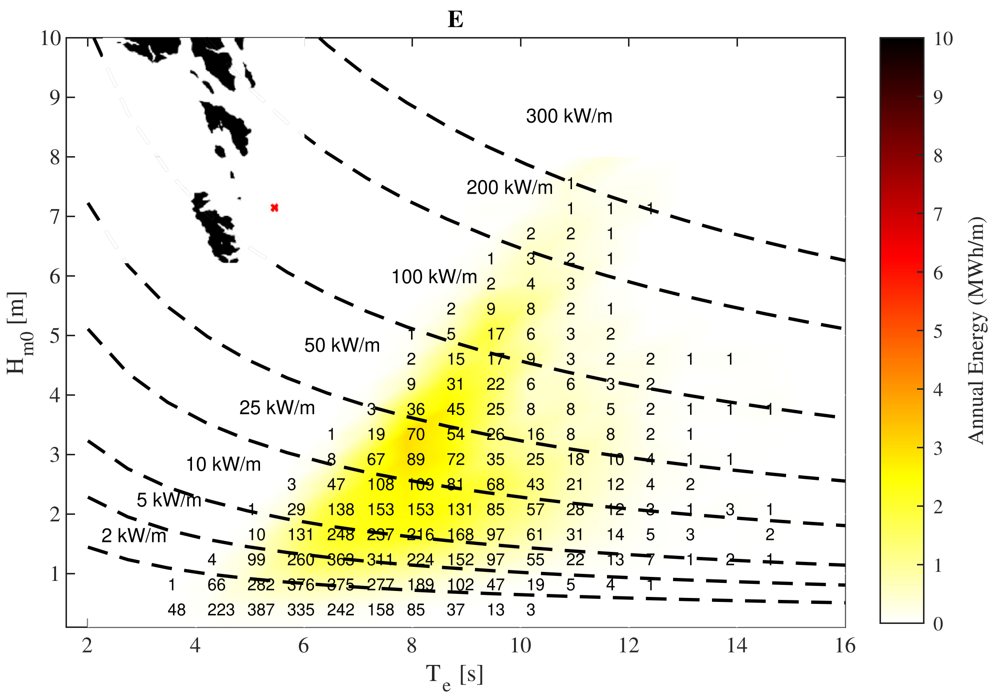

Fig. 13. Annual mean wave energy in (MWh/m) at point E, presented in terms of significant wave height H_{m0} and energy period T_e. The numbers on the plot show the occurrence per year of each sea state.

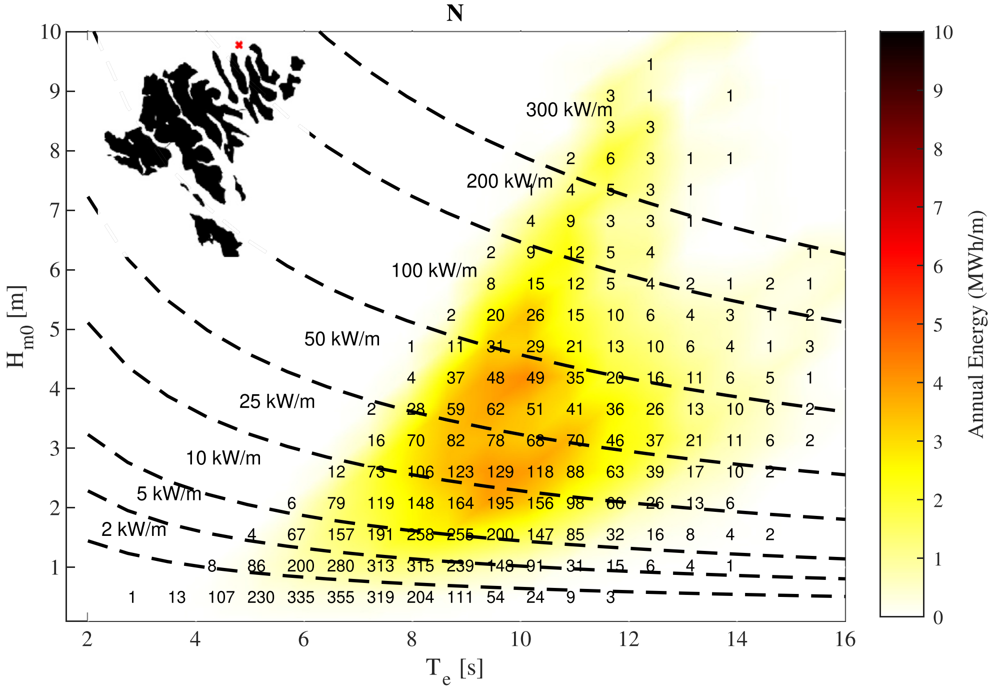

Fig. 14. Annual mean wave energy in (MWh/m) at point N, presented in terms of significant wave height H_{m0} and energy period T_e. The numbers on the plot show the occurrence per year of each sea state.

extraction, we would like to choose a design for the specific site so that the resonance wave period has a high representation in the scatter diagram. The more frequently the resonance period is represented the higher the energy output is from the device.

Table 3 shows the annual average energy content in MWh/m, the water depth and the distance to shore for each of the considered sites. The table shows the same trend as in Figs. 12–14, that the energy content is much higher at the western location, compared to eastern and northern. All three points have a relatively large water depth, when considering wave energy extraction devices, therefore floating devices are the most probable type to be installed at each location. The distance to shore varies a lot from site

Table 3
Annual average energy content, water depth and distance to shore for each of the considered sites.

Site	Annual energy	Depth	Distance to shore
[−]	[MWh/m]	[m]	[m]
W	424.9	77	5490
E	160.3	66	8650
N	264.5	89	3400

to site, giving a variation in installation costs, considering power transmission to land. However, at the northern location, the distance to shore is relatively short compared to the other locations, but the nearest islands all contain large headlands on the northern facing sites. So the actual power cable length from the north location to the nearest realistic land location is probably twice the distance shown in Table 3.

Indeed there are many things to consider before deployment of any type of wave energy extraction device. From a strict annual average energy content point of view, the western location is indeed the preferable one. However, at this location the occurrence of extreme sea-states is higher than at the other sites, leading to a longer survival mode operating time, and possibly also leading to more wear and tear on the device. If a more moderate production is desirable, the east location will be preferable, since the occurrence of milder sea-states is higher at this location.

5. Conclusions

This work developed a large scale model of the North Atlantic ocean, using the state-of-the-art wave model suite MIKE 21 SW, for hindcasting of wave parameters, specifically for the waters around the Faroe Islands. The model was forced by wind data from ECMWF at 0.25°x0.25° resolution. Furthermore, a comprehensive validation was performed using measured wave data from wave buoys both offshore and nearshore around the Faroe Islands. The validation study for the offshore buoys showed that the significant wave height was successfully reproduced, with correlation coefficients higher than 0.95. For the nearshore locations, correlation coefficients for the significant wave height were 0.96. For the peak wave period at the offshore locations, this was somewhat successfully reproduced, with correlation coefficients varying from 0.7 to 0.85. However, for the nearshore locations, the peak wave period showed higher discrepancies, with correlation coefficients of 0.53 at the Árnafjørdur site, and 0.47 at the Vágur site.Results for the statistical maximum of the significant wave height, were in agreement with a previous study [41]. Values of 12–14 m were found at the western coasts, 9–13 m at the northern coasts and 8–9 m at the eastern coasts. Furthermore, results for the annual average wave energy flux aligned with what was presented in Ref. [40], showing 45–55 kW/m at the western and northern coasts, and 10–25 kW/m at the eastern coasts.

The results of the present study show that the developed wave model can be used with high confidence to provide detailed wave statistics at suitable locations in the Faroe Islands. This will provide valuable data for initial design studies on the deployment of wave energy converters for power production and the transition to a 100% renewable supply.

Credit author contribution statement

Bárður Joensen: Conceptualization, Methodology, Validation, Formal analysis, Investigation, Data curation, Writing – original draft, Writing – review & editing, Funding acquisition, Bárður A. Niclasen: Writing – original draft, Writing – review & editing, Supervision, Harry B. Bingham: Writing – original draft, Writing – review & editing, Supervision, Project administration.

Declaration of competing interest

The authors declare that they have no known competing financial interests or personal relationships that could have appeared to influence the work reported in this paper.

Acknowledgements

This study is based on project supported by the Research Council of the Faroe Islands, grant number 02010. The same project is also financially supported by Betri Bank and SEV. The authors would like to thank Landsverk and Fiskaaling for providing the measured wave data.

References

[1] Vinnuhúsið-anonymous. Tech. rep.. In: Notat um elprísirnar til føroyskar ídnaðarfyritøkur v.m. Vinnuhúsieth; - House of Industry; 2020.
[2] Umhvørvisstovan DES. Orkugoymslur í føroyum (Accessed 01-01-2021) URL, http://www.os.fo/media/1198/orkugoymsla-i-foeroyum-web.pdf.
[3] Trondheim HM, Niclasen BA, Nielsen T, Silva FFD, Bak CL. 100% sustainable electricity in the Faroe Islands: expansion planning through economic optimization. IEEE Open Access Journal of Power and Energy 2021;8:23–34. https://doi.org/10.1109/oajpe.2021.3051917.
[4] Katsaprakakis DA, Thomsen B, Dakanali I, Tzirakis K. Faroe Islands: towards 100% R.E.S. penetration. Renew Energy 2019;135:473–84. https://doi.org/10.1016/j.renene.2018.12.042.
[5] Aderinto T, Li H. ocean wave energy converters: status and challenges. Energies 2018;11(5):1250. https://doi.org/10.3390/en11051250.
[6] Kamranzad B, Takara K. A climate-dependent sustainability index for wave energy resources in Northeast Asia. Energy 2020;209:118466. https://doi.org/10.1016/j.energy.2020.118466.
[7] Karunarathna H, Maduwantha P, Kamranzad B, Rathnasooriya H, de Silva K. Evaluation of spatio-temporal variability of ocean wave power resource around Sri Lanka. Energy 2020;200:117503. https://doi.org/10.1016/j.energy.2020.117503.
[8] Kamranzad B, Lin P. Sustainability of wave energy resources in the South China Sea based on five decades of changing climate. Energy 2020;210:118604. https://doi.org/10.1016/j.energy.2020.118604.
[9] Ris RC, Holthuijsen LH, Booij N. A third-generation wave model for coastal regions: 2. verification. J Geophys Res: Oceans 1999;104(C4):7667–81. https://doi.org/10.1029/1998jc900123.
[10] Kobayashi S, Ota Y, Harada Y, Ebita A, Moriya M, Onoda H, Onogi K, Kamahori H, Kobayashi C, Endo H, Miyaoka K, Takahashi K. The JRA-55 reanalysis: General specifications and basic characteristics. Journal of the Meteorological Society of Japan. Ser. II 2015;93(1):5–48. https://doi.org/10.2151/jmsj.2015-001.
[11] Yang Z, Neary VS. High-resolution hindcasts for U.S. wave energy resource characterization. International Marine Energy Journal 2020;3(2):65–71. https://doi.org/10.36688/imej.3.65-71.
[12] Ahn S, Haas KA, Neary VS. Wave energy resource characterization and assessment for coastal waters of the United States. Appl Energy 2020;267:114922. https://doi.org/10.1016/j.apenergy.2020.114922.
[13] Ahn S, Neary VS. Non-stationary historical trends in wave energy climate for coastal waters of the United States. Ocean Eng 2020;216:108044. https://doi.org/10.1016/j.oceaneng.2020.108044.
[14] Allahdadi MN, Gunawan B, Lai J, He R, Neary VS. Development and validation of a regional-scale high-resolution unstructured model for wave energy resource characterization along the US East Coast. Renew Energy 2019;136:500–11. https://doi.org/10.1016/j.renene.2019.01.020.
[15] The WAVEWATCH III ® Development Group. User manual and system documentation of WAVEWATCH III ® version 5.16. pp. + Appendices. Tech. Note 329. NOAA/NWS/NCEP/MMAB; 2016. p. 326.
[16] Arinaga RA, Cheung KF. Atlas of global wave energy from 10 years of reanalysis and hindcast data. Renew Energy 2012;39(1):49–64. https://doi.org/10.1016/j.renene.2011.06.039.
[17] Iglesias G, Carballo R. Choosing the site for the first wave farm in a region: a case study in the Galician Southwest (Spain). Energy 2011;36(9):5525–31. https://doi.org/10.1016/j.energy.2011.07.022.
[18] Iglesias G, Carballo R. Wave resource in El Hierro—an island towards energy self-sufficiency. Renew Energy 2011;36(2):689–98. https://doi.org/10.1016/j.renene.2010.08.021.
[19] Iglesias G, López M, Carballo R, Castro A, Fraguela J, Frigaard P. Wave energy potential in Galicia (NW Spain). Renew Energy 2009;34(11):2323–33. https://doi.org/10.1016/j.renene.2009.03.030.

[20] The WAMDI Group. The WAM model—a third generation ocean wave prediction model. J Phys Oceanogr 1988;18(12):1775−810. https://doi.org/10.1175/1520-0485(1988)018<1775:TWMTGO>2.0.CO;2.
[21] Kalnay E, Kanamitsu M, Kistler R, Collins W, Deaven D, Gandin L, Iredell M, Saha S, White G, Woollen J, Zhu Y, Leetmaa A, Reynolds R, Chelliah M, Ebisuzaki W, Higgins W, Janowiak J, Mo KC, Ropelewski C, Wang J, Jenne R, Joseph D. The NCEP/NCAR 40-year reanalysis project. Bull Am Meteorol Soc 1996;77(3):437−71. https://doi.org/10.1175/1520-0477(1996)077<0437:tnyrp>2.0.co;2.
[22] Cats G, Wolters L. The hirlam project [meteorology]. IEEE Comput Sci Eng 1996;3(4):4−7. https://doi.org/10.1109/99.556505.
[23] Iglesias G, Carballo R. Wave energy potential along the death coast (Spain). Energy 2009;34(11):1963−75. https://doi.org/10.1016/j.energy.2009.08.004.
[24] Iglesias G, Carballo R. Offshore and inshore wave energy assessment: asturias (N Spain). Energy 2010;35(5):1964−72. https://doi.org/10.1016/j.energy.2010.01.011.
[25] Rusu E, Soares CG. Numerical modelling to estimate the spatial distribution of the wave energy in the Portuguese nearshore. Renew Energy 2009;34(6): 1501−16. https://doi.org/10.1016/j.renene.2008.10.027.
[26] Iglesias G, Carballo R. Wave energy and nearshore hot spots: the case of the SE Bay of Biscay. Renew Energy 2010;35(11):2490−500. https://doi.org/10.1016/j.renene.2010.03.016.
[27] Venugopal V, Nemalidinne R. Wave resource assessment for Scottish waters using a large scale North Atlantic spectral wave model. Renew Energy 2015;76:503−25. https://doi.org/10.1016/j.renene.2014.11.056.
[28] DHI. MIKE 21 Spectral waves FM, user guide. Hørsholm, Denmark DHI, Agern Allé 2017;5:2970.
[29] ECMWF (Accessed 01-01-2021), https://cds.climate.copernicus.eu/.
[30] Rusu L, Soares CG. Wave energy assessments in the Azores islands. Renew Energy 2012;45:183−96. https://doi.org/10.1016/j.renene.2012.02.027.
[31] Rusu E, Soares CG. Wave energy pattern around the Madeira Islands. Energy 2012;45(1):771−85. https://doi.org/10.1016/j.energy.2012.07.013.
[32] Sierra J, González-Marco D, Sospedra J, Gironella X, Mösso C, Sánchez-Arcilla A. Wave energy resource assessment in Lanzarote (Spain). Renew Energy 2013;55:480−9. https://doi.org/10.1016/j.renene.2013.01.004.
[33] Gonçalves M, Martinho P, Soares CG. Assessment of wave energy in the canary islands. Renew Energy 2014;68:774−84. https://doi.org/10.1016/j.renene.2014.03.017.
[34] Rusu E, Onea F. Estimation of the wave energy conversion efficiency in the Atlantic Ocean close to the European islands. Renew Energy 2016;85: 687−703. https://doi.org/10.1016/j.renene.2015.07.042.
[35] Davidsen E. Bølgeklimaet ved Fæøerne. Tech. rep. Polyteknisk læreanstalt; 1974.
[36] Etemad-Shahidi A, Kazeminezhad M, Mousavi S. On the prediction of wave parameters using simplified methods. Journal of Coastal Research (SPEC. ISSUE 2009;56:505−9.
[37] Guide to wave analysis and forecasting. Geneva, Switzerland: Secretariat of the World Meteorological Organization; 1998.
[38] Mühlestein D, Rugbjerg M. Wave atlas for the Faroe Islands. Tech. rep. DHI; 1998.
[39] Niclasen BA. An operation wave model for the Faroe Shelf. Ph.D. thesis. 2006.
[40] SeWave. Front end engineering design, tunneled wave energy converter for the Faroe Islands, tech. Rep. SeWave Ltd.; 2005.
[41] Niclasen B, Simonsen K. High resolution wave climate of the Faroe Islands. 2012.
[42] Ceverny R. 19-meter wave sets new record - highest significant wave height measured by a buoy (Accessed 01-01-2021), https://public.wmo.int/en/media/press-release/19-meter-wave-sets-new-record-highest-significant-wave-height-measured-buoy.
[43] DHI. MIKE 21 Wave modelling, spectral waves FM, short description. Hørsholm, Denmark DHI, Agern Allé 2017;5:2970.
[44] Komen GJ, Cavaleri L, Donelan M, Hasselmann K, Hasselmann S, Janssen PAEM. Dynamics and modelling of ocean waves. Cambridge University Press; 1994. https://doi.org/10.1017/cbo9780511628955.
[45] Janssen P. Wave induced stress and the drag of airflow over sea waves. J Phys Oceanogr 1989;19:745−54.
[46] Janssen P. Quasi-linear theory of wind wave generation applied to wave forecasting. J Phys Oceanogr 1991;19:1631−42.
[47] Hasselmann S, Hasselmann K, Allender J, Barnett T. Computations and parameterizations of the nonlinear energy transfer in a gravity wave spectrum. Part ii: parameterizations of the nonlinear transfer for application in wave models. J Phys Oceanogr 1985;15(11):1378−91.
[48] General bathymetric charts of the Oceans. GEBCO (Accessed 01-01-2021). URL, https://www.gebco.net/.
[49] Simonsen K, Larsen K, Mortensen L, Norbye A. New bathymetry for the Faroe Shelf, tech. Rep. University of the Faroe Islands; 2002.
[50] A. Wiese, J. Staneva, J. Schultz-Stellenfleth, A. Behrens, L. Fenoglio-Marc, J.-R. Bidlot, Synergy between satellite observations and model simulations during extreme eventsdoi:10.5194/os-2018-87.
[51] DHI. MIKE 21 spectral wave module. Scientific documentation; 2017.
[52] Nortek. Wave systems - AWAC (Accessed 01-01-2021). URL, http://195.62.126.26/en/products/wave-systems/awac.
[53] Davidsen E, Hansen B. The Faroese wave- and current-measuring project. Coast Eng 1981;5:111−23. https://doi.org/10.1016/0378-3839(81)90010-7.
[54] Niclasen B, Simonsen K. Note on wave parameters from moored wave buoys. Appl Ocean Res 2007;29(4):231−8. https://doi.org/10.1016/j.apor.2008.01.003.
[55] Landsverk. Webpage (Accessed 01-01-2021). URL, https://www.landsverk.fo.

Chapter 4

Evaluation of the power performance of various wave energy conversion concepts for Faroese coastal waters

The paper entitled ”Evaluation of the power performance of various wave energy conversion concepts for Faroese coastal waters” has been published in Developments in Renewable Energies Offshore as:

Bárdur Joensen, Harry B. Bingham, and Bárdur A. Niclasen. “Evaluation of the power performance of various wave energy conversion concepts for Faroese coastal waters”. In: *Developments in Renewable Energies Offshore*. CRCPress/Balkema, 2021, pp. 96–102. ISBN: 9780367681319

Developments in Renewable Energies Offshore – Guedes Soares (Ed.)
© 2021 Taylor & Francis Group, London, ISBN 978-0-367-68131-9

Evaluation of the power performance of various wave energy conversion concepts for Faroese coastal waters

B. Joensen
LBF Consulting Engineers, Tórshavn, Faroe Islands
Department of Mechanical Engineering, Section for Fluid Mechanics, Coastal & Maritime Engineering Technical University of Denmark, Kgs. Lyngby, Denmark

H.B. Bingham
Department of Mechanical Engineering, Section for Fluid Mechanics, CoastalMaritime Engineering Technical University of Denmark, Kgs. Lyngby, Denmark

B.A. Niclasen
Department of ScienceTechnology, University of Faroe Islands, Tórshavn, Faroe Islands

ABSTRACT: The Faroe Islands, aim at having all power production based on renewable sources by 2030. Wave power is a natural option, as the islands are situated in one of the world harshest wave climates. Here we investigate the power performance of various wave energy conversion concepts in the coastal Faroese waters. The wave climate around the islands is classified using several years of modelled data from MIKE 21 SW, which has been thoroughly validated by regional and nearshore measured data. Bivariate distributions of modelled significant wave height and peak wave period, at representative nearshore locations, together with the non- dimensional power performance, are used to derive the power output from several wave energy conversion concepts. The results show that the waters around the Faroe Islands are well suited for wave energy conversion, although survivability and strong tidal currents might become an issue at some exposed sites.

1 INTRODUCTION

The extraction of energy from waves has received in- creasing attention over the past two decades or so, due to its high predictability and high energetic density (Pecher & Kofoed 2017). However, challenges still lie ahead, since the wave energy sector is still mostly in a development stage, and few wave energy extraction devices are in operation (Aderinto & Li 2018). The Faroe Islands hold a great potential of wave power production, due to the islands' location in the North Atlantic Ocean. While the energy content is high around the Faroe Islands, wave heights are also high, leading to an increased focus on survivability of wave energy devices. A study on the wave power potential for the Faroe Islands was performed by Joensen et al. (2020). The study was performed as a wave hindcast using the MIKE 21 SW wave model to set up a large scale computational domain for the ten year period 2009-2018, to characterize the spatial and temporal variation in the wave climate around the Faroe Islands. The model was set up to cover almost the entire North Atlantic Ocean, to accurately model the long swell waves which travel a long distance to reach Faroese waters. The model was thoroughly validated using regional and nearshore measured data. The results from the study show a reasonably high average wave energy flux at the western and north- ern coasts - 45-55 kW/m. The average wave energy flux was 10-25 kW/m at the eastern coasts. The study showed that there was a significant seasonal variation in the wave energy flux. For the winter and autumn months the average wave energy flux was 56- 88 kW/m at the western and northern coasts. For the eastern coasts the average wave energy flux was 16-40 kW/m. For the spring and summer months an average wave energy flux of 16-32 kW/m for the western and northern coasts, while at the eastern coasts the average wave energy flux was 4-16 kW/m.

Faroe Islands. The model was set up to cover almost the entire North Atlantic Ocean, to accurately model the long swell waves which travel a long distance to reach Faroese waters. The model was thoroughly validated using regional and nearshore measured data. The results from the study show a reasonably high average wave energy flux at the western and north- ern coasts - 45-55 kW/m. The average wave energy flux was 10-25 kW/m at the eastern coasts. The study showed that there was a significant seasonal variation in the wave energy flux. For the winter and autumn months the average wave energy flux was 56- 88 kW/m at the western and northern coasts. For the eastern coasts the

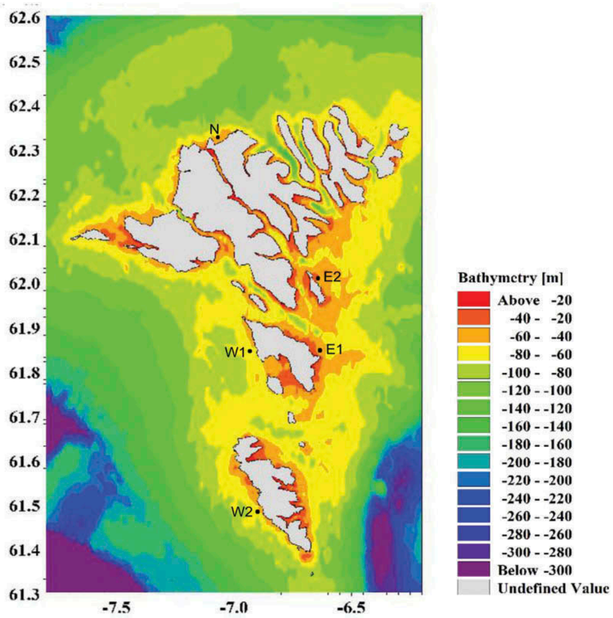

Figure 1. Map of the five locations used for study.

average wave energy flux was 16-40 kW/m. For the spring and summer months an average wave energy flux of 16-32 kW/m for the western and northern coasts, while at the eastern coasts the aver- age wave energy flux was 4-16 kW/m.

As the wave energy content is high, the study showed at the same time that there are large wave heights present in Faroese waters. At the western coasts, maximum significant wave heights of 12-14 m, at the northern coasts 9-13 m and at the eastern coasts 8- 9 m.

The peak wave period at the western and northern coast varies between 10 and 11 s. At the eastern coasts the peak wave period varies between 7 and 9 s.

In the study, directional wave roses were also computed for the east, north, west and south locations. For the west and south locations, the majority of the waves came from the west and southwest. For the east location, the waves came from the north and south, while for the north location, the majority of the waves came from the west and north.

The objective of the present study is to evaluate four types of wave energy conversion concepts at particular coastal locations in the Faroese nearshore. These particular wave energy conversion devices are: WEP- TOS, Langlee, KNSwing and the M4 wave energy converter. These mentioned wave energy conversion devices all have different working principles, which will be presented in the following section.

2 WAVE ENERGY CONVERSION DEVICES

2.1 *WEPTOS*

The WEPTOS wave energy converter (WEC) is a novel device that combines an established and efficient wave energy absorbing mechanism with a smart structure, which can regulate the amount of incoming wave energy and reduce loads in extreme wave conditions, see Kofoed et al. (2018). This adjustable A-shaped slack-moored and floating structure absorbs the energy of the waves through a multitude of rotors. The shape of the rotors is based on the renowned Salter’s Duck. On each leg, the rotors pivot around a common axle, through which the rotors transfer the absorbed power to a common power take off system. See Kofoed et al. (2018) for further description of the device.

2.2 *Langlee*

The Langlee wave energy converter (WEC), is a semi-submerged oscillating wave surge converter, see Pecher et al. (2010). Its design extracts the energy from the surge motion of the waves through two pairs of working flaps, called water wings, which are placed symmetrically opposing each other. See Pecher et al. (2010) for further description of the device.

2.3 *M4*

The original design of the M4 wave energy converter consisted of three in-line floaters increasing in diameter and draft, from bow to stern, such that the device heads naturally into the wave direction with power take off from a hinge above the mid float. This design was then extended to 6-floats, with three in the middle, one in the bow and two in the stern, see Moreno & Stansby (2019). See Moreno & Stansby (2019) for further description of the device.

2.4 *KNSwing*

This particular device is basically a ship hull, consisting of 40 oscillating water column chambers, 20 on each side, see Bingham et al. (2015). From Bingham et al. (2015) the capture width ratio from the moored device experiments are used to represent the non-dimensional performance of the WEC. See Bingham et al. (2015) for further description of the device.

3 DATA AND METHOD

3.1 *Locations for study*

For the analysis of the suitability of the different wave energy conversion types, five different locations in the Faroese nearshore have been chosen for study, see Figure 1. See also Table 1, which shows the global position, water depth, the maximum significant wave height from the 10-year hindcast study in Joensen et al. (2020), the maximum tidal current from Simonsen & Niclasen (2020) and the distance to shore.

Table 1 . The five considered locations.

Site	Lat/Long	Depth	Max H_{m0}	Max U	Dist. to shore
[-]	[deg]	[m]	[m]	[m/s]	[m]
N	62.3/-7.1	55	9.7	0.7	840
E1	61.8/-6.6	41	7.9	1.0	1680
E2	62.0/-6.6	27	7.7	0.5	1320
W1	61.8/-6.9	61	12.7	0.6	628
W2	61.5/-6.9	58	13.0	0.8	311

3.2 *Methodology*

The methodology used to evaluate the different wave energy conversion devices in this study is as follows:

- The capture width ratio η (non-dimensional performance) of the studied wave energy conversion devices as a function of wave period or wave frequency is adopted from relevant references. As the capture width ratio usually has a low variation as a function of wave height, this is not included here. The capture width ratio is defined as

$$\eta = \frac{P_{abs}}{P_{wave}L} \tag{1}$$

where P_{abs} is the power absorbed by the device, P_{wave} is the available wave power per unit crest length and L is the length scale - depending on the concept, this might either be width, length of the device or the wavelength (Pecher & Kofoed 2017).

- The spectral energy density is computed from each sea-state present at each site from the map in Figure 1. The wave spectrum is computed using the WAFO toolbox for MATLAB with H_{m0} and T_p as input, see (WAFO-group 2017). Here a JONSWAP spectrum is used, with a γ factor of 3.3.
- The average absorbed power of the device for each sea-state (SS), is defined as

$$P_{abs(SS)} = \rho g L \int_0^\infty C_g(\omega)S(\omega)\eta(\omega)d\omega \tag{2}$$

where ρ is the density of water, g is the gravitational acceleration, L is the length scale, c_g is the group velocity of the wave, S is the wave spectrum, η is the capture width ratio and ω is the wave frequency.

- The absorbed power is multiplied by the probability of occurrence of that sea-state and summed, to give the total absorbed power.

$$P_{abs(tot)} = \sum_{SS=1}^{N} P_{abs(SS)} \cdot Prob \tag{3}$$

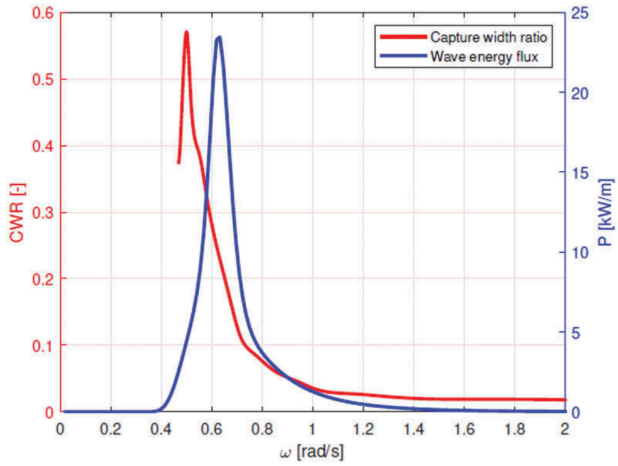

Figure 2. Demonstration of the match between capture width ratio and the wave energy flux for the particular sea-state.

where N is equal to the number of sea-states present and *Prob* is the occurrence probability of that sea-state occurring.

Lastly, the annual energy production is computed as

$$AEP = P_{abs(tot)} \cdot n_{hours} \tag{4}$$

where n_{hours} is the number of operating hours of the machine - 8760 hours if the machine is operating a - whole year (non leap year).

With commercialization of the wave energy extraction devices in mind, the full scale of the device will be much larger than the model scale of the device. This means that the capture width ratio curve will change in terms of wave period or wave frequency. A larger device has a larger resonance period than a small devices. Therefore, the capture width ratio (η) curve will shift to the right or left (with respect to period or frequency), depending on how the capture width ratio is represented, as the scale is increased. See Figure 2 for an example of the match between the capture width ratio and the contribution of the sea-state.

4 RESULTS AND DISCUSSION

The objective of the present study is to evaluate each of the selected devices at each particular location. This is presented as curves of the absorbed power for each device at each location as a function of the scale of the device compared to the model scale. Furthermore, the annual energy production of the devices are computed. The scale of each device used here, is the optimal scale, i.e. the scale that delivers the most power.

4.1 *Local wave conditions*

The information on the local wave conditions for each site are presented in Figure 3-7 as bi-variate distributions of significant wave height and peak wave period with percentage of occurrence. The data is taken from Joensen et al. (2020) and represents the period 2009- 2018.

4.2 *Absorbed power vs. scale*

As Figure 8-11 show, the maximum value (optimal scale) of the average absorbed power is reached at different scales for each location. As results from Table 2 and Figure 8-11 show, it is of great importance to conduct careful site investigation, before deployment of wave energy extraction devices. By performing these careful site investigations beforehand, a lot of material

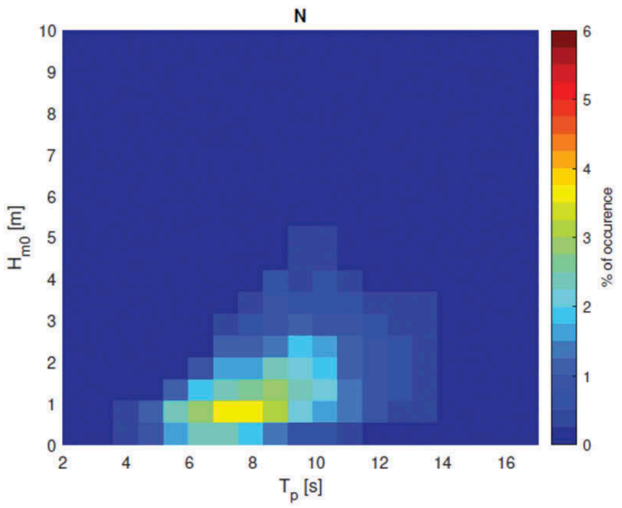

Figure 3. N - bivariate distribution of occurrences corresponding to sea-states represented by H_{m0} and T_p for the ten year period 2009-2018.

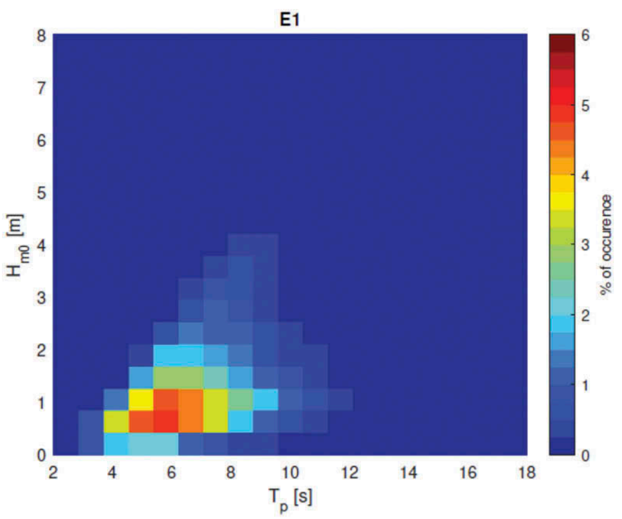

Figure 4. E1 - bivariate distribution of occurrences corresponding to sea-states represented by H_{m0} and T_p for the ten year period 2009-2018.

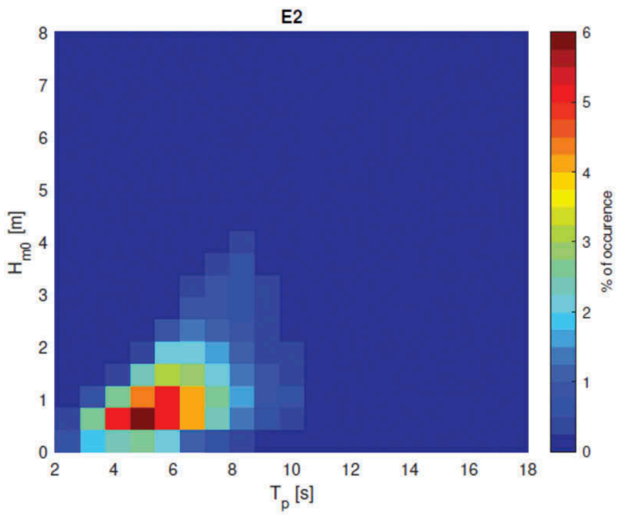

Figure 5. E2 - bivariate distribution of occurrences corresponding to sea-states represented by H_{m0} and T_p for the ten year period 2009-2018.

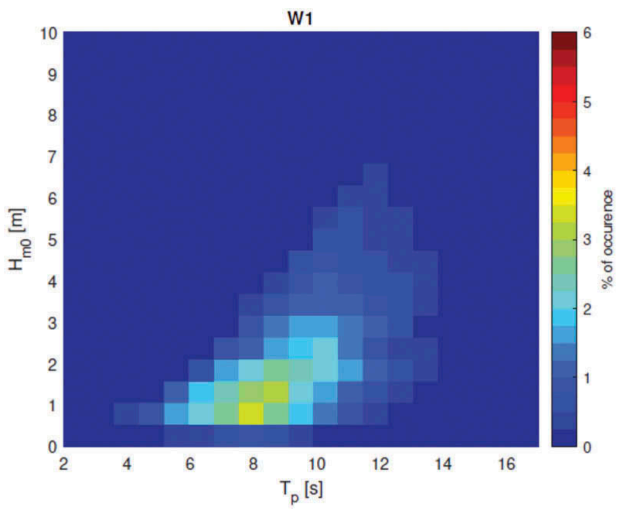

Figure 6. W1 - bivariate distribution of occurrences corresponding to sea-states represented by H_{m0} and T_p for the ten year period 2009-2018.

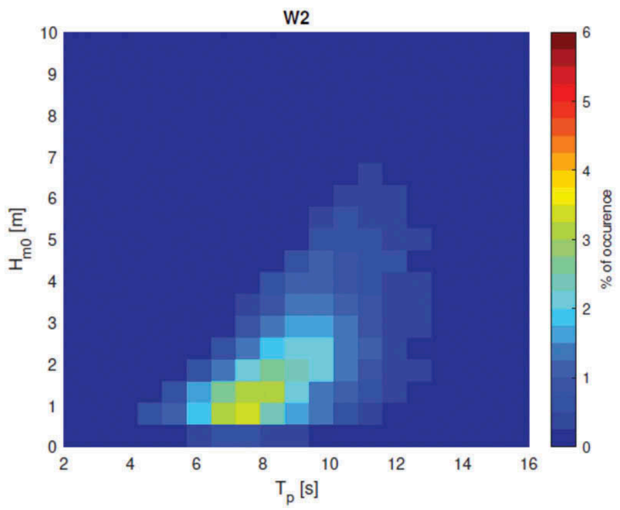

Figure 7. W2 - bivariate distribution of occurrences corresponding to sea-states represented by H_{m0} and T_p for the ten year period 2009-2018.

can be saved. Especially when considering that the maximum value of average absorbed power at one location can occur earlier compared to another location when up-scaling the device.Figure 8-11 Show the average absorbed power over the entire year of each device at each location as a function of the scale of the device, compared to the model scale used in the experiments. The figures show a difference in the maximum value (scale) of average absorbed power at each location for each device. For example, is the maximum value (scale) of average absorbed power reached at a smaller scale for the east- ern locations compared to the other locations. This is valid for all the considered devices. The figures also show that there is a great difference in the maximum value (scale) of average absorbed power at the eastern locations, compared to the western locations. Table 2 summarizes the average absorbed power of each de- vice at the optimal scale at each considered location.

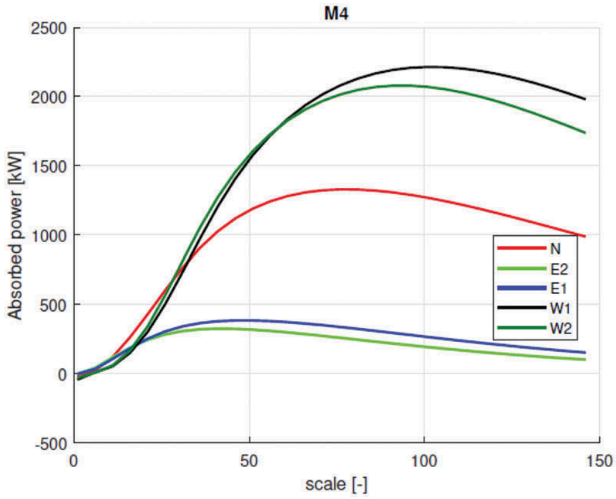

Figure 10. Absorbed power of the M4 device at the five different locations as a function of the scale of the device.

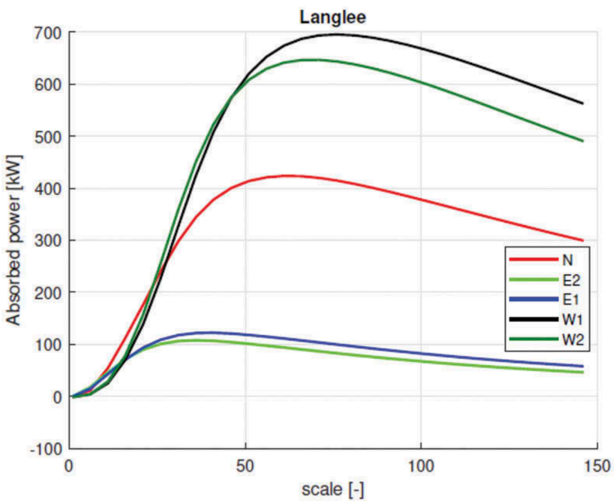

Figure 8. Absorbed power of the Langlee device at the five different locations as a function of the scale of the device.

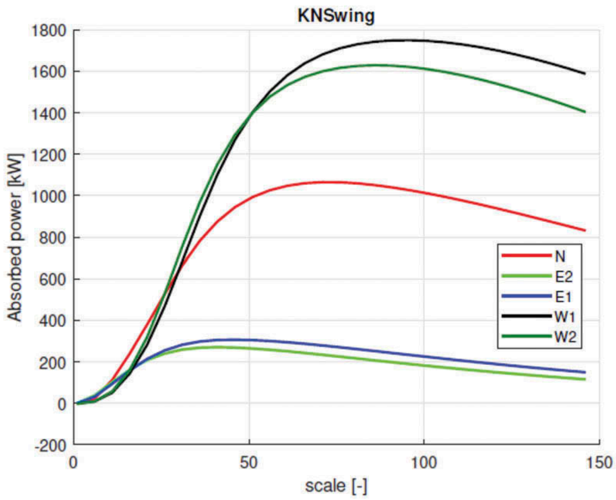

Figure 11. Absorbed power of the KNSwing device at the five different locations as a function of the scale of the device.

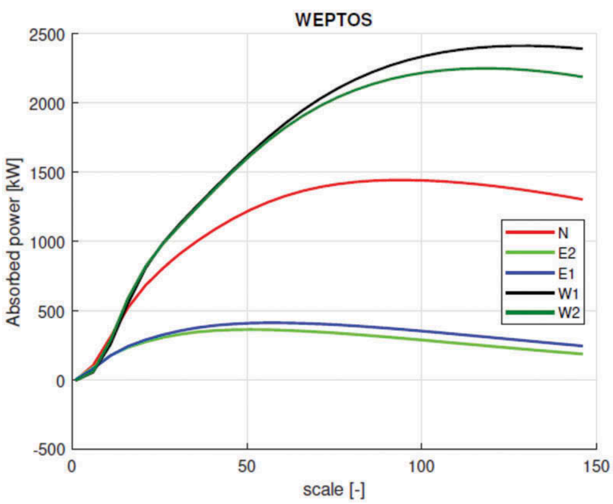

Figure 9. Absorbed power of the WEPTOS device at the five different locations as a function of the scale of the device.

Table 2 . Average absorbed power (kW) of each device at each location for the optimale scale.

Site	Weptos	M4	Langlee	KNSwing
N	1450	1350	425	1065
E1	415	385	125	305
E2	365	325	110	270
W1	2400	2200	695	1750
W2	2250	2075	650	1625

It is important to clarify here, that no considerations have been made regarding failure or maintenance of the devices, nor downtime due to survival mode. This means that the assumption here is that the machine operate for an entire year.

4.2.1 *Optimal scale*
Table 3 shows the optimal scale for each of the devices for at each location considered. As mentioned previously the scale is taken with regards to the model scale which have been tested in the references cited. For example, looking at the Langlee device at the northern location, the optimal scale here is 13 with respects to the model scale. The size of the model in the experiments in Pecher et al. (2010) was a 1.25 m by 1.25 m device, meaning that the optimal scale de- vice for the northern location would be a 16.25 m by 16.25 m device.

4.3 *Annual energy production*

Table 4 shows the annual energy production of the different devices at each location for the optimal scale of the devices, i.e. the scale yielding the most power. The annual energy production in Table 4 is only derived from the absorbed mechanical power. The final energy production depends on the power take-off (PTO) system used for each concept. The PTO systems vary in working principle, but they also vary a lot in efficiency (Pecher & Kofoed 2017).

As the wave energy resource in Faroese coastal waters is high, survivability of the devices could become an issue, because of the relatively large wave heights at the more exposed sites. The western lying locations yield the highest energy production and absorbed power for all devices. However, the western lying locations also have the highest maximum significant wave height, see Table 1.

Table 3 . Optimal scales for each device at each location.

Site	Weptos	M4	Langlee	KNSwing
N	20	16	13	15
E1	12	10	9	10
E2	11	9	8	9
W1	27	21	16	20
W2	24	19	15	18

Table 4 . Annual energy production (GWh) of each device at each location for the optimal scale.

Site	Weptos	M4	Langlee	KNSwing
N	12.6	11.6	3.7	9.3
E1	3.6	3.3	1.1	2.7
E2	3.2	2.8	1.0	2.4
W1	21.5	19.4	6.1	15.3
W2	19.7	18.2	5.7	14.3

Since the devices considered in this study are all floating devices, mooring design might become an issue at some exposed sites, due to the strong currents.

4.4 *Future work*

Future work will hold a study of more device types, together with more locations for consideration in Faroese coastal waters. Furthermore, an economic study to yield the levelised cost of energy (LCOE) for each device, together with the most optimal scale of each device, with respects to energy production and capital expenditure.

5 CONCLUSIONS

In this paper we have highlighted the importance of careful site investigation before deployment of wave energy devices for power production. The out- put power from two devices of the same concept deployed at different locations might be very different. The study also showed that Faroese coastal waters are well suited for wave energy extraction. However, large wave heights and strong currents might become an issue regarding survivability of the devices and mooring design.

ACKNOWLEDGEMENTS

This study is based on project supported by the Research Council of the Faroe Islands, grant number 02010. The same project is also financially supported by Betri Bank and SEV.

REFERENCES

Aderinto, T. & H. Li (2018, may). Ocean wave energy con- verters: Status and challenges. *Energies 11*(5), 1250.

Bingham, H. B., D. Ducasse, K. Nielsen, & R. Read (2015, jul). Hydrodynamic analysis of oscillating water column wave energy devices. *Journal of Ocean Engineering and Marine Energy 1*(4), 405–419.

Joensen, B., B. A. Niclasen, & H. B. Bingham (2020). Wave power assessment in Faroese waters using a large scale spectral wave model. Manuscript submitted for publication.

Kofoed, J. P., A. Tetu, F. Ferri, L. Margheritini, N. Sonalier, & T. Larsen (2018, jun). Real Sea Testing of a Small Scale Weptos WEC Prototype. In *Volume 10: Ocean Renewable Energy*. American Society of Mechanical Engineers.

Moreno, E. C. & P. Stansby (2019). Experimental assessment of a 6-float M4 wave energy converter. In *Advances in Renewable Energies Offshore*, pp. 401–407. Taylor & Francis Group, London.

Pecher, A., J. Kofoed, J. Espedal, & S. Hagberg (2010). Results of an experimental study of the Langlee wave energy converter. In *Proceedings of the Twentieth (2010) International Offshore and Polar Engineering Conference*, Volume 1, pp. pp. 877–885.

Pecher, A. & J. P. Kofoed (Eds.) (2017). *Handbook of Ocean Wave Energy*. Springer International Publishing.

Simonsen, K. & B. Niclasen (submitted 2020). On the energy potential in the tidal streams on the faroeshelf. *Renewable Energy*.

WAFO-group (2017). *WAFO - a matlab toolbox for analysis of random waves and loads - a tutorial*. Math. Stat., Center for Math. Sci., Lund Univ., Sweden.

Chapter 5

Hydrodynamic analysis of one-way energy capture by an oscillating water column wave energy device

The paper entitled ”Hydrodynamic analysis of one-way energy capture by an oscillating water column wave energy device” is a revised version under review for publication in the Journal of Energy Reports as:

Bárdur Joensen et al. “Hydrodynamic analysis of a one-way energy capture of an oscillating water column wave energy device”. In: *Journal of Energy Reports (In review)* (2022)

Hydrodynamic analysis of one-way energy capture by an oscillating water column wave energy device

Bárður Joensen[a,b,*], Harry B. Bingham[b], Robert W. Read[b], Kim Nielsen[c], Jokin Brito Trevino[c]

[a] *LBF Consulting Engineers, Niels Finsensgøta 10, FO-110 Tórshavn, Faroe Islands*
[b] *Technical University of Denmark, Department of Civil and Mechanical Engineering, Section for Fluid Mechanics, Coastal and Maritime Engineering, Nils Koppels Allé, Building 403, 2800 Kgs. Lyngby, Denmark*
[c] *Rambøll A/S, Hanemanns Allé 53, 2300 Copenhagen, Denmark*

Abstract

This work evaluates the hydrodynamic performance of an oscillating water column wave energy converter, with a focus on comparing conventional two-way energy capture to one-way energy capture where only the up- or down-stroke is used drive the turbine. Small-scale model test experiments are performed, and numerical calculations are made using weakly-nonlinear potential flow theory. The air turbine is represented experimentally by an orifice plate with a flow area equal to about 1% of the internal-chamber water-plane area. One-way energy capture by the experimental model is realized by incorporating a passive, low-inertia, non-return valve which vents the air inside the chamber on one half-cycle of the internal water-column oscillation. In the numerical calculations, there is little difference between the two venting configurations, due to the simplified weakly non-linear model. However, the experimental results show that up-stroke venting generally yields a higher power absorption than down-stroke venting and the two-way energy capture generally yields a higher power absorption compared to the one-way energy capture. The calculations agree well with the experiments for two-way absorption, but substantially over-predict the absorbed power in the one-way configuration. This is mainly attributed to the imperfect venting system in the physical model, but further tests and/or CFD calculations are needed to confirm this conclusion.

Keywords: Wave energy conversion, Experimental model testing, Oscillating water column, Valve system

1. Introduction

Global emissions of carbon dioxide and other damaging pollutants must be reduced. To achieve this, fossil-fuel based energy production must be replaced with zero-emissions alternatives. Wave energy is a viable candidate for this. However, given that the wave energy conversion (WEC) industry is still at a pre-commercial stage, cost-efficient technologies to produce energy must still be proven. The oscillating water column (OWC) concept is arguably one of the more promising technologies, due to its simplicity and the fact that it has no moving parts in the water. It is therefore one of the most extensively studied and tested concepts [1].

The conventional OWC consists of an internal air chamber with an opening below the water surface. An air turbine is attached to the top of the air chamber. As the waves interact with the device, the internal water surface moves up and down like a piston in an engine driving air through a turbine to generate energy. Conventional OWCs are often equipped with a Wells-type turbine [2], which rotates in the same direction regardless of the air-flow direction. However, recently, more sophisticated self-rectifying turbine designs have been investigated and tested. These include the impulse turbine and the bi-radial turbine [1].

*Corresponding author
Email address: bajoe@mek.dtu.dk (Bárður Joensen)

There are two main types of OWCs: floating and fixed devices. The few grid-connected devices are fixed OWCs, for example the Mutriku power plant in the Basque Country [3], the Pico wave power plant in the Azores [4] and the Limpet power plant in Islay (which is now decommissioned) [5].

A lot of time and effort has been invested in the research and development of oscillating water column type wave energy conversion devices, both in terms of experimental studies, numerical studies, hybrid OWC concepts, and novel OWC conversion technologies. The large number of academic and technical references support this. Ref. [6] and ref. [7] review the many studies that have been conducted throughout the last 150 years or so, from whistling buoys in the late 1800s to the Mutriku breakwater wave power plant commissioned in 2011. Ref. [8] gives a review of multi-chamber OWCs, while ref. [9] gives a review on more recent advances within OWCs.

Many previous works have focused on integrating OWC plants into coastal and near-shore structures, for example the OWC power plant integrated into the Mutriku harbour breakwater [3]. Many scientific works have been published in this area. Experimental and numerical analysis for two different layouts of OWCs, were performed in [10]. They found that the integrated device was able to absorb more than twice the power of one isolated device. Other integration layouts have also been investigated. The integration of OWCs into monopile foundations for offshore wind turbines was studied in [11] and [12].

The performance of the air turbine itself has also been studied. A number of different turbines have been tested and analyzed in [13], including the Wells turbine, the bi-radial turbine, and the impulse turbine. Ref. [14] investigated a novel self-rectifying air turbine to be used in OWCs. The authors concluded that this novel turbine was slightly less efficient than a bi-radial turbine, although it is less complex and is expected to be less costly than the bi-radial turbine.

Rectifying the air flow in an OWC device allows for a uni-directional air turbine which can be substantially more efficient than existing bi-directional (or self-rectifying) turbines, but at the cost of additional complexity in the design. Several such devices have been proposed and are under development. The Tupperware device was tested with two different numerical models and small-scale experiments in [15]. The Tupperware device is a closed-circuit OWC using non-return valves and two accumulator chambers to create a smooth unidirectional flow across a unidirectional turbine. Furthermore, the UniWave device was tested in [16] and [17]. The UniWave device is a machine developed by Wave Swell Energy [18]. The concept of this device is similar to the approach used in this study - the machine is equipped with a non-return valve and a unidirectional air turbine for power generation.

1.1. Contributions and Novelty

The present study is based on the KNSwing device, an I-Beam attenuator, a ship-like structure equipped with 20 oscillating water column chambers on each side, see [19]. Two-way power absorption, motion response, and mooring loads for the device have been studied, both numerically and experimentally, and reported in: [20], [21] and [22]. The main purpose of this paper is to present experimental and computational results for a modified version of a single chamber from the KNSwing model which includes a valve system to allow for one-way venting on either the up- or the down-stroke. This is realized experimentally through a simple passive non-return valve system installed between the chamber and the orifice plate. The passive non-return valve system consists of an external box, connected to the OWC through flexible hoses. On one side of the box, a low weight, low inertia hinged flap with the same area as the chamber is mounted, as is explained in detail in Section 3. The advantage of this passive-type valve system is its simplicity however, better designs with multiple flaps and/or active valves should be developed for a real full-scale device. In the weakly-nonlinear, frequency-domain numerical calculations, this is modelled by altering the non-dimensional equivalent linear damping coefficient to only work on half of the wave cycle. For the time-domain model, the venting is implemented by assuming a perfect one-way valve.

The novel contributions of this paper are:

- We present (to our knowledge for the first time) an experimental comparison of the three available hydrodynamic energy absorption strategies for a single OWC chamber, *i.e.* two-way, up-, and down-stroke absorption.

- We present experimental evidence (to our knowledge for the first time) that more power can be absorbed by venting on the up-stroke than on the down-stroke.
- We present numerical calculations of one-way power absorption for an OWC chamber. The calculations capture the trends shown by the experimental measurements, but substantially over-predict the absorbed power for one-way venting. This is mainly attributed to the performance of the experimental venting valve.

These contributions highlight the important trade-offs that must be considered when choosing an optimal energy absorption strategy for an OWC-type wave energy device. In particular, losses associated with a more complex venting system for one-way absorption must be substantially lower than the efficiency gains associated with a one-way turbine in order to justify the extra cost and complexity.

2. Numerical modelling of OWC chambers

In this section we describe the approach for the numerical modelling of the OWC chamber, to predict the response and absorbed power of the OWC chamber tested experimentally.

The basis for the theoretical approach is the use of weakly non-linear potential flow theory in both the time- and the frequency-domains (see for example [23] and [24]). Furthermore, the orifice plate damping is modelled by assuming an incompressible air flow. We will here briefly summarize the theory, and define the standard approaches used in the calculations. The presentation closely follows that of [25], which can be consulted for further details.

2.1. Weakly non-linear potential flow modelling in the frequency domain

Two standard approaches are used to model OWC chambers using potential flow, radiation/diffraction theory. The first approach introduces new degrees of freedom to represent the pressure distribution applied to the interior free surface by the air turbine. This can be implemented in a Boundary Element Method (BEM) radiation/diffraction solver such as WAMIT [26], where the new degrees of freedom are identified as Free Surface Pressure (FSP) modes. This method was used by [21] to analyse OWC chambers. A second approach is to treat the interior free surface as a massless element of the boundary, which is predefined to move in a set of *generalized modes*. This is also implemented in WAMIT, and was applied to an OWC chamber by [25]. The generalized modes approach is more straightforward and is adopted here.

The equations of motion for a floating structure, including M_{g} generalized modes, take the form

$$\sum_{k=1}^{6+M_{\mathrm{g}}} \left[-\omega^2 \Big(M_{jk} + A_{jk} \Big) + \mathrm{i}\omega \Big(B_{jk} + B^0_{jk} \Big) + c_{jk} \right] \xi_k = X_j, \quad j = 1, 2, ..., 6 + M_{\mathrm{g}} \tag{1}$$

Here, $\xi_j(\omega)$ is the generalized body-response phasor in $6+M_{\mathrm{g}}$ (M_g = number of generalized modes) degrees of freedom, where $j = 1, 2, 3$ correspond to the translational motions in surge, sway and heave, while $j = 4, 5, 6$ correspond to the rotational motions in roll, pitch and yaw, and lastly $j = 7, 8, ..., 6 + M_{\mathrm{g}}$ are the motions of the interior free surface of the chamber. Each of the generalized body modes is defined by the boundary conditions

$$\left.\begin{aligned} \frac{\partial \phi_j}{\partial z} &= w_j(x), \quad \text{on } S_i \\ \frac{\partial \phi_j}{\partial n} &= 0, \qquad\quad \text{on } S_b \end{aligned}\right\} \quad j = 7, 8, ..., 6 + M_{\mathrm{g}}, \tag{2}$$

where ϕ_j is the radiation potential in mode j, $w_j(\mathbf{x})$ defines the vertical displacement of the interior free surface due to unit amplitude motion in mode j, S_{i} is the internal free surface, S_{b} is the submerged body surface, and $\partial/\partial n = \mathbf{n} \cdot \nabla$ represents the derivative in the direction normal to S_b, with $\mathbf{n}$ the unit normal vector and ∇ the gradient operator. M_{jk} is the linearized body inertia matrix, $A_{jk}(\omega)$ and $B_{jk}(\omega)$ are the radiation added mass and damping coefficient matrices, c_{jk} is the hydrostatic restoring coefficient matrix, and X_j is the diffraction exciting force coefficient vector. Here we assume that the incident wave can be described as a superposition of a number of linear Stokes waves at frequency ω taking the form

$$\eta_0(\mathbf{x}, t) = \Re\{A\mathrm{e}^{\mathrm{i}[\omega t - k(x\cos\beta + y\sin\beta)]}\} \tag{3}$$

$$\phi_0(\mathbf{x}, z, t) = -\Re\{\mathrm{i}\frac{gA}{\omega}\frac{\cosh k(z+h)}{\cosh kh}\mathrm{e}^{\mathrm{i}[\omega t - k(x\cos\beta + y\sin\beta)]}\}, \tag{4}$$

where, $\Re$ indicates the real part of a complex quantity, $\mathbf{x} = [x, y]$ is a horizontal position vector, and the z-axis is oriented vertically upward, with $z = 0$ at the still-water level and $z = -h$ at the fluid bottom. The free surface elevation is η_0 and ϕ_0 is the velocity potential, with g the gravitational acceleration. The incident wave has a period $T = 2\pi/\omega$, a length $\lambda = 2\pi/k$, an amplitude $A = H/2$, and it propagates in the direction defined by the angle β, measured from the positive x-axis. The linear dispersion relation, relates the wave period and the wavelength, and defines the wave phase and group velocities c and c_g

$$\omega^2 = gk\tanh kh, \quad c = \frac{\omega}{k}, \quad c_\mathrm{g} = \frac{c}{2}\left(1 + \frac{2kh}{\sinh 2kh}\right). \tag{5}$$

All the coefficients appearing in Eq. (1), except for B^0_{jk}, can be computed for any desired floating structure, using a frequency domain radiation/diffraction code, e.g. WAMIT [26]. The matrix B^0_{jk} represents the applied damping from the air turbine (or orifice plate) to the chamber and its evaluation is discussed in Section 2.3. Since this term is generally dependent on the wave amplitude, it makes the equations weakly non-linear and the solution requires iteration for each wave frequency and steepness.

2.2. Weakly non-linear potential flow modelling in the time domain

The frequency domain formulation has an equivalent formulation stated in the time-domain [27] which can be written:

$$\sum_{k=1}^{6+M_\mathrm{g}}\left[(M_{jk} + A^\infty_{jk})\ddot{x}_k(t) + \int_{-\infty}^{t} K_{jk}(t-\tau)\dot{x}_k(\tau)d\tau + c_{jk}x_k(t)\right] = F_{jD} + F_{j0}, \qquad j = 1, 2, ..., 6 + M_\mathrm{g}, \tag{6}$$

where $x_k(t)$ is the time history of the motion response in mode k, $A^\infty_{jk} = A_{jk}(\infty)$ is the infinite frequency limit of the added mass and the over-dots represent time derivatives. The radiation impulse response functions, K_{jk}, and the diffraction force, F_{jD}, are related to the frequency-response functions through the Fourier transforms

$$K_{jk}(t) = \frac{2}{\pi}\int_0^\infty B_{jk}\cos\omega t\,\mathrm{d}\omega, \qquad K_{jD}(t) = \frac{1}{2\pi}\int_{-\infty}^{\infty} X_j\mathrm{e}^{\mathrm{i}\omega t}\,\mathrm{d}\omega, \tag{7a}$$

$$F_{jD}(t) = \int_{-\infty}^{\infty} K_{jD}(t-\tau)\,\eta(\tau)\,\mathrm{d}\tau = \int_{-\infty}^{\infty}\frac{X_{jD}}{A}\hat{\eta}\,\mathrm{e}^{-\mathrm{i}\omega t}\,\mathrm{d}\omega, \tag{7b}$$

$$\hat{\eta}(\omega) = \int_{-\infty}^{\infty}\eta(t)\,\mathrm{e}^{\mathrm{i}\omega t}\,\mathrm{d}t \tag{7c}$$

where η is a particular incident wave elevation measured at the origin of the coordinate system. Here, K_{jD} is the diffraction impulse response function, and the two equivalent forms of F_{jD} indicate how the wave excitation force can be computed in either the time or frequency domains when the incident wave elevation signal is known for the all time. Other external forces applied to the body, e.g., by the air turbine or a mooring system, are represented by $F_{j0}(t)$ and can be nonlinear.

2.3. Modelling the Orifice-Plate Damping – Incompressible flow

When working at model scale, the usual assumption is that air compressibility effects are negligible. In this case, we assume that the relationship between the air flux in the chamber and the pressure drop across the orifice plate is given by

$$p(t) = \frac{1}{2}\rho_\mathrm{a}\left(\frac{1}{C_\mathrm{d}A_\mathrm{o}}\right)^2 Q(t)^2\mathrm{sign}(Q), \tag{8}$$

where ρ_a is the air density, A_o is the area of the orifice, Q is the volume flux, and C_d is a head-loss coefficient which must be determined experimentally. In [21], the orifice plate used here was found experimentally to have $C_d \approx 0.64$ and to follow Eq. (8) very closely. By defining the *generalized mode* $j = 7$ to be the *piston mode*, representing uniform vertical motion of the internal free surface of the chamber, the flux, Q, is defined as

$$Q(t) = A_\mathrm{c}\dot{x}_7, \tag{9}$$

where A_c is the internal free surface area, and $\dot{x}_7(t)$ is the surface velocity. The applied force from the orifice plate, is then given by

$$F_{70} = -A_\mathrm{c}R_0\dot{x}_7^2\,\mathrm{sign}(\dot{x}_7), \qquad R_0 = \frac{1}{2}\rho_\mathrm{a}\left(\frac{A_\mathrm{c}}{C_\mathrm{d}A_\mathrm{o}}\right)^2. \tag{10}$$

Assuming that all other mode shapes have zero mean value, these will not contribute to the air flux and thus not directly experience any damping from the orifice plate, i.e. the piston mode response is the only mode shape which directly contributes to the power absorption.

In the frequency domain, there is a need to develop an equivalent linearized damping coefficient. Assuming a sinusoidal flux at frequency ω (*i.e.* $x_7(t) = \Re\{\xi_7 e^{i\omega t}\}$), and a linear relationship between the pressure and flux, leads to

$$B_{77}^0 = \frac{8}{3\pi}\omega A_\mathrm{c}R_0|\xi_7| \tag{11}$$

as the equivalent linear damping coefficient which ensures the same power extraction per wave cycle as that defined by Eq. (10). Due to the fact that this damping coefficient depends on the chamber response, ξ_7, the solution to the equation of motion in the frequency domain, Eq. (1), is also weakly non-linear and must therefore be found iteratively for each combination of wave frequency and wave steepness. For one-way energy capture, the damping pressure is only applied over one half of the wave cycle, and Eq. (11) must be divided by two. Therefore, the equivalent linearized damping coefficient for one-way energy capture is given by

$$B_{77}^0 = \frac{4}{3\pi}\omega A_\mathrm{c}R_0|\xi_7|. \tag{12}$$

We have opted for a quadratic damping model because this is closer to the conditions produced by a bi-radial or impulse turbine which tends to have a better efficiency compared to a Wells-type turbine.

2.4. Calculation procedure

- Chamber geometry is analyzed in WAMIT [26] to get the hydrodynamic coefficients for added mass and damping (and hydrostatics) along with the excitation forces.
- The output data from WAMIT [26] is read in to MATLAB [28] and the wave parameters which are to be analyzed for are set up.
- Based on an initial guess of the chamber motion response ξ_7 and ξ_8, we iterate to find the correct linearized external damping coefficient. A maximum number of iterations is set in order to prevent an infinite loop, along with a tolerance level for the error. Then we solve Eq. (1), re-compute B_{77}^0 and repeat until the change is below the tolerance. This ensures the same power extraction per cycle as that defined by Eq. (10).

3. Experimental measurements

We provide here a description of the experimental set up and the analysis associated with the measurements. Further details can be found in [29]. Fig. 1 shows a sketch of the wave flume used for the experiments and Fig. 2 shows the model used in the experiments. Abbreviations 'WG' and 'OWC' are 'wave gauge' and 'oscillating water column', respectively.

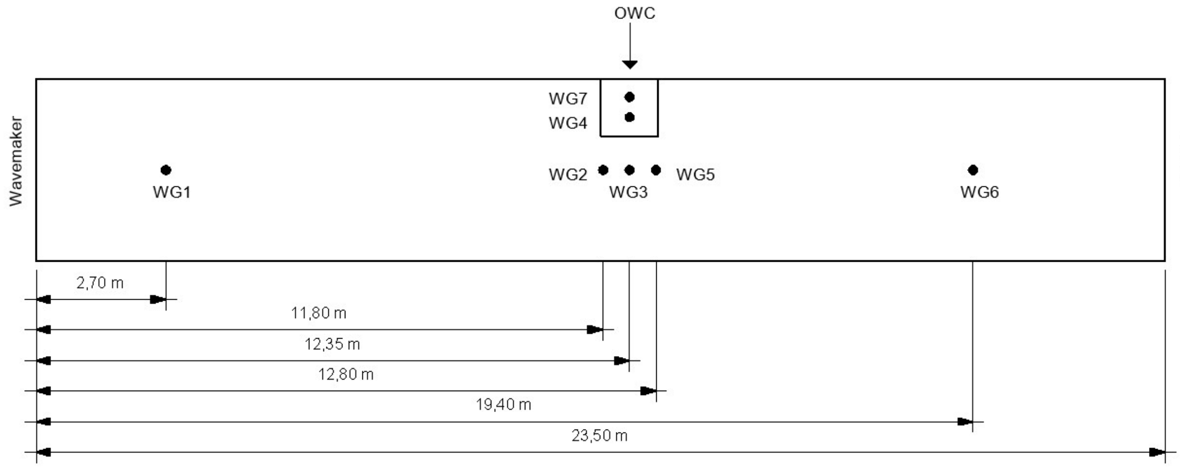

Figure 1: Layout of the experiments.

The full-scale internal chamber dimensions are 6 m by 5 m by 7.5 m in the x, y and z-directions, respectively. The model has a scale of 1:50. The used chamber dimensions give an undamped natural period of 5.78s which is tuned to be close to a typical value for the conditions in the Danish North Sea, off the northwest coast of Jutland. To apply damping and include the effects of the air turbine, a chamber lid is installed which has an orifice in the middle with a diameter of 0.8m (16mm at model-scale). Based on previous calculations using the same chamber, this orifice diameter has been found to be close to an optimum in terms of maximizing the area under the capture width ratio curve. A more detailed discussion of this topic is given in Sec. 4.2. The flume used for the experiments here measures 25 m by 0.6 m and the water depth is 0.65 m. Dimensions of the full scale and model scale are shown in Table 1

Table 1: Full scale and model scale dimensions of the OWC.

Parameter	Model scale	Full scale	Description
L [m]	0.12	6	Internal chamber length
B [m]	0.10	5	Internal chamber width
H [m]	0.15	7.5	Internal water column height
T_0 [s]	0.818	5.78	Resonance period
d_o [m]	0.016	0.8	Orifice diameter

Tests were made at a series of monochromatic wave conditions, where monochromatic is used here to indicate that only a single frequency is used in the wave-paddle signal. Two values of wave steepness are applied to each frequency, $H/\lambda = 0.025$ and 0.04. A pressure sensor from *First - Sensor*, model *BTEL5P05D4A* was used to measure the internal chamber pressure. This has an operating range from -5 mbar to +5 mbar with an accuracy of 0.5%. For measuring the surface elevation in the wave flume, together with the internal

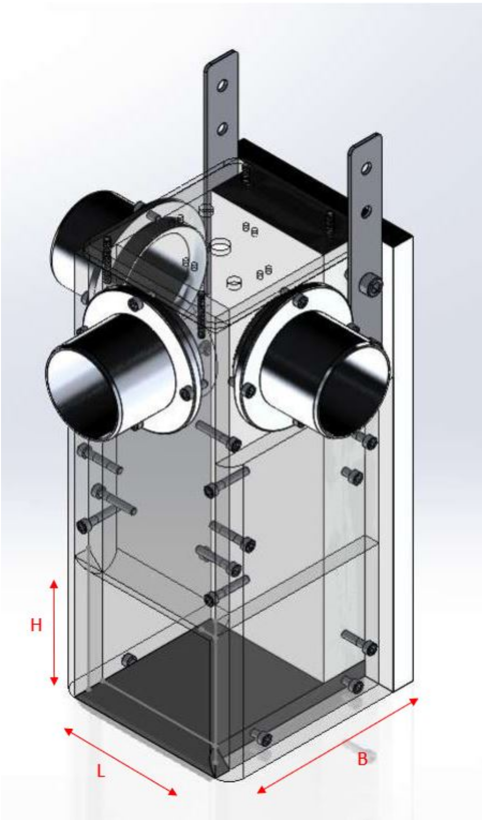

(a) 3D CAD model of the OWC chamber.

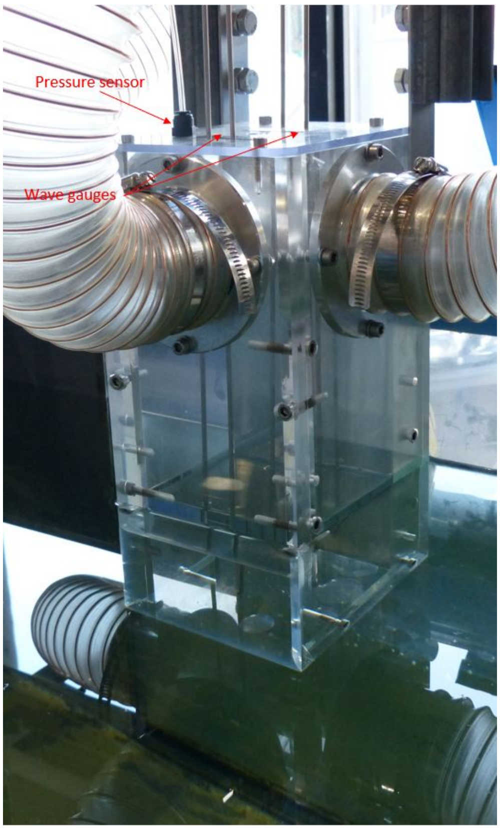

(b) Photograph of the OWC chamber in place for tests.

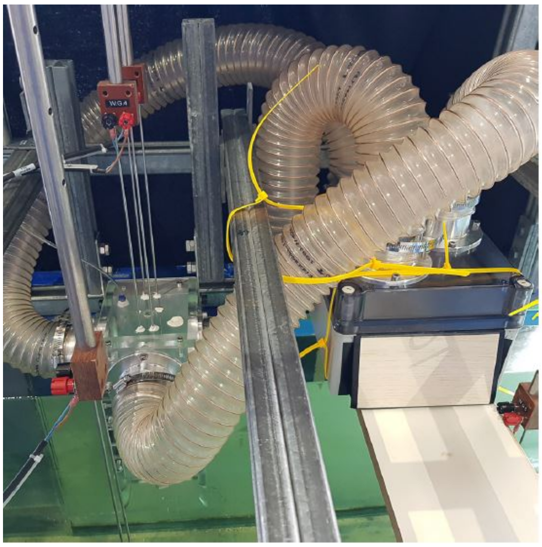

(c) Photograph of the OWC chamber, hoses and valve box.

Figure 2: OWC chamber used in the experiments.

free surface elevation in the chamber, wave measuring probes from *Edinburgh Designs* were used. Briefly speaking, these wave measuring probes mainly consist of two parallel rods which are submerged in the water and measure the electrical conductivity in the water. For more detailed information, see [30]. The rods measure 700mm in length, and the typical application of measuring is -100mm to +100mm with an accuracy 0.1mm. However it is possible to utilize almost the whole length of the wave probe rods, but at the expense of less accuracy. Two wave probes were inserted into the chamber to measure the internal free surface elevation. This was done both with the lid off and on the chamber. The two wave probes were inserted into the chamber to measure the piston mode amplitude and the first sloshing mode amplitude in the transverse direction (perpendicular to the flume wall). From visual inspection during the tests and also from video, when two-way absorption was applied, there was clear sloshing-mode activity in the cross-tank direction, but none in the direction of wave propagation. However, for one-way absorption, more complicated responses were excited as discussed further below. In total, 30 different wave conditions were tested. For varying wave height and period, two wave steepnesses were considered. See Table 2. The sampling rate used in the data acquisition was 512 Hz.

Table 2: Monochromatic wave conditions tested in the experiments.

T (s)	λ (m)	H_1 (m)	H_2 (m)	$t_{\max}$ (s)
0.57	0.51	0.013	0.021	84
0.74	0.85	0.021	0.034	65
0.78	0.94	0.024	0.038	62
0.79	0.98	0.025	0.039	60
0.81	1.02	0.026	0.041	59
0.82	1.05	0.026	0.042	58
0.83	1.07	0.027	0.043	58
0.84	1.11	0.028	0.044	57
0.86	1.15	0.029	0.046	55
0.90	1.26	0.032	0.050	52
0.98	1.49	0.037	0.060	47
1.15	1.98	0.050	0.079	38
1.31	2.48	0.062	0.099	32
1.47	2.98	0.074	0.119	27
1.64	3.46	0.087	0.138	24

In order to ensure repeatability of the tests, each condition was run 3 times. First the undisturbed wave amplitudes were established by running each condition 3 times, with no chamber placed in the flume. Second, each test condition was run three times with the chamber in place, but with no lid placed on top. This was to establish the undamped natural response of the chamber. Lastly, the lid was placed on top of the chamber in order to measure the damped response inside the chamber. In order to avoid any significant reflections disturbing the measurements on the OWC chamber, data was collected up to a time $t_{\max}$, the time required for the wave front to reach the end of the tank and return to the measurement area based on linear theory, see Table 2.

For the damped response, each condition was run three times, with a conventional configuration of the chamber, where the full wave cycle was utilized. Apart from this, a new configuration of the chamber was established, where only half of the wave cycle was utilized for power extraction. This was done in two ways. First, where the air inside the chamber was vented on the up-stroke part of the wave cycle. Second, where the air inside the chamber was vented on the down-stroke part of the wave cycle. These conditions were produced by integrating a passive one-way valve system with the chamber. It was important, since this is a passive valve system, that the valve had as little inertia as possible. Since the magnitude of the pressure difference between the inside of the chamber and the atmosphere is small, a very light material is needed for the valves. An external box was connected to the OWC chamber through flexible PVC hoses attached on the three aluminum manifolds seen in Fig. 2. The valve opening area was specifically designed to have the same resulting area as the internal free surface of the OWC chamber, in order to reduce the effect of losses in the system, e.g. pressure or friction losses. The valve flaps were made from balsa wood sheets, with thickness $t = 0.8\,\mathrm{mm}$ and a density of $150\,\mathrm{kg/m^3}$, resulting in a low-inertia valve system, as required. For the 'hinges', electric flyer hinge tape was used at the top edge of the flap, making sure to seal the complete length of the edge. To seal the edges of the flap when it was closed and subsequently ensure an air-tight seal, a 1 mm NBR rubber sheet was custom cut to fit the valve edges. As this is a passive valve system, the flaps were angled slightly in order for gravity to help close the valve flaps when required, see Fig. 3.

(a) Valve system closed.

(b) Valve system open.

Figure 3: Visualization of the passive valve system used in the experiments.

The detailed implementation of the one-way energy absorption working principle is shown in Fig. 4 for the downstroke absorption and Fig. 5 for the upstroke absorption.

To ensure a precise operation of the novel one-way absorption configuration, the pressure drop across the orifice along with the internal surface elevation was monitored. When the valve opens the pressure should be approximately zero and when the valve closes properly we should see a significant increase in the pressure measurement. Fig. 6 shows an example of the pressure measurement plotted together with the internal surface elevation, to ensure that the valve closes when expected, i.e. in the upstroke venting configuration, the valve should open when the internal surface elevation travels from the wave trough to the wave crest.

3.1. Analysis of experimental results

For the experimental measurements, the surface elevations measured by the two wave gauges placed inside the OWC chamber were used to extract the piston-mode response and the first sloshing mode response inside the chamber. Fig. 7 shows a schematic definition of the placement of the wave gauges, together with a definition of the piston and sloshing modes inside the chamber.

The wave elevation time-series $a_1(t)$ and $a_2(t)$ are assumed to be of the form

$$a_1(t) = \Re\left\{\left[\xi_7 + \xi_8 \cos\left(\frac{\pi}{W} c_1\right)\right] \mathrm{e}^{\mathrm{i}\omega t}\right\}, \tag{13}$$

$$a_2(t) = \Re\left\{\left[\xi_7 + \xi_8 \cos\left(\frac{\pi}{W} (W - c_2)\right)\right] \mathrm{e}^{\mathrm{i}\omega t}\right\}, \tag{14}$$

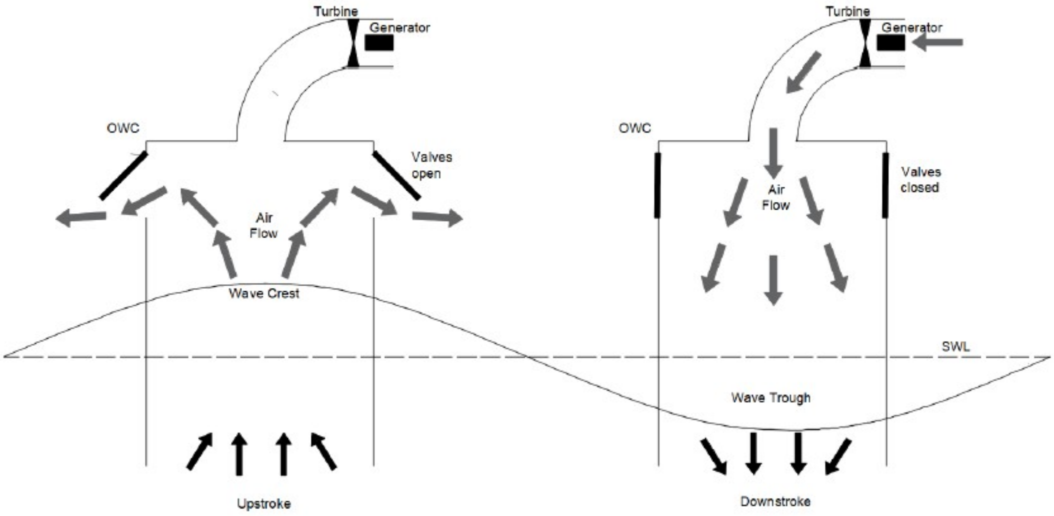

Figure 4: Working principle of one-way energy absorption on the downstroke.

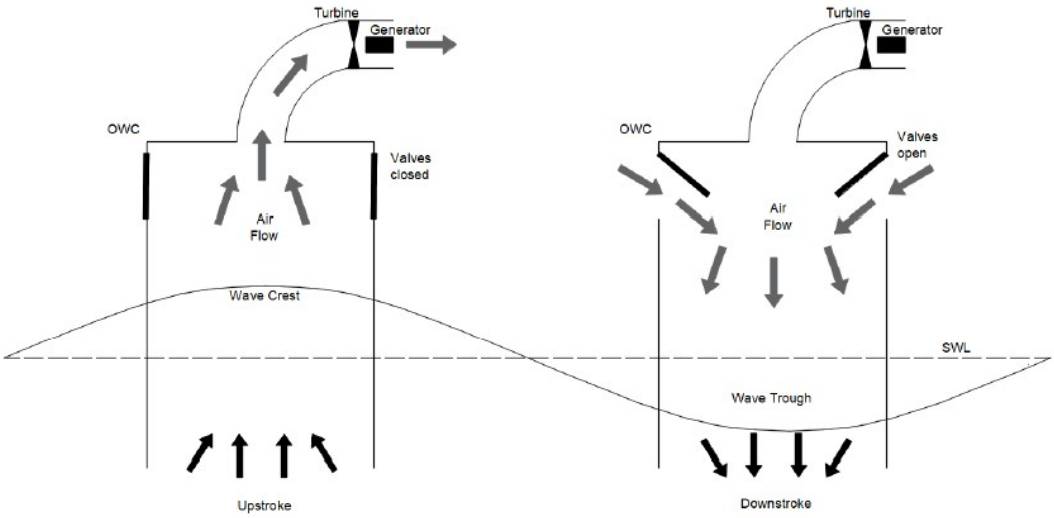

Figure 5: Working principle of one-way energy absorption on the upstroke.

where W is the internal chamber width. We can define the sum and difference elevations as

$$a^+ = a_1 + a_2 = \Re\left\{\left[2\xi_7 + \xi_8\left(\cos\left(\frac{\pi}{W}c_1\right) + \cos\left(\frac{\pi}{W}(W - c_2),\right)\right)\right]e^{i\omega t}\right\} \tag{15}$$

$$a^- = a_1 - a_2 = \Re\left\{\left[\xi_8\left(\cos\left(\frac{\pi}{W}c_1\right) - \cos\left(\frac{\pi}{W}(W - c_2).\right)\right)\right]e^{i\omega t}\right\} \tag{16}$$

For the experiments carried out in this study, $c_1 = c_2 = 10$mm. By forming a^+ and a^- and making a

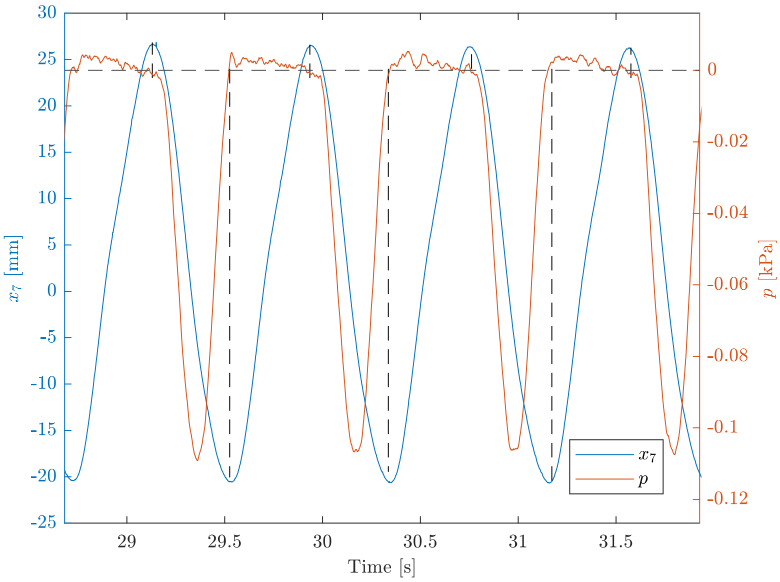

Figure 6: An example of the up-stoke venting configuration showing the pressure measurement together with the mean internal surface elevation. The vertical dashed lines indicate the peaks and troughs of the surface elevation.

harmonic fit to each of the signals, we can extract the piston mode response, ξ_7,

$$\Re\{\xi_7\} = \frac{a_{\mathrm{C}}^{+}}{2}, \qquad \Im\{\xi_7\} = -\frac{a_{\mathrm{S}}^{+}}{2}, \tag{17}$$

$$\Re\{\xi_8\} = \frac{a_{\mathrm{C}}^{-}}{2\cos(\pi/Wc_1)}, \qquad \Im\{\xi_8\} = -\frac{a_{\mathrm{S}}^{-}}{2\cos(\pi/Wc_1)}, \tag{18}$$

and the sloshing mode response, ξ_8, from the first-harmonic amplitudes, where the subscripts C and S indicate the cosine and sine amplitudes of a harmonic fit of the signals using a method of least squares fitting [31]. In fluid dynamics, liquid sloshing refers to the movement of a liquid with a free surface inside a container.

The piston mode response of the chamber was used to derive the air volume flux passing through the orifice plate. The air volume flux, together with the measured pressure drop across the orifice plate, was used to derive the absorbed power of the OWC chamber. The air volume flux is defined as

$$Q(t) = \frac{1}{2}\frac{\mathrm{d}a^{+}}{\mathrm{d}t}A_{\mathrm{c}} \tag{19}$$

where A_c is the internal free surface of the chamber and the term $1/2\,\mathrm{d}a^{+}/\mathrm{d}t$ is the piston mode velocity. The average absorbed power of the chamber is then given by

$$\overline{W} = \frac{1}{T}\int_0^T p(t)\,Q(t)\mathrm{d}t \tag{20}$$

and the non-dimensional absorbed power of the chamber (the capture width ratio, CWR) is given by

$$CWR = \frac{\overline{W}}{W_{\max}} \tag{21}$$

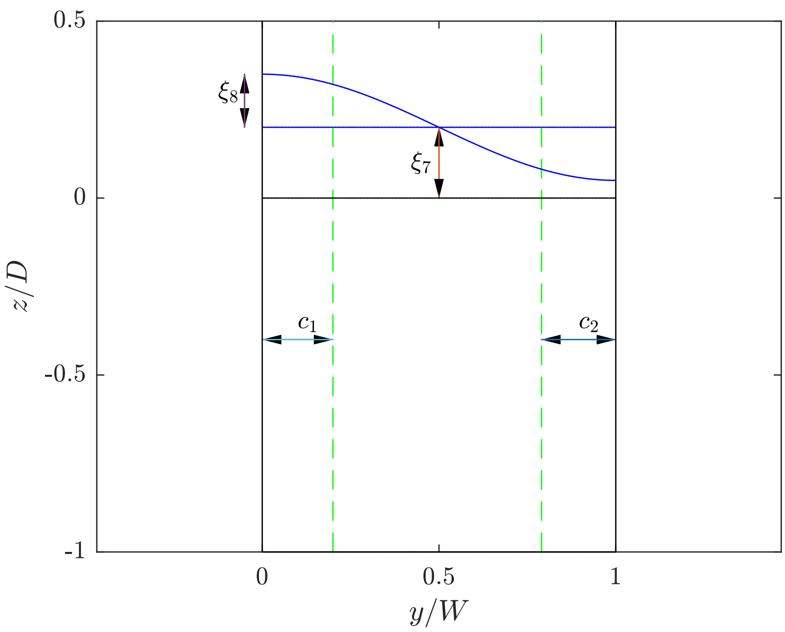

Figure 7: Schematic sketch of the dimensions of the chamber together with the placement of the wave gauges (green dashed lines), the piston mode definition (straight blue line) and the sloshing mode definition (curved blue line).

where $W_{\max}$ is defined as

$$W_{\max} = \frac{1}{2}\rho g A^2 c_{\mathrm{g}} L_{\mathrm{c}} \tag{22}$$

where ρ is the water density, g is the gravitational acceleration, A is the wave amplitude, $L_{\mathrm{c}} = 7.5$m (full-scale) is the length of the chamber in the propagation direction of the waves and c_{g} is the group velocity of the wave defined in Eq. (5). Since we are modelling a double-chamber section of the full attenuator model here, with one tank wall acting as a symmetry plane, we present the CWR for the double-chamber in the results below.

3.1.1. Harmonic analysis of periodic signals

A clean periodic signal is needed to analyze the time series from the experimental measurements from the wave gauges and the pressure sensor. For this, a harmonic analysis of the measured time series is performed using a method of least-squares fitting. This method estimates the analyzed signal as a sum of time-varying sinusoidal functions at frequencies as multiples of the main (fundamental) frequency, ω, plus a mean value.

The harmonic fit for the original measured time-series is given by

$$\eta(t) = \overline{\eta} + \sum_{n=1}^{N} a_n^{\mathrm{C}} \cos(\omega_n t) + a_n^{\mathrm{S}} \sin(\omega_n t), \tag{23}$$

where $\overline{\eta}$ is the mean value of the time series, N is the number of harmonics included in the fit, a_n^{C} is the cosine component of the amplitude of the n^{th} harmonic, a_n^{S} is the sine component of the amplitude of the n^{th} harmonic, and ω_n is the frequency of the n^{th} harmonic. This is a multiple of the main frequency ω, so that

$$\omega_n = \omega\, n. \tag{24}$$

4. Results

For the experimental measurements, the internal free surface elevation was measured using two wave gauges, along with the pressure difference across the orifice in the damped cases, as mentioned in section 3. For demonstration purposes, Fig. 8 shows an example of the surface elevation at each wave gauge and the pressure measurement, in the two-way absorption configuration.

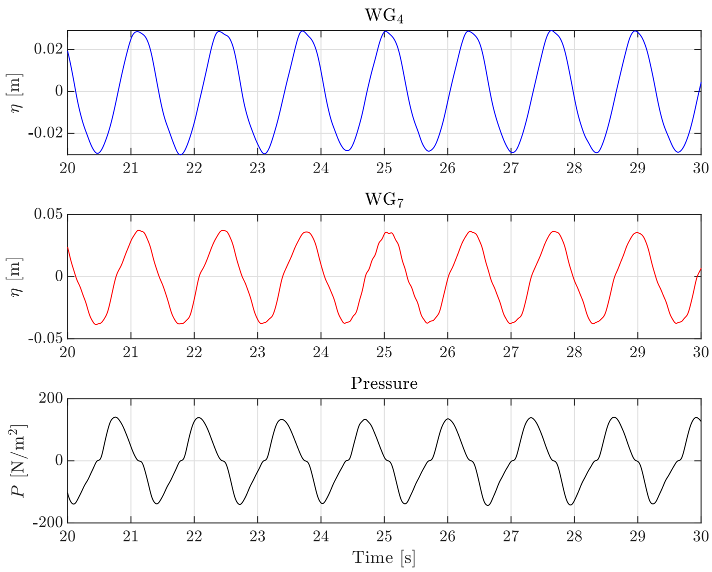

Figure 8: Example of the measured surface elevation, together with the pressure drop across the orifice at wave condition 13 - H=0.062m and T=1.31s. Two-way energy extraction.

In the next Section, we will make several sample comparisons between the measurements and the calculations in the time-domain, and a complete comparison for all cases of the first-harmonic response amplitudes. For the harmonic amplitude comparison, we decompose the signal into harmonics - 1st, 2nd, 3rd, etc. In order to perform the harmonic analysis in the correct way, and obtain a representative output signal, we need to use a clean signal for the input. Fig. 9 shows a demonstration of the full wave signal, together with the extracted portion of the data used for the harmonic analysis. From the two wave gauges it is possible to construct the mean surface elevation inside the OWC chamber - instead of using the terms WG or wave gauge, we use a_1 and a_2 to be consistent with the terminology in Section 3. From the two measurements we form the mean surface elevation as:

$$x_7(t) = \frac{a_1(t) + a_2(t)}{2}. \tag{25}$$

From the mean surface elevation, we can take the time derivative to get the mean surface velocity, and thus compute the air volume flux flowing through the orifice as

$$Q(t) = \frac{\mathrm{d}x_7(t)}{\mathrm{d}t} A_\mathrm{c}. \tag{26}$$

Alternatively, we can compute the air volume flux from the pressure measurement, through the relation in Eq. (8), where the time-varying air volume flux is given by

$$Q(t) = C_\mathrm{d} A_\mathrm{o} \sqrt{\frac{2|p(t)|}{\rho_\mathrm{a}}} \mathrm{sign}(p). \tag{27}$$

A C_d value of 0.64 was found during an earlier experimental campaign using a mechanical air pump [21]. This value also provides the best fit between the two air volume-flux calculations for the majority of the different wave conditions tested here. Fig. 10 shows one typical example of how the two estimates compare. Here, the flux computed from the two wave probes can be seen to contain significant high-frequency oscillation which is not observed by the pressure gauge. As discussed in more detail below, we attribute this to aliasing from higher modes (in both space and time) which cannot be captured by just two wave probes. Therefore, we consider the air-volume flux computed from the pressure to be more reliable, and use this value to compute the absorbed power.

Perhaps unsurprisingly, in the one-way absorption case we observe a significantly more complicated chamber response with an inherently highly nonlinear, non-symmetric shape in time, but also significant higher-mode sloshing response in both the transverse and the longitudinal directions. Fig. 11 shows the same

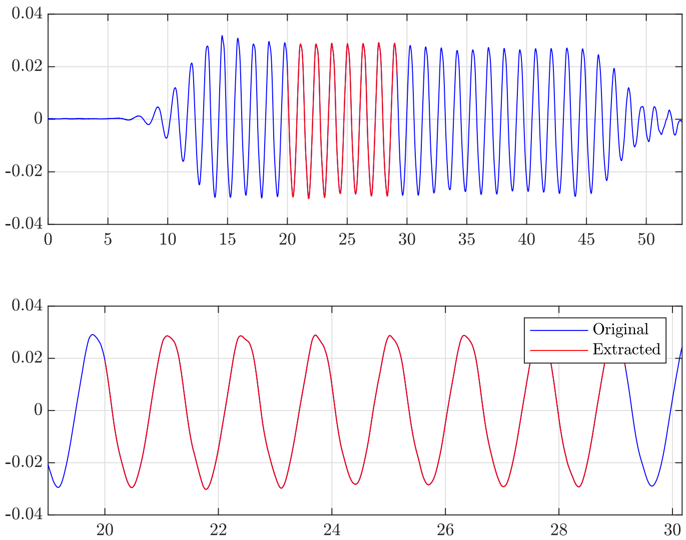

Figure 9: Example showing the portion of the measurement used for the harmonic analysis, wave condition 13 - H=0.062m and T=1.31s. Two-way energy extraction.

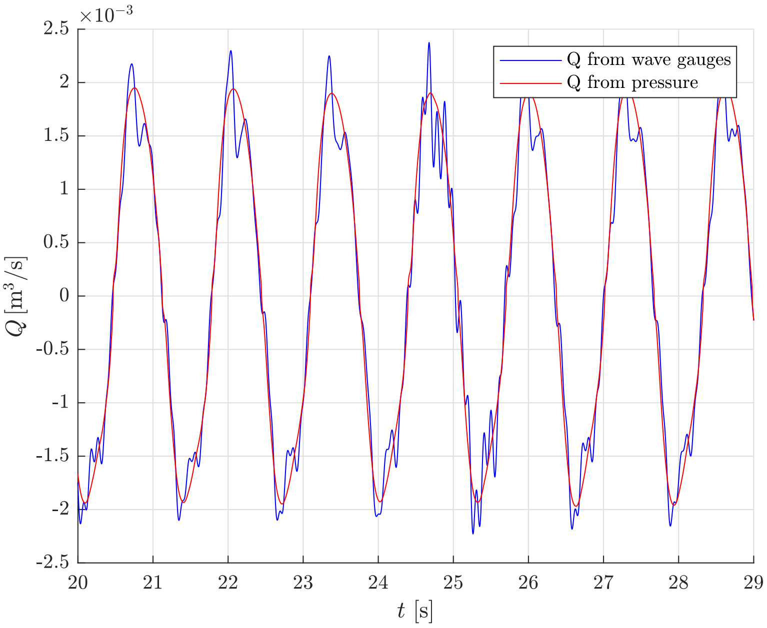

Figure 10: Comparison of the air volume flux computed from the two wave gauges (blue line) and the pressure gauge measurement (red line), wave condition 13 - H=0.062m and T=1.31s. Two-way energy extraction. $C_d = 0.64$

comparison as Fig. 10, but with venting on the upstroke half-cycle of the wave. Here we have used the same C_d as in the two-way extraction. Clearly the air-volume flux computed from the two wave probes (blue line) is significantly larger than the air-volume flux computed from the pressure gauge (red line). Our explanation for this discrepancy is that the presence of many different sloshing modes (in both the longitudinal and the transverse directions) produces an aliasing effect such that the average of the two wave probe elevations is no longer equivalent to the mean free-surface level. It is perhaps intuitively obvious that with only two measurement points, we can at most identify two modal amplitudes, but a synthetic example demonstrating quantitatively how the mean value is corrupted by the higher modes is given in Appendix A as an illustration. Clearly in the one-way absorption case, it is even more important to rely on the pressure measurement for the air-volume flux estimate. Given the complexity of the response in this case, we would need to use many more wave probes to accurately estimate the mean surface motion, but this will require a larger-scale model or smaller wave probes. Also notable in Fig. 11 is a significant flux through the orifice during the up-stroke cycle, illustrating the imperfect sealing of the venting valve.

4.1. Comparison with numerical calculations

In this Section, we compare the experimental measurements with numerical calculations carried out in both the frequency domain and the time domain. Air compressibility effects are generally quite significant at full-scale for OWC chambers however, since the experiments are performed at such a small scale (the chamber air volume is $0.002\,\mathrm{m}^3$), air compressibility effects are assumed to be negligible and we have therefore modelled the air as incompressible. Frequency domain calculations are performed as described in Section 2.1 and Section 2.3. The calculations in the time domain are performed as described in Section 2.2 and Section 2.3. In order to model the relatively small width of the experimental tank, two image bodies are included along with the full double-chamber model as shown in Fig. 12. The centerline positions of the images are located at $y = \pm 0.65$m at model scale, *i.e.* the tank width. The geometry is a high-order representation generated using

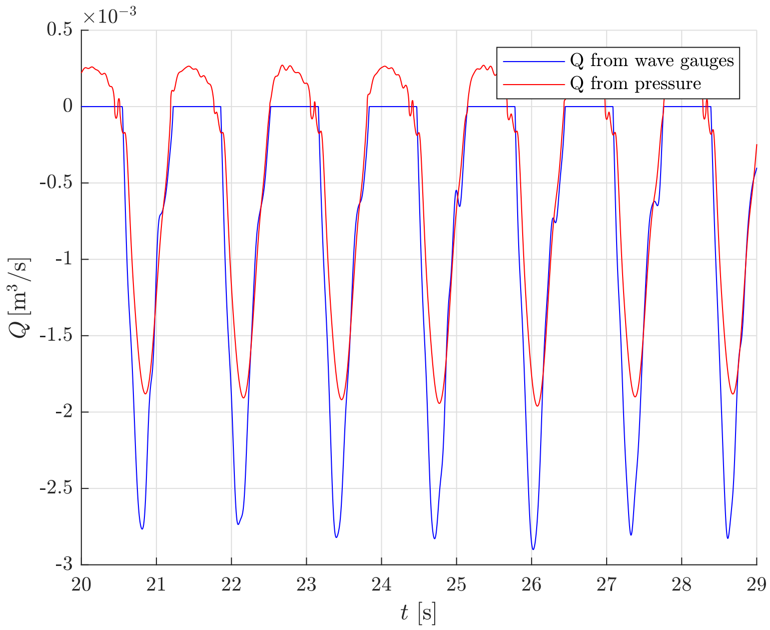

Figure 11: Comparison of the air volume flux computed from the two wave gauges (blue line) and the pressure gauge measurement (red line), wave condition 13 - H=0.062m and T=1.31s. Upstroke venting of the OWC chamber. $C_d = 0.64$

the *MultiSurf* software which is used as an input by WAMIT. Only the submerged portion of the chamber is discretized, and the light green patches represent the free surface of the internal chamber where the generalized modes are applied. For the radiation problem, the internal free surfaces of all the internal chambers move together with that of the actual chamber. In order to accurately compute the infinite-frequency added resistance, the method described by [25] is applied, which is critical to getting accurate results in the time-domain. The time-domain results are computed using the open source package DTUMotionSimulator [32]. To compare response amplitudes, we perform a harmonic analysis of each time series as described in Section 3.1.1.

4.1.1. Two-way energy capture

We start with the two-way damping results then move to the novel one-way damping results to compare the differences between the two.

We first compare the experimental measurements with the numerical calculations in the time-domain, i.e. we extract a portion of the time-series for a particular wave condition and compare. Fig. 13a shows the internal surface elevation measured at wave gauge 4, the internal surface elevation measured at wave gauge 7 and the pressure difference across the orifice for wave condition 5 - H=0.026m and T=0.81s. Due to the extreme fluctuations in the pressure signal, this has been filtered to give a better comparison. We here used a finite impulse response (FIR) smoothing filter based on polynomial order and frame length, i.e. how many points to include for the smoothing.

Fig. 13a shows that the numerical calculations overestimate the experimentally measured internal free surface elevation, both at wave gauge 4 and wave gauge 7. However, the numerical results for the pressure difference across the orifice are lower than the experiment results. Fig. 13b shows a comparison of the same parameters as Fig. 13a, but this time for wave condition 13. The figure shows the same trend as in Fig. 13a, although the surface elevation at wave gauge 7 for experiments and numerical results gives a good match.

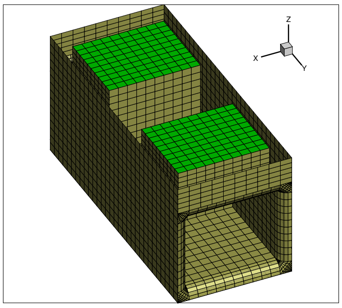

(a) The high-order panel discretization of the chamber.

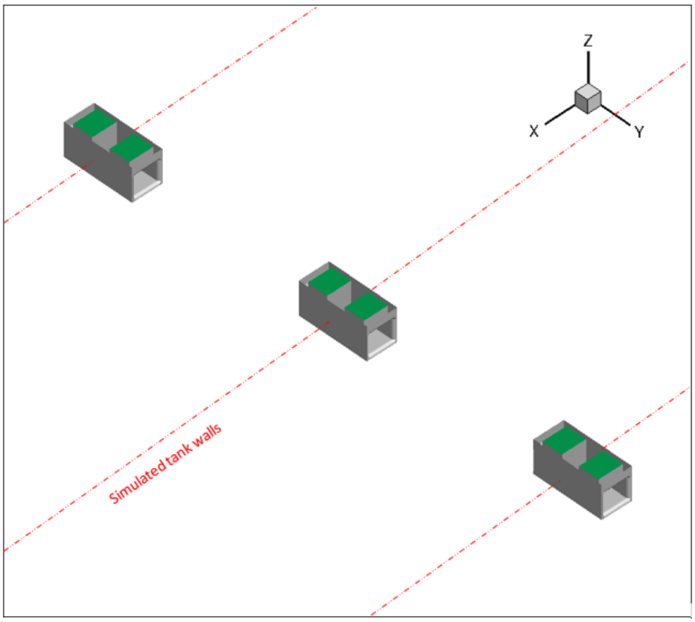

(b) The complete geometry with two images to approximate the effects of the tank walls.

Figure 12: The geometry for the WAMIT calculations.

As the measured pressure is the only physical parameter used to compute the power, we compare experimental and numerical predictions of the first harmonic decomposition of the pressure drop across the orifice. Fig. 14 shows the results as a function of the wave period. Here the error bars on the experimental points represent only the uncertainty associated with the three realizations that were performed for each condition. A more detailed uncertainty analysis which includes all of the experimental errors is a goal of future work but has not yet been carried out. There is generally good agreement between the experiments and numerical results, however around the resonance period there are some significant deviations.

The main objective of this study is to investigate the power absorption of the OWC chamber. This is shown in Fig. 15, where the experimentally computed non-dimensional absorbed power is plotted against the numerical results for the two-way energy capture. Since we are modelling a double-chamber section of the full attenuator device, with one tank wall acting as a plane of symmetry, we show here results for the double-chamber section normalized by its length in the x-direction, $L_c = 7.5$m at full-scale. Fig. 15 shows that there is relatively good agreement between experimental and numerical results, though the numerical results tend to overestimate the absorbed power. These results are also in good agreement with earlier experimental measurements and calculations. It should be noted that the Capture Width Ratio results are those associated with a double chamber section, as shown in Fig. 12a.

4.1.2. One-way energy capture - upstroke venting

We will now focus on the one-way energy capture results. In the upstroke venting configuration, the positive cycle of the wave enables the chamber to vent, such that the pressure drop across the orifice is close to zero throughout the entire positive half-cycle. Fig. 16a shows the same quantities as Fig. 13a for the upstroke venting configuration. It is clear from the pressure time-series that the pressure is nearly zero when the chamber vents on the upstroke half-cycle of the wave period. For the frequency domain results, there is no actual venting since the model is by definition time-harmonic. However, the same power should be extracted over one cycle via the modified equivalent damping coefficient. In the time-domain model,

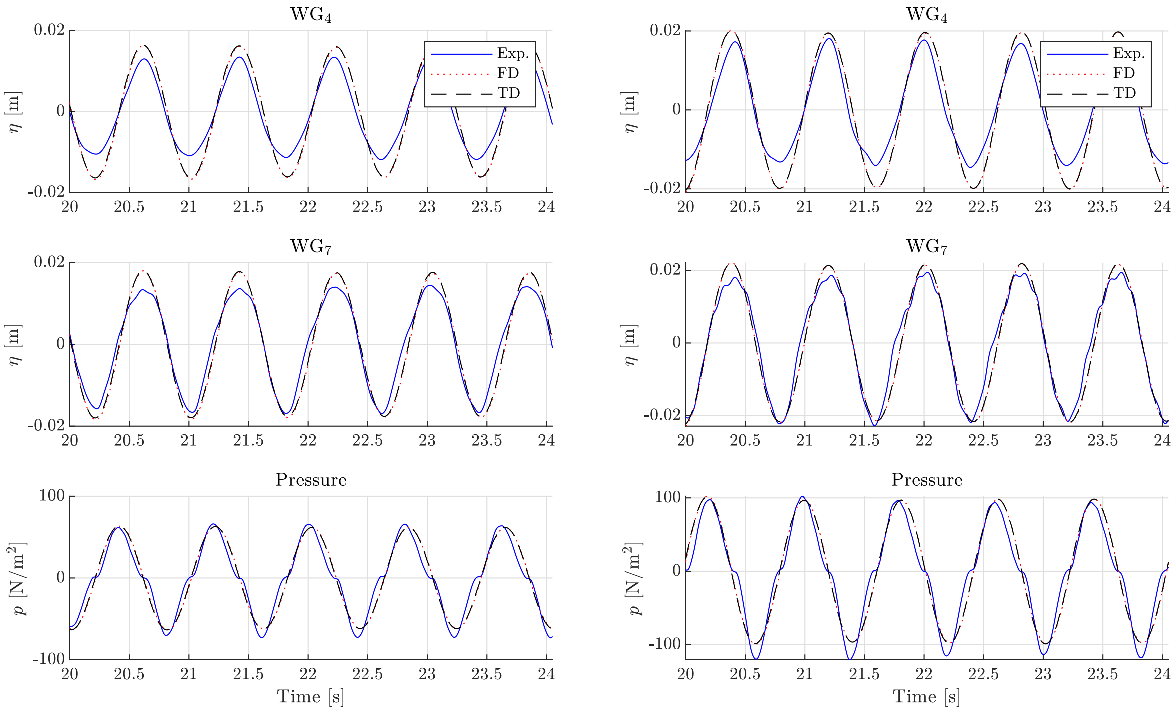

(a) Wave conditions: H=0.026m and T=0.81s.

(b) Wave conditions: H=0.041m and T=0.81s.

Figure 13: Chamber motions and pressure in the two-way configuration for two cases near resonance. Blue solid line - experiments, red dotted line - frequency domain calculations, black dashed line - time domain calculations.

the applied pressure is set to zero on the upstroke, as for the experiment. Similarly for the wave elevation signals, the frequency-domain results are by definition harmonic with a single amplitude (zero-mean), while the measurements clearly show a high peak and a relatively low trough which is also captured by the time-domain model.

For the internal free surface elevation (at both wave gauge 4 and 7) the total peak-to-trough height is fairly well predicted by the calculations, but the experimental measurements are generally a bit larger and contain more harmonic components. However, for the pressure drop, the height is strongly over-estimated by the calculations and there is a slight delay in the closing point of the passive valve which presumably is caused by the inertia of the flap. This seems to cause a shift in the peak value of the pressure, and may also contribute to reducing it.

Fig. 16b shows the same quantities as Fig. 16a for the steeper wave condition 13 and similar general conclusions can be drawn. Somewhat more nonlinearity can be seen here in the elevation signals as well as stronger evidence of the one-way valve's inertia. Fig. 17 shows the capture width ratio for all conditions and compares the measurements with the calculations. Clearly the measured values are substantially lower than predictied by the calculations. As indicated above, we attribute this mainly to the imperfect venting valve mechanism which leads to a delay in the build-up of pressure and a substantially lower peak applied pressure, but this needs to be confirmed by future experiments or refined CFD calculations.

4.1.3. One-way energy capture - downstroke venting

Here we turn our attention to the other configuration of the one-way energy capture of the OWC chamber, namely the downstroke venting of the chamber. This configuration is the opposite of the previous, i.e. the negative half-cycle of the wave enables the chamber to vent the air, giving a nearly zero applied pressure

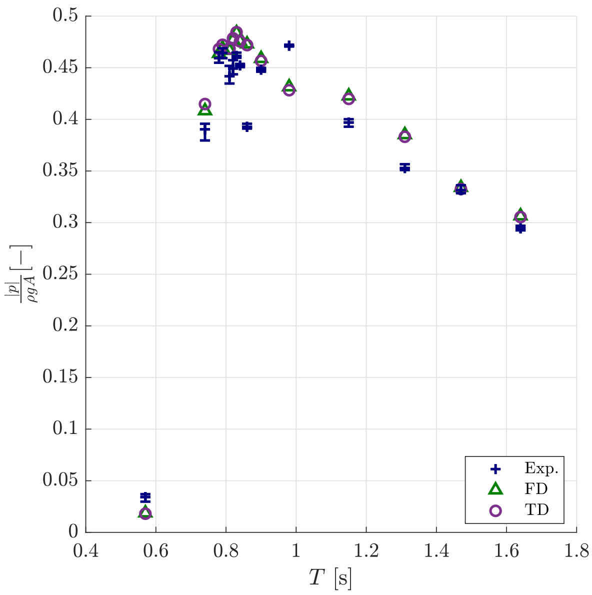

(a) Wave steepness $H/L = 0.025$.

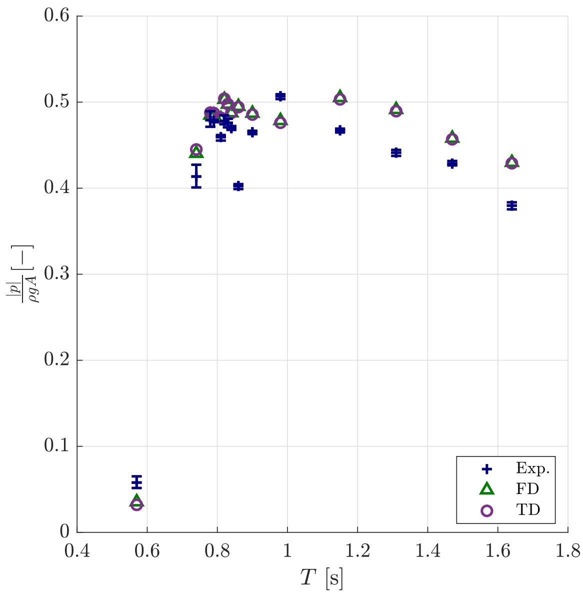

(b) Wave steepness $H/L = 0.04$.

Figure 14: Nondimensional pressure drop across the orifice, two-way energy extraction. Blue crosses are experimental measurements; green triangles are the frequency-domain calculations; purple circles are the time-domain calculations.

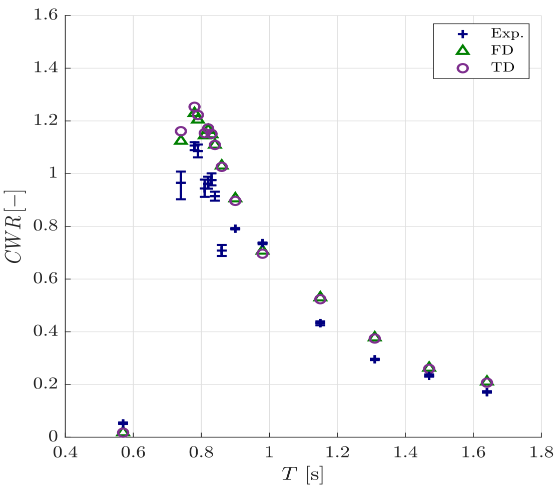

(a) Capture-width-ratio, $H/L = 0.025$

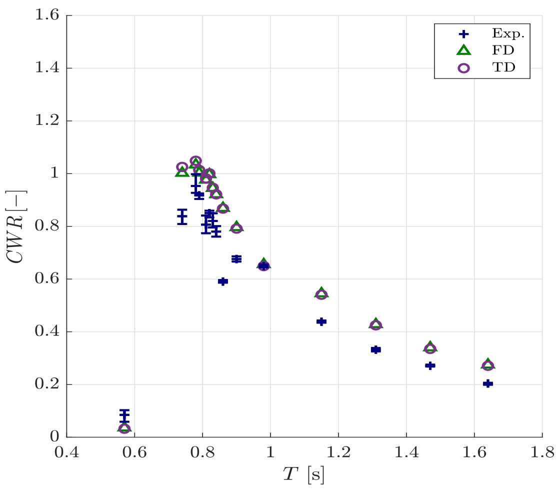

(b) Capture-width-ratio, $H/L = 0.04$

Figure 15: CWR with respect to $L_c = 7.5$m (full-scale) of the double-chamber in the two-way configuration. Blue crosses are experimental measurements; green triangles are the frequency domain calculations; purple circles are the time-domain calculations.

on the entire negative half-cycle. Here we will similarly present all the results, in the same manner as in the previous subsections. Fig. 18 shows the time-series comparison of the experimental measurements and the numerical calculations for the downstroke venting configuration. The figure shows time-series results for wave conditions 5 and 13, respectively. As in Fig. 16 the experimental measurements for the surface elevation

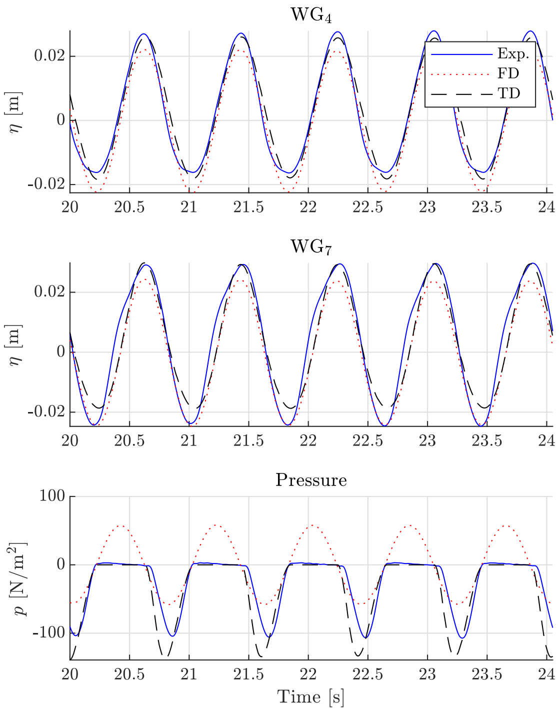

(a) Wave conditions: H=0.026m and T=0.81s.

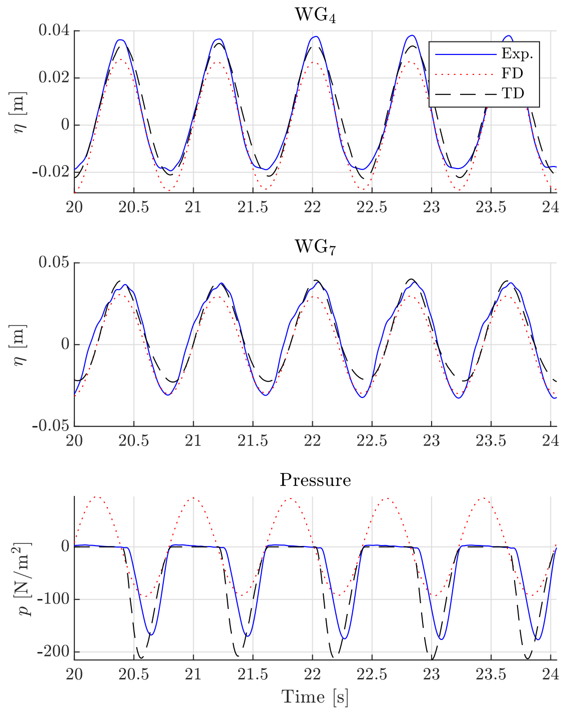

(b) Wave conditions: H=0.041m and T=0.81s.

Figure 16: Chamber motions and pressure in the upstroke-venting configuration for two cases near resonance. Blue solid line - experiments, red dotted line - frequency domain calculations, black dashed line - time domain calculations.

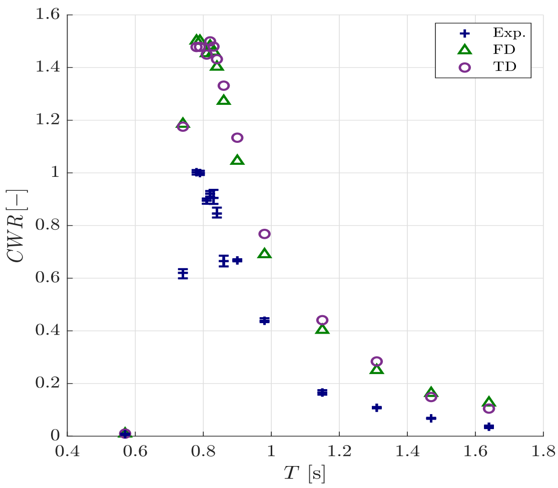

(a) Wave steepness $H/L = 0.025$

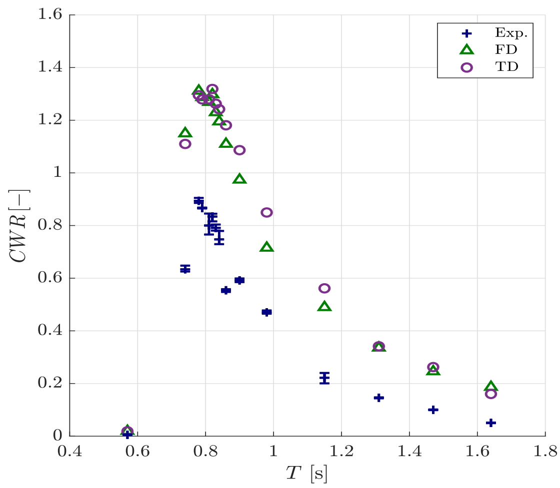

(b) Wave steepness $H/L = 0.04$

Figure 17: CWR with respect to $L_c = 7.5$m (full-scale) of the double-chamber in the up-stroke venting configuration.

are generally larger than the numerical results, and the experimentally-measured pressure difference across the orifice is substantially smaller than the numerical results. As in the up-stroke venting case, a significant delay in the closing of the vent is evident.

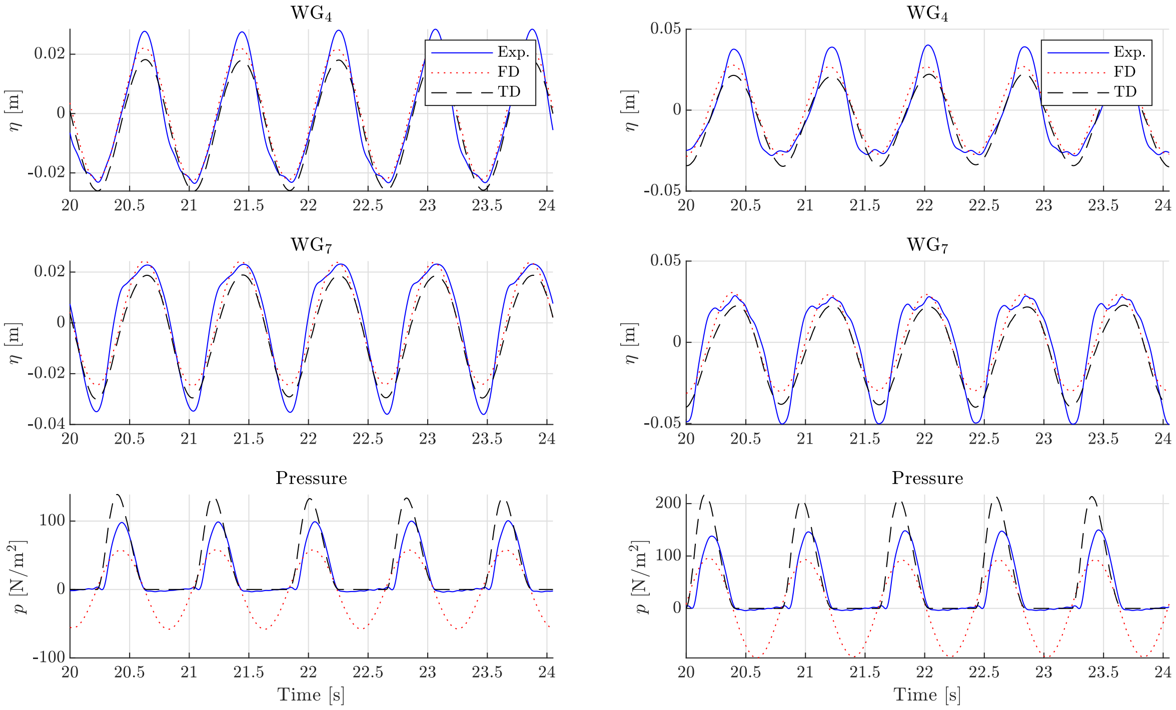

(a) Wave conditions: H=0.026m and T=0.81s. (b) Wave conditions: H=0.041m and T=0.81s.

Figure 18: Chamber elevation and pressure time series near resonance in the down-stroke venting condition. Blue solid line - experiments, red dotted line - frequency domain calculations, black dashed line - time domain calculations.

Fig. 19 compares the measured and computed capture width ratio for all wave conditions. As in the up-stroke venting condition, the measured values are substantially lower than predicted by the calculations.

4.2. Optimizing the orifice diameter

The orifice diameter chosen for this study was based on a simple optimization strategy using the weakly-nonlinear frequency domain model with two-way absorption. Here we choose a range of (model-scale) orifice diameters, from 0.01 m to 0.03 m in steps of 0.002 m and compute the integral of the CWR over non-dimensional frequency. These results are shown in Fig. 20 for the two wave steepness values of 0.025 and 0.04 using two-way absorption. To indicate the sensitivity of these results to the head-loss coefficient C_d, each plot shows three values which bound the most likely value of $C_d = 0.64$ within realistic limits.

The curves here for $C_d = 0.64$ suggest that a diameter of 0.016m is close to the optimal orifice diameter.

To consider how this choice performs for the other configurations, we have also made similar calculations using the time-domain model for two-way, up-stroke and down-stroke venting. Fig. 21 shows results for the integrated capture width ratio ($\overline{CWR}$) as a function of the orifice diameter. Fig. 21a shows results for the 2.5% wave steepness and Fig. 21b shows results for the 4% wave steepness. Frequency-domain results for 1-way absorption are also shown for completeness, but due to the highly-nonlinear nature of the one-way configuration we consider the time-domain calculations to be more realistic. From these curves we can see that the time-domain model suggests a slightly larger optimal orifice diameter of 0.018 to 0.02m.

As a final comment however, we note that a true optimization of the turbine should not necessarily be based on the integrated CWR. Instead, the estimated yearly distribution of wave conditions at a particular

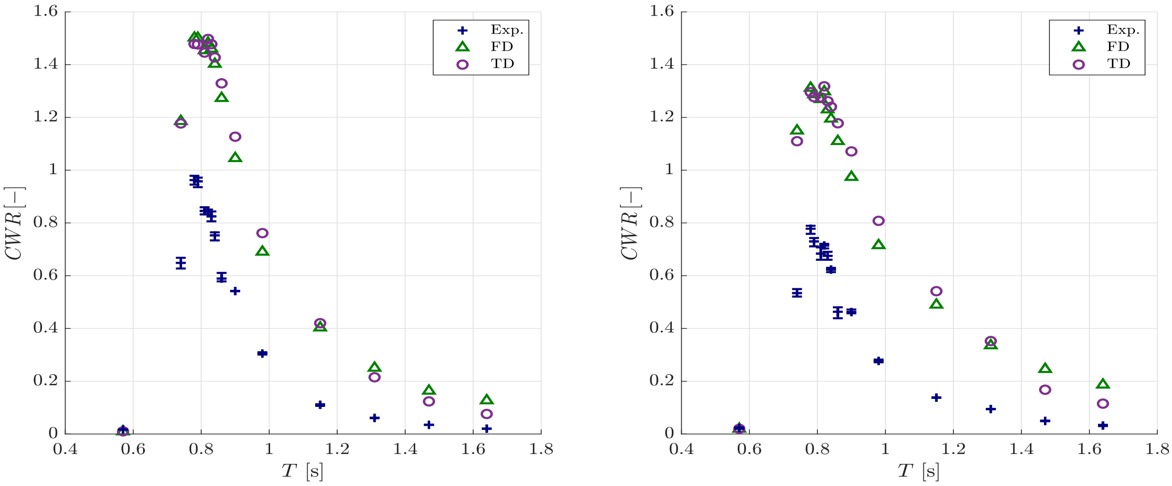

(a) Wave steepness $H/L = 0.025$

(b) Wave steepness $H/L = 0.04$

Figure 19: CWR with respect to $L_c = 7.5$m (full-scale) of the double-chamber in the downstroke venting configuration.

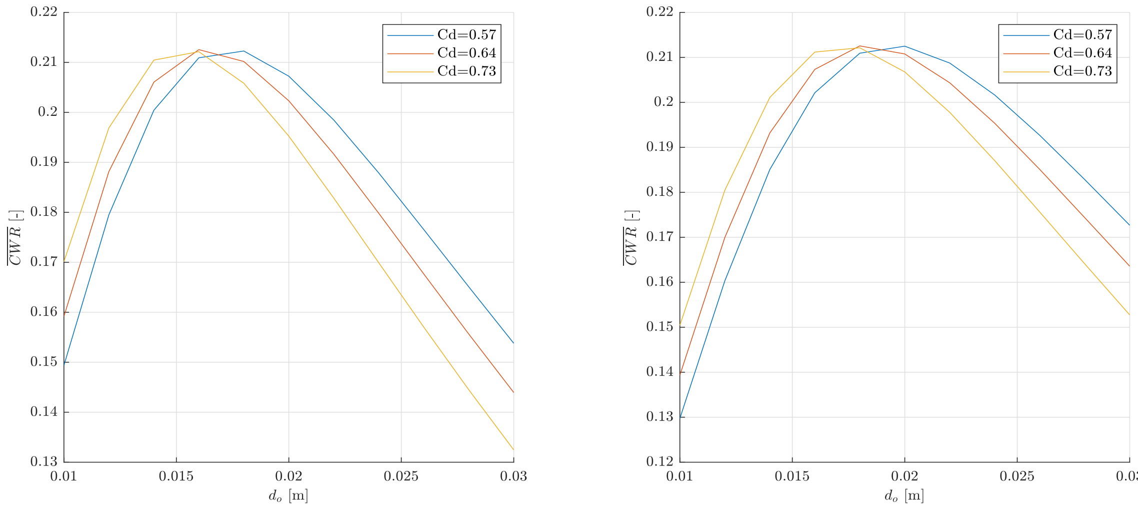

(a) Integrated CWR as a function of the orifice diameter at wave steepness $H/L = 0.025$

(b) Integrated CWR as a function of the orifice diameter at wave steepness $H/L = 0.04$

Figure 20: Integrated capture width ratio (CWR) as function of orifice diameter - frequency domain calculations, two-way absorption.

deployment site should be collected. Then, the orifice diameter that maximizes the yearly energy capture should be found, which can then be used to design the optimal turbine.

5. Discussion

For two-way energy absorption, good agreement is found between experimental measurements and calculations based on weakly-nonlinear potential flow theory. In practice, this hydrodynamic power must be

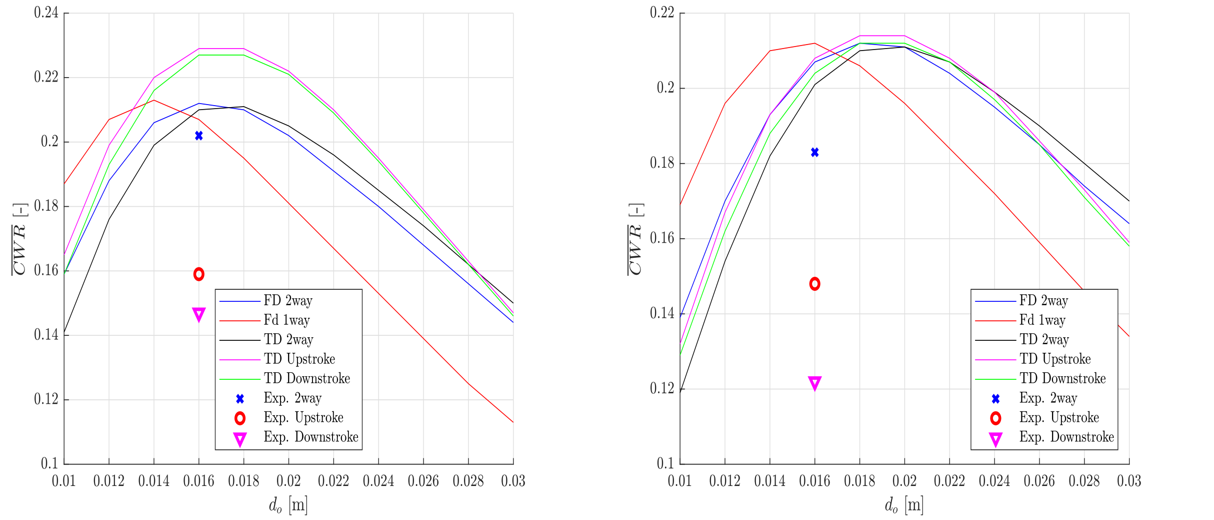

(a) Integrated CWR as a function of the orifice diameter at wave steepness $H/L = 0.025$, $C_d = 0.64$

(b) Integrated CWR as a function of the orifice diameter at wave steepness $H/L = 0.04$, $C_d = 0.64$

Figure 21: Integrated capture width ratio (CWR) as a function of the orifice diameter - frequency domain calculations, time-domain calculations and experiments for all configurations.

extracted by a self-rectifying air turbine which generally has lower peak and mean efficiencies than a uni-directional turbine. This motivates a one-way power extraction strategy where a passive valve system vents the chamber to the atmosphere on half of the cycle. The assumption here is that by allowing potential energy to freely enter the chamber during the passive cycle, roughly the same total energy will then be available for extraction on the active half-cycle. The numerical calculations (with a perfect vent system) confirm the idea, and predict as much as 30% more absorbed power near resonance and about 30% less in long-waves (see Fig. 22). The experiments also confirm the idea, but show slightly less energy absorption near the peak and substantially less in long waves. Up- and downstroke venting are nearly the same near resonance but down-stroke venting shows substantially less power absorption in long waves. The time-domain calculations actually show the same trend, though to a lesser extent. The relatively large discrepancies in magnitude between measurements and calculations here are mostly attributed to losses associated with the passive valve system.

It is challenging to construct a passive venting valve in general, but especially at such a small scale where the pressures are so low. A significant delay in the closing of the valve is clear from the pressure signal, along with significant air flux through the orifice on the passive cycle, indicating that there are significant energy losses associated with the valve. The one-way venting valve constructed in this study was clearly not optimal, and better performance can certainly be achieved, as is apparently the case for the UniWave design mentioned above. Even so, some losses can be expected in general. In [33] for example, they assume losses of 5% on the passive cycle, which is probably realistic. So while a vented design may allow for significant gains in turbine efficiency, passive losses must also be evaluated, along with the additional mechanical complexity of a one-way valve system. One-way energy capture also leads to highly nonlinear motion of the internal chamber surface, which adds to the complexity of the numerical analysis. Higher internal elevations on the up-stroke also increase the danger of impact with the chamber roof and possible water ingress into the turbine. Thus, any practical evaluation of one-way vs. two-way energy absorption must include consideration of a range of interacting factors which all influence the final energy capture.

Our weakly-nonlinear time-domain calculations capture the trends shown by the experiments, where more

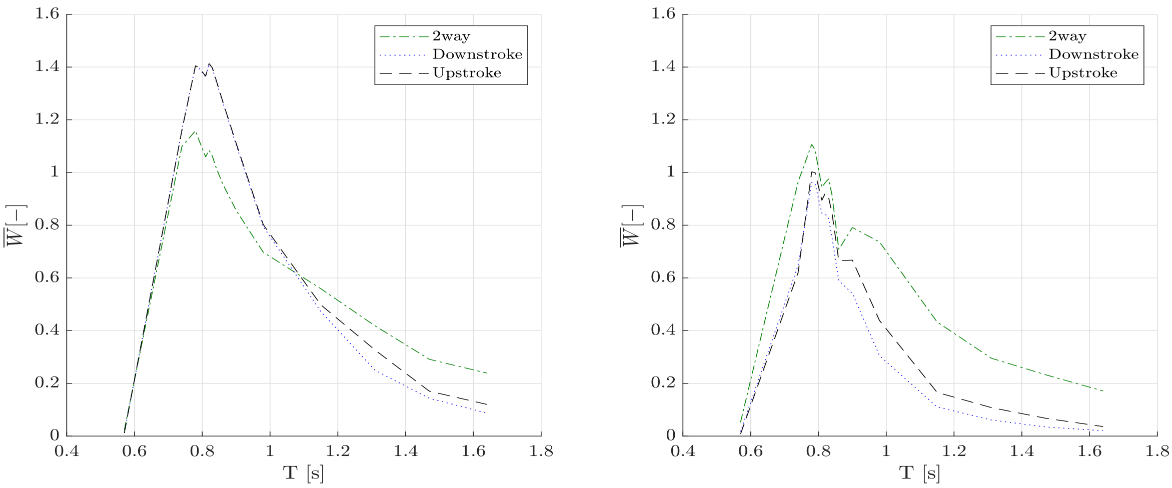

(a) Time-domain numerical calculations for $H/L = 0.025$

(b) Experimental measurements for $H/L = 0.025$

Figure 22: CWR with respect to $L_c = 7.5$m (full-scale) of the double-chamber for the three different configurations, $H/L = 0.025$.

energy is absorbed in long-waves by venting on the up-stroke than on the down-stroke, though the effect is less pronounced. This suggests that the effect is not associated with the passive valve system, which works equally well (or badly) in both directions. Instead, this is attributed to the highly nonlinear physics of the internal chamber motion which apparently allows more potential energy to be stored by the free upward motion than by the free downward motion. Although we are not aware of other published results in the literature that support or explain this result, we note that the UniWave concept reported in [16] vents on the up-stroke.

More refined numerical calculations using CFD for example, and/or larger-scale experimental measurements are required to better understand the more complicated physics of the one-way configuration. From a more practical perspective, choosing which strategy is advantageous is a balance between several design factors.

6. Conclusions

In this study we have investigated the hydrodynamic performance of a fixed OWC chamber using both conventional two-way energy absorption and a one-way absorption strategy where the internal chamber motion is un-damped on either the up- or the down-stroke. Chamber motion response and pressure are measured, from which we compute the absorbed hydrodynamic power. Measured quantities are compared to predictions using weakly-nonlinear potential flow theory in both the frequency- and the time-domain. The choice of orifice diameter used to model the turbine is motivated by a simple optimization of the integrated CWR using the frequency-domain model.

For the conventional two-way absorption strategy, good agreement is found between the calculations and the measurements. For the one-way strategies, the experimental trends are captured by the time-domain model but total power absorption is dramatically over predicted. This is mostly attributed to losses from the experimental passive valve system, but this contention needs to be confirmed by new experiments using a better venting valve system, which could be either passive or active.

One-way absorption allows for the use of a uni-directional air turbine, but at the expense of additional mechanical complexity and the associated valve-system losses. It also results in larger and much more non-linear motions of the internal chamber, which may have additional negative consequences. The presented measurements and calculations highlight the need for more refined calculations and larger-scale measurements in order to better understand the associated physics and ultimately determine which strategy is more attractive.

CRediT author contribution statement

Bárður Joensen: Methodology, Validation, Formal analysis, Investigation, Data curation, Writing – original draft, Writing – review & editing, Funding acquisition. **Harry B. Bingham:** Numerical model setup, Writing - original draft, Writing - review & editing, Supervision, Project administration. **Robert W. Read:** Writing - review & editing, Supervision. **Kim Nielsen:** Writing - review & editing, Supervision. **Jokin Brito Trevino:** Methodology, Validation, Investigation, Data curation.

Declaration of competing interests

The authors declare that they have no known competing financial interests or personal relationships that could have appeared to influence the work reported in this paper.

Acknowledgements

This study is based on project supported by the Research Council of the Faroe Islands, grant number 02010. The same project is also financially supported by Betri Research Foundation, SEV, Bakkafrost Farming, MOWI Faroes and Hiddenfjord.

Appendix A. Demonstration of amplification of mean surface elevation

We sum up a total of 6 different wave components together with a mean amplitude level. The wave components are:

$$\begin{aligned}
\eta_1(t) &= A_7 \cos(-\omega t)\\
\eta_2(t) &= A_8 \cos(k_{nat} x) \cos(-\omega t)\\
\eta_3(t) &= A_{res} \cos(-\omega_{res} t)\\
\eta_4(t) &= A_{slosh} \cos(k_{nat} x) \cos(-\omega_{nat} t)\\
\eta_5(t) &= A_9 \cos(k_9 x) \cos(-\omega t)\\
\eta_6(t) &= A_9 \cos(k_9 x) \cos(-\omega_9 t)
\end{aligned} \tag{A.1}$$

By predefining the amplitudes to reasonable values, summing these up, together with the wave number being associated with either a first transverse sloshing mode or second transverse sloshing mode.

$$\eta_{sum}(t) = \eta_1(t) + \eta_2(t) + \eta_3(t) + \eta_4(t) + \eta_5(t) + \eta_6(t) + A_{mean} \tag{A.2}$$

By computing the error in the mean, piston mode amplitude at the wave frequency and the piston mode amplitude at the resonance frequency, by inclusion and exclusion of the A_9 amplitude, respectively, it was found that by including this second transverse sloshing wave a significant error is found. This means that, unfortunately, with higher order modes present in the free surface elevation inside the chamber, these contribute to an amplification of the mean elevation of the internal chamber elevation.
For demonstration purposes, we will here show an example of the assumption. In order to successfully demonstrate this, we will exaggerate some of the values for clarification purposes, i.e. the wave parameters are scaled up to full scale.

$$\begin{aligned}
A_{mean} &= 5.0\\
A_7 &= 7.5\\
A_8 &= 1.25\\
A_9 &= 0.5\\
A_{res} &= 2.5\\
A_{slosh} &= 0.625\\
\omega &= 0.7727\\
\omega_{res} &= 1.0836\\
\omega_{nat} &= 2.4827\\
\omega_9 &= 3.5111\\
k_{nat} &= 0.6283\\
k_9 &= 1.2566
\end{aligned} \tag{A.3}$$

By using these values we get the results in Fig. A.23 The figure clearly shows, that by including the second order transverse standing modes in the summation of wave components, the decomposition of the harmonics show a difference in mean amplitudes.

Abbreviations

The following list of abbreviations is used in this manuscript:

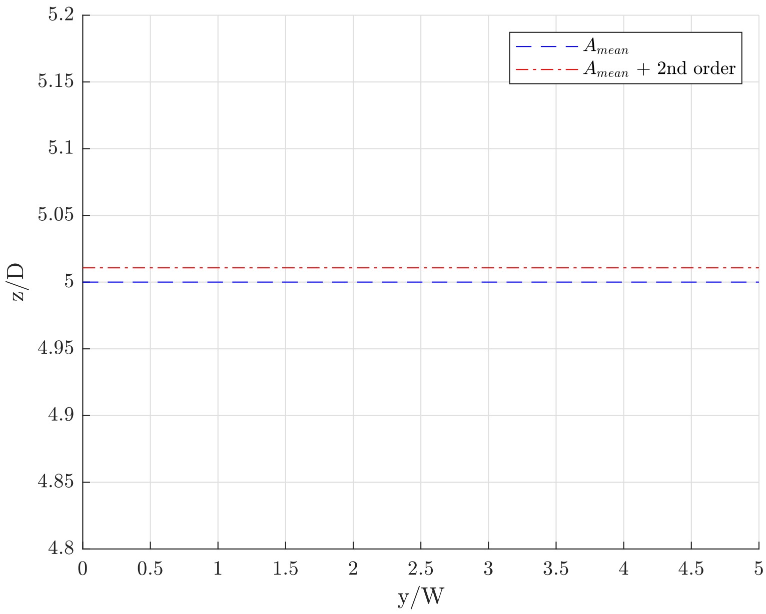

Figure A.23: Demonstration of the significance of including second order transverse standing modes. Blue dashed line - mean amplitude, red dash-dotted line - mean amplitude including the second order modes.

OWC Oscillating water column

WEC Wave energy converter

RANS Reynolds-Averaged Navier-Stokes

VOF Volume-of-fluid

PTO Power-take-off

CFD Computational fluid dynamics

U-OWC U-shaped oscillating water column

PIV Particle image velocimetry

CWR Capture width ratio

FD Frequency domain

TD Time domain

FFT Fast-Fourier Transform

References

[1] A. F. O. Falcão, J. C. C. Henriques, Oscillating-water-column wave energy converters and air turbines: A review, Renewable Energy 85 (2016) 1391–1424. doi:10.1016/j.renene.2015.07.086.

[2] L. M. C. Gato, V. Warfield, A. Thakker, Performance of a high-solidity wells turbine for an OWC wave power plant, Journal of Energy Resources Technology 118 (4) (1996) 263–268. doi:10.1115/1.2793872.

[3] Y. Torre-Enciso, I. Ortubia, L. de Aguileta, J. Marqués, Mutriku wave power plant: from the thinking out to the reality, in: Proceedings of the 8th European Wave and Tidal Energy Conference, Uppsala, Sweden, 2009.

[4] A. F. O. Falcão, The shoreline owc wave power plant at the Azores, in: Proceedings of the 4th European Wave Energy Conference, Aalborg, Denmark, 2000.

[5] The Queen's University of Belfast, Islay Limpet wave power plant-publishable report, Tech. rep., The Queen's University of Belfast (2002).

[6] T. V. Heath, A review of oscillating water columns, Philosophical Transactions of the Royal Society A: Mathematical, Physical and Engineering Sciences 370 (1959) (2012) 235–245. doi:10.1098/rsta.2011.0164.

[7] N. Delmonte, D. Barater, F. Giuliani, P. Cova, G. Buticchi, Review of oscillating water column converters, IEEE Transactions on Industry Applications (2015) 1–1doi:10.1109/tia.2015.2490629.

[8] M. Shalby, D. G. Dorrell, P. Walker, Multi-chamber oscillating water column wave energy converters and air turbines: A review, International Journal of Energy Research 43 (2) (2018) 681–696. doi:10.1002/er.4222.

[9] A. F. O. Falcão, Overview on oscillating water column devices, in: Floating Offshore Energy Devices, Materials Research Forum LLC, 2022. doi:10.21741/9781644901731-1.

[10] D. Howe, J.-R. Nader, OWC WEC integrated within a breakwater versus isolated: Experimental and numerical theoretical study, International Journal of Marine Energy 20 (2017) 165–182. doi:10.1016/j.ijome.2017.07.008.

[11] C. Perez-Collazo, D. Greaves, G. Iglesias, Hydrodynamic response of the WEC sub-system of a novel hybrid wind-wave energy converter, Energy Conversion and Management 171 (2018) 307–325. doi:10.1016/j.enconman.2018.05.090.

[12] C. Perez-Collazo, R. Pemberton, D. Greaves, G. Iglesias, Monopile-mounted wave energy converter for a hybrid wind-wave system, Energy Conversion and Management 199 (2019) 111971. doi:10.1016/j.enconman.2019.111971.

[13] A. F. O. Falcão, J. C. C. Henriques, L. M. C. Gato, Self-rectifying air turbines for wave energy conversion: A comparative analysis, Renewable and Sustainable Energy Reviews 91 (2018) 1231–1241. doi:10.1016/j.rser.2018.04.019.

[14] B. S. Lopes, L. M. C. Gato, A. F. O. Falcão, J. C. C. Henriques, Test results of a novel twin-rotor radial inflow self-rectifying air turbine for OWC wave energy converters, Energy 170 (2019) 869–879. doi:10.1016/j.energy.2018.12.078.

[15] P. Benreguig, M. Vicente, A. Dunne, J. Murphy, Modelling approaches of a closed-circuit OWC wave energy converter, Journal of Marine Science and Engineering 7 (2) (2019) 23. doi:10.3390/jmse7020023.

[16] A. Fleming, G. MacFarlane, S. Hunter, T. Denniss, Power performance prediction for a vented oscillating water column wave energy converter with a unidirectional air turbine power take-off, in: Proceedings of the 12th European Wave and Tidal Energy Conference.

[17] N. Ansarifard, S. Kianejad, A. Fleming, S. Chai, A radial inflow air turbine design for a vented oscillating water column, Energy 166 (2019) 380–391. doi:10.1016/j.energy.2018.10.068.

[18] Wave Swell Energy, https://www.waveswell.com/ ([accessed 23.03.2021]).

[19] K. Nielsen, H. Bingham, MARINET experiment KNSWING testing an I-Beam OWC attenuator, International Journal of Marine Energy 12 (2015) 21–34. doi:10.1016/j.ijome.2015.08.005.

[20] H. Bingham, R. Read, F. Jakobsen, M. Simonsen, P. Guillen, D. Ducasse, K. Nielsen, An experimental and numerical analysis of an I-beam attenuator-type, oscillating water column wave energy converter, in: Renewable Energies Offshore, CRC Press, 2015, pp. 437–443. doi:10.1201/b18973-62.

[21] H. B. Bingham, D. Ducasse, K. Nielsen, R. Read, Hydrodynamic analysis of oscillating water column wave energy devices, Journal of Ocean Engineering and Marine Energy 1 (4) (2015) 405–419. doi:10.1007/s40722-015-0032-4.

[22] K. Nielsen, H. Bingham, J. B. Thomsen, On the absorption of wave power using ship like structures, in: Proceedings of the Twenty-eighth (2018) International Ocean and Polar Engineering Conference, pp. 719–726.

[23] J. N. Newman, Marine hydrodynamics, MIT Press, Cambridge, Mass, 1977.

[24] J. Falnes, Ocean Waves and Oscillating Systems, Cambridge University Press, 2002.
URL https://www.ebook.de/de/product/3895081/johannes_falnes_ocean_waves_and_oscillating_systems.html

[25] H. B. Bingham, Y.-H. Yu, K. Nielsen, K.-H. Kim, S. Park, K. Hong, H. A. Said, T. Kelly, J. Ringwood, R. W. Read, E. Ransley, S. Brown, D. Greaves, Ocean energy systems wave energy modelling task 10.4: Numerical modelling of a fixed oscillating water column, Energies 14 (6) (2021) 1718. doi:10.3390/en14061718.

[26] J. N. Newman, C.-H. Lee, WAMIT; a radiation-diffraction panel program for wave-structure interactions.

[27] W.E. Cummins, The impulse response function and ship motion, Schiffstecknik 9 (1962) 101–109.

[28] MathWorks, MATLAB (Accessed February 27, 2023).
URL https://se.mathworks.com/

[29] J. B. Trevino, Experimental investigation of one-way energy capture by an OWC wave energy device, Master's thesis, Technical University of Denmark, Department of Mechanical Engineering (2020).

[30] Edinburgh Designs, Wave Gauge Software Manual (2018).

[31] W. Emery, Data analysis methods in physical oceanography, Elsevier, Amsterdam New York, 2001.

[32] H. B. Bingham, R. Read, DTUMotionSimulator; a MATLAB package for simulating linear or weakly nonlinear response of a floating structure to ocean waves, https://gitlab.gbar.dtu.dk/oceanwave3d/DTUMotionSimulator (2022).

[33] N. Ansarifard, , A. Fleming, A. Henderseon, S. Kianejad, S. Chai, Comparison of inflow and outflow radial air turbines in vented and bidirectional owc wave energy converters, Energy 182 (2019) 159–176. doi:10.1016/j.energy.2018.10.068.

Chapter 6

Economic feasibility study for wave energy conversion device deployment in Faroese waters

The paper entitled ”Economic feasibility study for wave energy conversion device deployment in Faroese waters” has been submitted to the Journal of Energy as:

Bárdur Joensen and Harry B. Bingham. “Economic feasibility study for wave energy conversion device deployment in Faroese waters”. Submitted.

Economic feasibility study for wave energy conversion device deployment in Faroese waters

Bárður Joensen[a,b,*], Harry B. Bingham[b]

[a] *LBF Consulting Engineers, Niels Finsensgøta 10, FO-110 Tórshavn, Faroe Islands*
[b] *Technical University of Denmark, Department of Civil & Mechanical Engineering, Section for Fluid Mechanics, Coastal and Maritime Engineering, Nils Koppels Allé building 404, 2800 Kgs. Lyngby, Denmark*

Abstract

As the world continues to battle with the increasing energy demand along with the seroius effects of climate change, there is a need for more reliable renewable energy sources. The objective of the present work is to study the economic feasibility for deployment of wave energy conversion devices in the Faroese coastal region. We analyze eight different wave energy conversion concepts under development at nine different nearshore locations in the Faroese coastal region. The nine different locations are classified into three coastal locations - three on the west coast, three on the east coast and three on the north coast. The nine wave energy conversion devices mainly rely on different working principles, though some of these are similar. Results show that there is quite a significant difference in the performance of the devices from coast to coast. There is also a difference between the different conversion devices as they rely on different principles and the suitability of each device varies from location to location. We also show that the Faroe Islands are a suitable location for wave energy converter deployment compared to other places. Furthermore, results show that the performance of wave energy converters in the Faroe Islands can prove to be a direct competitor to offshore floating wind energy.

Keywords: Wave energy conversion, Economic feasibility WECs, Faroe Islands, Levelised-cost-of-energy

1. Introduction

The need for developing efficient, optimal and robust technologies for capturing power from renewable resources grows by the minute. The effects from climate change are already disastrous, with recorded extreme heat records all across Europe [1]. As power production transitions from a stable generation from coal, oil, natural gas, nuclear fission, etc., to a more unstable generation from renewables, there is a need for a variety of different renewable sources to feed in to the electricity grid [2]. A clean and efficient source of renewable energy is wave power. This resource has been extensively tested and investigated, but up to this point there are no large-scale commercially available technologies for power generation from waves. However, there are many different companies/technologies on the doorstep to enter the commercial stage. Some examples include: CorPower [3], Mocean [4], EcoWave Power [5], Wave Dragon [6], Wavepiston [7], ExoWave [8], KNSwing [9] and NoviOcean [10].

To make a power generation technology attractive and interesting, there is a need for optimization with regards to the economic perspective. This is one factor which has failed in the past when considering wave power - it has simply been too expensive to produce power from ocean waves, compared to other renewable sources, e.g. offshore wind [11]. The most common metric for the economic assessment is the levelised-cost-of-energy (LCoE), which is defined in Section 2.5.

*Corresponding author
Email address: bajoe@mek.dtu.dk (Bárður Joensen)

Several studies have focused on investigating the economics of wave power for a specific region based on the available level of data from ocean waves. Ref. [12] identified potential sites and assessed the technical and economic feasibility of harnessing wave energy along the Indian coast. The authors analysed four different wave energy conversion technologies: Wave Dragon, Pelamis, Oceantec and Aquabuoy. They found that the most economically feasible technology was the Oceantec device which had a LCoE ranging from 354 to 505 EUR/MWh at all sites.

Ref. [13] explored the potential benefits of co-locating a wave energy device with an offshore floating wind farm located off the coast of northern Portugal. The authors conclude that the co-located farm would increase the energy production by 19 % and the LCoE level with a co-located wave farm is at 105 EUR/MWh.

Ref. [14] examines the feasibility of a hybrid wave-photovoltaic (PV) system in three ports of Iran. They found that the maximum energy production occurred in May and the minimum energy production occurred in November. For the three ports, they found LCoE values of 4420 EUR/MWh, 5010 EUR/MWh and 5120 EUR/MWh, respectively.

Ref. [15] studied the economic feasibility of two wave energy conversion devices along the coast of Brazil: Pelamis and Wave Dragon. They found a LCoE value for the Pelamis device of 149 EUR/MWh and 126 EUR/MWh for the Wave Dragon device.

Ref. [16] investigated the economic feasibility of the Pelamis, the AquaBuoy and the Wave Dragon device off the coast of northern Spain. They found the best LCoE values for the Wave Dragon at 513.17 EUR/MWh, the Pelamis at 1710.98 EUR/MWh and the AquaBuoy at 2627.60 EUR/MWh.

In [17], the authors investigate the economic feasibility of the same devices as in [16], but for the coast of Portugal. They found here that the Wave Dragon had a LCoE value of 316.90 EUR/MWh, the Pelamis had a LCoE value of 735.94 EUR/MWh, while the AquaBuoy was all the way up at 2967.85 EUR/MWh.

In [18] the authors investigated the economic feasibility of the backward bent duct buoy (BBDB) oscillating water column (OWC) device. The authors investigated the economics with regards to three different discount rates, three different efficiency levels and two different initial capital costs in units of EUR/kW of rated power. The LCoE values ranged from 81 EUR/MWh with the lower capital cost value, the maximum efficiency level and the lowest discount rate, to 1335 EUR/MWh with the higher initial capital cost, the lowest efficiency level and the highest discount rate.

In recent years there has been a special focus on using ocean renewables to supply oil and gas platforms in order to reduce the energy consumption for their oil and gas extraction. Ref. [19] assessed the performance and economic feasibility of seven wave energy devices for a case study site located at an oil and gas platform in the North Sea. They found that the hydrodynamic performance of the wave energy device is not necessarily directly linked with the economic attractiveness. They found that the LCoE ranged from 188 EUR/MWh to 471 EUR/MWh.

In [20], the authors investigate the feasibility of implementing combined wave and solar systems for supplying power to offshore oil and gas platforms. They assessed four wave energy converters and one solar power system for three scenarios: wave power only, solar power only and both combined. Results showed that a combination of electricity sources increased the electricity production, reduced the intra-annual variability of energy production and intermittency issues, increased capacity factors up to 24 % and avoided over dimensioning. The LCoE level ranged from 131 EUR/MWh to 263 EUR/MWh and the reduction in emissions was estimated at approximately 281,915 tons/year.

No study concerning the economic feasibility of wave energy converters exists for the Faroe Islands, which according to [21] might prove to be a viable candidate for the first real community running fully on wave power for electricity generation. Small island communities might prove to be ideal candidates for wave power generation, since the demand is not as high as in a cross-country electrical grid network [22].

1.1. Contributions and Novelty

The present study analyzes the performance in the Faroese coastal waters of eight different wave energy conversion devices currently under commercial development. The performance of the devices are analyzed at nine different locations and is based on:

- An energy production perspective, through the prediction of the annual energy production (AEP) of each device at each location.
- An efficiency perspective, through an estimate of the capacity factor (CF) for each device at each location.
- An economic perspective, by estimating the levelised-cost-of-energy (LCoE) for each device at each location.

Based on the numbers derived from the above calculations, the more promising and cost-competitive devices are compared to offshore floating wind power. This is the real competitor to the wave energy conversion devices analysed (for Faroese conditions), since due to the steep water depth contours around the Faroe Islands, offshore bottom-fixed wind power seems to be unrealistic.

These contributions will hopefully stimulate the desire for wave energy developers and potential investors to see the Faroe Islands as a realistic candidate for one of the world's first large scale commercial wave farms. This study highlights that the Faroe Islands are one of the best suited locations worldwide when considering energy production, capacity factor and cost of energy. Furthermore, it highlights that for Faroese conditions, wave power is truly a competitor to offshore floating wind power.

2. Theory and methods

The main working principles of wave energy conversion devices are generally categorized into four types: 1) wave over-topping devices, 2) oscillating water columns, 3) lift-based devices, and 4) wave activated bodies. Other, less commonly used working principles also exist, e.g. submerged pressure differential devices, internal rotating mass and bulge wave devices; but these can generally be absorbed into the main categories [23]. Absorbers based on each of these working principles can further be deployed in one of three main configurations: a) point absorber, b) wave attenuator and c) wave terminator, as illustrated in Figure 1. This classification is based on the relative size of the device compared to a typical wavelength and its orientation with respect to the direction of wave travel.

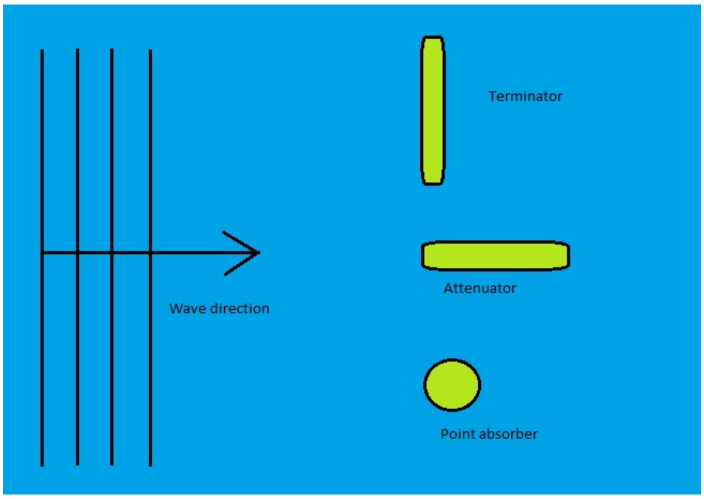

Figure 1: Attenuator, terminator and point absorber working principle.

2.1. Wave energy conversion working principles

2.1.1. Wave overtopping devices

Wave over-topping devices capture the water as the waves propagate up a ramp and break in to a reservoir. The water then returns to the sea through conventional hydro turbines generating electricity. Two well known devices are the Wave Dragon [24] device and the Sea Slot-cone generator (SSG) [25]. In this study we have focused on the Wave Dragon as this device is still under development. A sketch of the Wave Dragon is shown in Fig. 2 and an artistic impression of the SSG device is shown in Fig. 3. The Wave Dragon device is

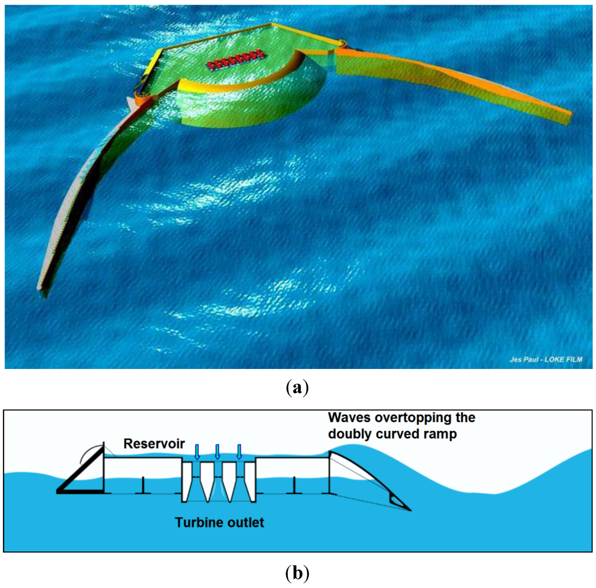

Figure 2: A schematic sketch of the working principle of the Wave Dragon device, from [26].

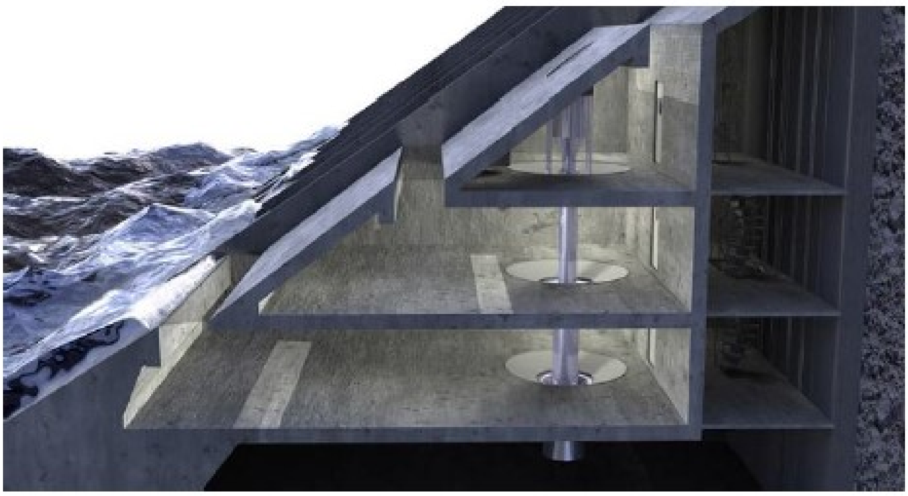

Figure 3: Artistic impression of the SSG wave energy device, from [27].

developed by a Danish company carrying the same name as the device - Wave Dragon Aps - and has been under development for more than 20 years.

2.1.2. Oscillating water column devices

The oscillating water column wave energy device has been subject to vast research and development for more than a century. Oscillating water column devices can be both fixed and floating, as well as nearshore and offshore devices. An oscillating water column is a partially submerged, hollow structure. It is open to the sea below the waterline, enclosing a column of air on top of a column of water. Waves cause the water column to rise and fall, which in turn compresses and decompresses the air column. The trapped air is allowed to flow to and from the atmosphere through a turbine, which usually can rotate in the same direction regardless of the flow direction. The turbine rotation is used to generate electricity. A schematic of the working principle of an oscillating water column is shown in Fig. 4.

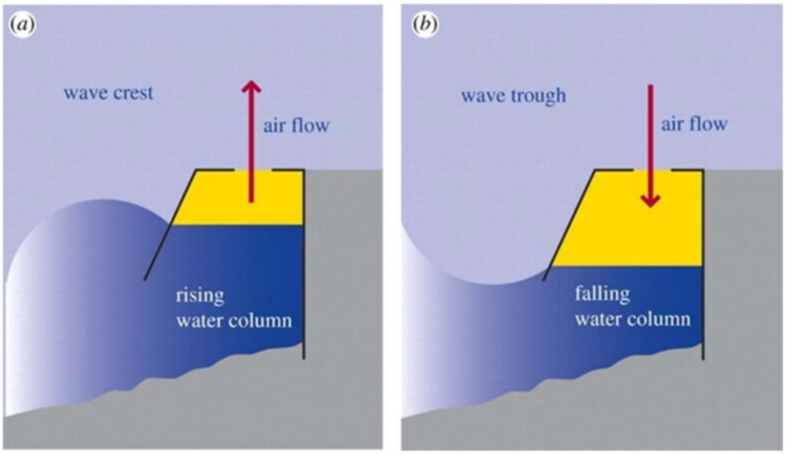

Figure 4: Oscillating water column working principle, from [28].

In this study we have focused on the KNSwing device, having an oscillating water column as the main driver for electricity generation. This is an offshore floating device, deployed as a wave attenuator device. The KNSwing is a long ship-like barge structure with the main direction of the device parallel to the direction of wave propagation (more details under *Wave attenuators*).

2.1.3. Lift-based devices

The concept of lift-based wave energy converters is relatively new, compared to the other working principles. As stated in [29] few studies exist that deal with these types of wave energy devices. However, in recent years, this type of wave energy conversion concept has received a great deal of attention. The LiftWEC project [30], a large project consortium consisting of 10 partners, deals with the many different aspects of development of a lift-based wave energy converter. Ref. [31] has made a numerical benchmarking of the CycWEC lift based wave energy converter developed at Atargis Energy Corporation [32].

In contrast to the conventional type of wave energy converter types, which utilize buoyancy and radiation/diffraction forces to drive the motion of the structure, the lift-based WECs, as the name indicates, utilize the lift forces on the structure to drive the motion. The main structure comprises of one or more hydrofoils which rotate about an axis perpendicular to the incoming wave direction.

Even though we don't have an actual lift-based device in this analysis, we believe it is important to mention this type of wave energy converter, due to its potential as a new way of approaching wave energy capture.

2.1.4. Wave activated bodies

Contrary to OWC and overtopping wave energy conversion principles, wave activated bodies are directly affected by the action of the waves. In wave activated bodies, the wave motion directly drives the power-take-off system for electricity generation from kinetic energy. Wave activated bodies mainly encompass two driving mechanisms - translational motion of the body and/or rotational motion of the body. Fig. 5 shows an example of a wave energy converter using the rotation of the body as the driving mechanism for the power-take-off.

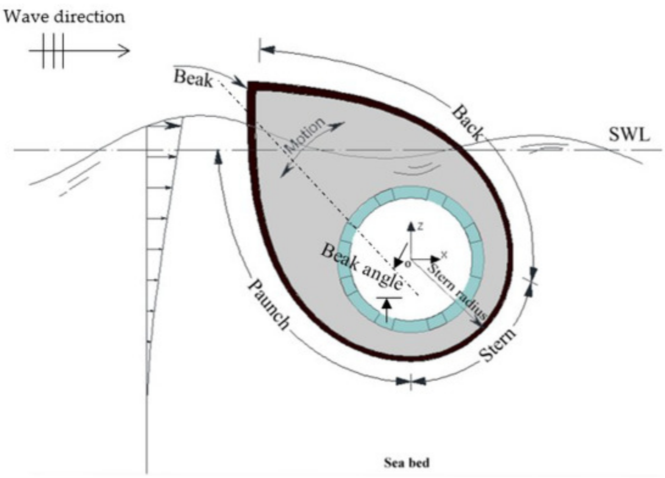

Figure 5: Example of a wave energy converter using the rotational motion of the main body as the driving mechanism for the power-take-off, from [33].

2.2. Wave energy conversion configuration types

Any of the above mentioned working principles (or even combinations of them) can be deployed in one of three main configurations - *a point absorber*, a *wave attenuator* or a *wave terminator*, which will be described in detail in the following.

2.2.1. Point absorbers

A point absorber is a floating device which is small relative to the wavelength of the incident waves. It typically has only one or two power-absorbing degrees of freedom and could be based on any of the above-described working principles.

In this study we have focused on the CorPower C12 device [3], which is planned to be operational in 2028-2030. The EcoWave Power device [5] is a modification of a point absorber, with a floater attached to a piston. Fig. 6 shows an illustration of the most common working principle for a point absorber wave energy device.

2.2.2. Wave attenuators

A wave attenuator is much longer than the target wavelength and oriented with its axis parallel to the direction of wave propogation. The device typically has many degrees of freedom to capture energy as the waves travel along its length. The KNSwing device shown in Fig. 7 is a good example of an attenuator. It is a long barge with 40 OWC chambers, slack-moored to align itself with the dominant direction of wave propagation.

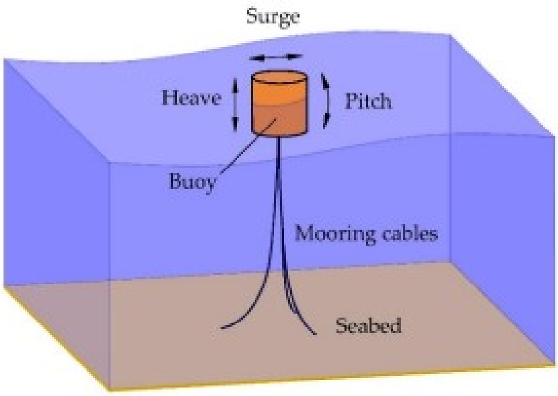

Figure 6: Point absorber working principle, from [34].

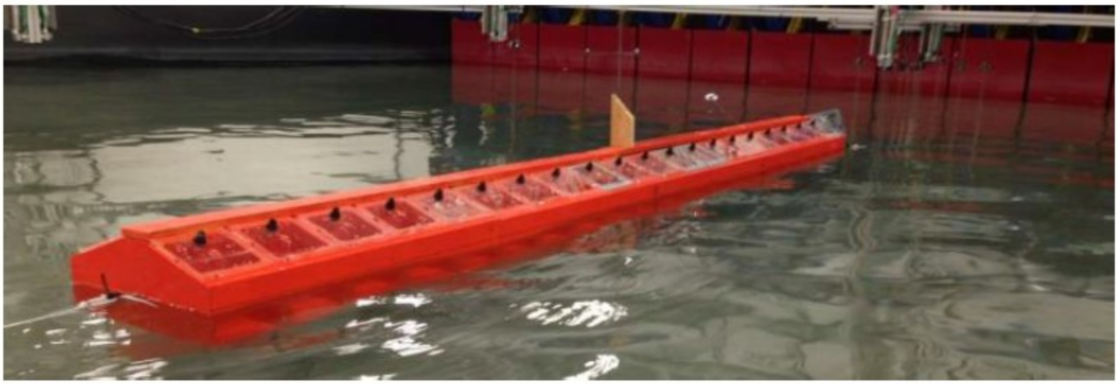

Figure 7: Experimental model scale of the KNSwing device, from [35].

2.2.3. Wave terminators

A wave terminator is also typically much longer than the target wavelength, but with its axis oriented perpendicular to the direction of wave propagation. A classic example of a wave terminator device is the famous spine duck, invented by Dr. Stephen Salter in 1974 [36]. Fig. 8 shows an impression of the spine duck. The WaveDragon concept is a wave overtopping device with only one power-absorbing degree of freedom which is deployed as a wave terminator. Fig. 9 shows pictures of the Wave Dragon converter deployed as a 1:4.5 scale protoype device tested in Nissum Bredning.

2.3. Wave data locations

The wave data used in this study is from an earlier study published in [21], where the spectral wave model, MIKE 21 SW [38] was used to model the wave climate around the Faroe Islands. The numerical calculations were extensively validated against wave buoy measurements and are thus taken to be reliable. We have selected nine locations for analysis in total - three on the west coast, three on the east coast and three on the north coast, as it was deemed that there was little variation between the three locations on each of the coasts. Fig. 10 shows a map of the selected locations.

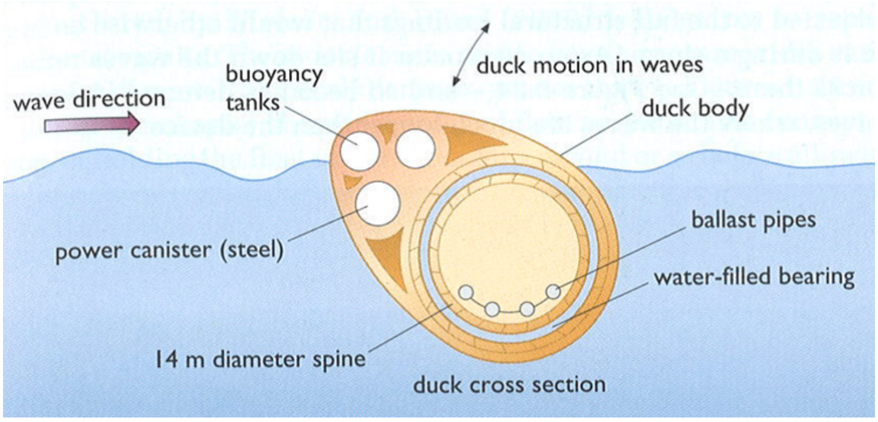

Figure 8: Sketch of the working principle of the spine duck, from [37].

Figure 9: 1:4.5 scale of the Wave Dragon converter, from [23]

2.4. Wave energy device power performance

To evaluate the power performance of the different devices analyzed in this study, we use the same methodology as in [39] to compute the average absorbed power, where the power matrix of each device is multiplied by the scatter diagram of sea states at each location and summed together for all sea states, resulting in

$$P_{abs} = \sum_{i=1}^{N} \sum_{j=1}^{M} P_{ij}\, f_{ij} \tag{1}$$

Figure 10: Map of the selected locations.

where N is the number of wave period bins, M is the number of wave height bins, P_{ij} is the power absorption coefficient corresponding to wave condition i, j (the power matrix) and f_{ij} is the occurrence frequency of the sea-state (H_{m0}, T_p) in the i^{th} and j^{th} bin. A visualization of the procedure is shown in Fig. 11

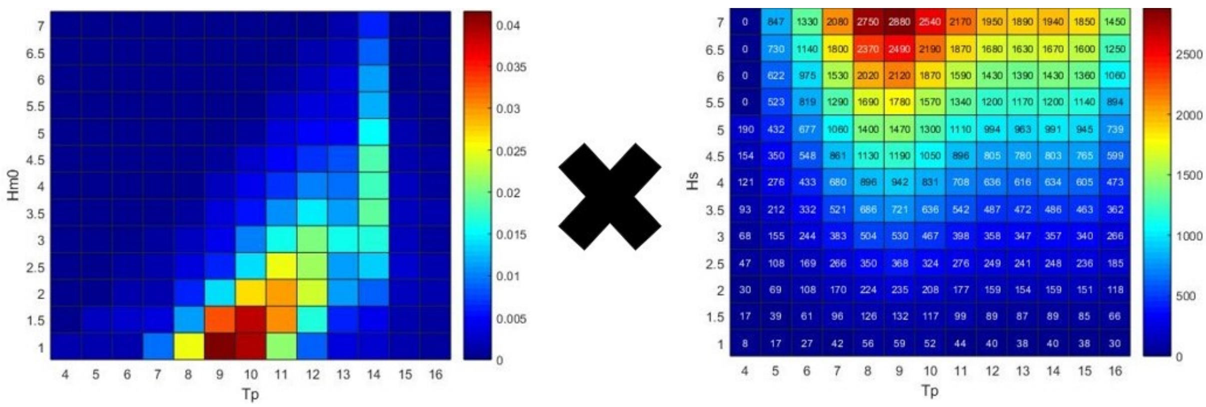

Figure 11: Visualization of the calculation of absorbed power by use of scatter diagram (left) and power matrix (right).

The annual energy production (AEP) of each device is calculated as the average absorbed power of the device multiplied by the operating hours in a year, assuming the device being fully operational in a year:

$$AEP = P_{abs}\,8766. \tag{2}$$

As it is not realistic that the device is fully operational throughout the whole lifetime of the device, the downtime due to storm limitations, maintenance, etc. is usually incorporated when calculating the total energy production of the device as some percentage.

The capacity factor (CF) of a device is a relationship between the annual average power and the rated power capacity R_P of the device through the equation:

$$CF = \frac{P_{abs}}{R_P} \tag{3}$$

The capacity factor is a metric to determine how well each device is able to absorb the power from the environmental conditions at the given location.

2.5. Levelised-Cost-of-Energy

The Levelised-Cost-of-Energy (LCoE) is an important metric when discussing the potential deployment of any given energy generation device. The cost of producing (and purchasing) energy is most likely the dominating metric when planning a potential deployment of any type of power plant - wind power, solar power, tidal power, wave power, thermal power, etc. The LCoE is defined as the total cost of commissioning, operating and maintaining the power plant divided by the total energy produced over the lifetime of the plant.

$$LCoE = \frac{CaPeX + OPeX\,L_t}{E_P} \tag{4}$$

where $CaPeX$ is the capital expenditure for the device, $OPeX$ is the cost related to operation and maintenance of the device, L_t is the lifetime of the device (including downtime due to maintenance and storm) and E_P is the total energy production over the lifetime of the device. This is a more conservative version of the cost of energy definition, because it does not take into account any effects of a possible discount rate on the operational costs or the energy production. By accounting for the discount rate it is possible to get a more realistic estimate of the LCoE over the whole lifetime of the wave energy device.

$$LCoE = \frac{\sum_{t=1}^{n} \frac{CaPeX_t + OPeX_t}{(1+r)^t}}{\sum_{t=1}^{n} \frac{E_P}{(1+r)^t}} \tag{5}$$

where n is the number of years the device is operational and r is the discount rate. We have used the latter definition of the LCoE as this gives a more realistic estimate of the cost of energy. Ref. [23] gives a nice overview of the parameters that should be taken into account when calculating the cost of energy.

2.6. Wave energy devices investigated

As mentioned above, we have investigated a number of different wave energy conversion devices currently under development - most of them on a commercial stage, while for the development of the KNSwing device has been conducted by universities and academic institutions.

CorPower Ocean device

The CorPower Ocean wave energy converter is a point absorbing device, with a heaving buoy on the surface absorbing energy from ocean waves. The buoy is connected to the seabed using a tensioned mooring system. The energy stored in the waves is converted into electricity through the rise and fall as well as back-and-forth motion of the waves. The composite buoy, interacting with this wave motion, drives a Power-Take-Off inside the buoy that converts the mechanical energy into electricity. According to CorPower, the device is at a Technology Readiness Level (TRL) at 7 [3]. A description of the TRL can be found in [23].

Eco Wave Power

The Eco Wave Power device is comprised of floaters attached to a harbour or coastal structure. The floaters draw energy from the incoming waves by converting the rising and falling motion of the waves into a clean energy generation process. The movement of the floaters compresses and decompresses hydraulic pistons which pump bio-degradable hydraulic fluid to land-based located accumulators. A pressure is built in the accumulators which rotates a hydraulic motor, which subsequently rotates a generator, converting mechanical energy into electricity to the grid via an inverter [5]. The numbers provided from the developer for the CAPEX in the analysis for the Eco Wave Power device do not include installation costs and grid connection. According to [40], the percentage share of installation and commissioning is about 13 %. Therefore, this percentage has been added by the authors in the analysis for the Eco Wave Power device.

Exowave

The Exowave wave energy converter, is in principle an oscillating wave surge converter, which extracts the kinetic energy from the ocean waves through bottom-hinged flaps. The flaps are activated by wave-induced orbital motion of the water and pivot about the horizontal shaft. The shaft is connected to a swivel that automatically orients the flap in the direction of the waves. The flap then drives a crank which actuates a cylinder pump [8]. Using Exowave's own name convention the flaps are called cells, while each block consists of three cells and subsequently each cluster consists of 10 blocks.

Wavepiston

The Wavepiston device consists of several energy collectors attached to the same spine-like structure. The energy collectors are vertical plates that move horizontally back and forth due to surging wave action. The energy collectors pump seawater through a pipe, to a water turbine that converts the pressurized water to electricity. The long structure is moored at both ends [7].

Wave Dragon

The basic principle of the Wave Dragon device is to use well-known and well-proven principles from traditional hydro-power plants in an offshore floating platform. The Wave Dragon over-topping device elevates the ocean waves to a reservoir above sea level where water is let out through a number of turbines and in this way it is transformed into electricity [6].

KNSwing

The KNSwing device is a long ship-like structures with oscillating water columns along both sides, where it absorbs the wave energy as it passes down along its hull. Traditionally, oscillating water column devices use bi-directional or self-rectifying turbines to generate electricity. The assumptions behind the calculations of the KNSwing device is such that a PTO efficiency of 49% is used (as per the developer). However, by increasing the efficiency of the PTO to up to 75-80%, by utilizing one-way energy absoprtion as is done in [41] this would lead to a significant increase in the annual energy production and capacity factor, while a significant decrease in the LCoE will be achieved.

Mocean Energy Blue Horizon device

The Mocean Energy Blue Horizon device is a hinged raft type of wave energy converter. It is inspired by the Pelamis device [42], but is simpler as it only consists of one hinge, compared to the several hinges of the Pelamis device. It is an attenuator device, i.e. it faces the waves head on and has a power rating of 200 kW.

NoviOcean NO500

The NoviOcean wave energy converter is a non-resonant buoyant device that extracts energy from the vertical motion (heave) of the waves. It is essentially comprised of two main subsystems which are both unique to the wave energy industry - the "rectangular float" and the "inverted hydropower plant PTO". The HPAS (Hydro Power Plant at Sea) is the result of merging these unique subsystems [10].

In Table 1 we have provided the main parameters of each device, e.g. largest dimension L, mass m and rated power P_r:

Table 1: Main specifications for each device.

	L [m]	m [ton]	P_r [kW]
CorPower	11.25	87.5	400
Eco Wave Power	3.6	1.6	1000
Exowave	12	100	350
Wavepiston	320	95	500
Wave Dragon	270	33000	7000
KNSwing	150	12000	1000
Mocean			200
NoviOcean	38	150	500

The values for length and weight of the Eco Wave Power device are for each floater, while the rated power is for the whole device comprising of 100 floaters. The company Mocean Energy wishes to keep the specifications on their device confidential, as this device is currently under development and the design is constantly evolving. Therefore, only the rated power of the device is provided.

3. Results and discussion

3.1. Annual energy production

The annual energy production of the devices varies a lot since they span a large range of sizes and rated powers. The annual energy production of each device at each location is calculated from Eq. 2. The results are presented in Fig. 12.

Fig. 12 shows that the energy production roughly follows the rated power of the devices, and increases with the increasing wave climate from eastern to northern to western locations. The Wave Dragon device, with a rated power of seven times the next highest rated device, always produces the most energy. Considering the Eco Wave Power and KNSwing devices, which have the same rated power, the Eco Wave Power device is more productive on the east coast while they are fairly similar on the north coast and the KNSwing device has a larger annual energy production on the west coast. This is presumably due to the different distributions of the two power matrices.

The Exowave and the Mocean device are amongst those with the lowest energy production. However there is a clear variation between the devices for each of the locations. For the east locations the Mocean device outperforms the Exowave, while for the west locations the Exowave has the highest production.

The Wavepiston device and the CorPower device have similar annual energy production at most locations, however at the E3, N1 and N2 the CorPower device overperforms the Wavepiston device.

It is particularly interesting to note that the devices that fall in the same amount of energy production, actually rely on different working principles and power-take-offs. In terms of energy production, the Wave Dragon device is in a category for itself, as well as in terms of working principle being an overtopping device. The KNSwing device and the Eco Wave Power device have somewhat similar energy production, with the KNSwing device being an attenuator device equipped with OWCs and the Eco Wave Power device being a collection of point absorbers. The Exowave converter is a bottom mounted oscillating wave surge converter and the Mocean device is an attenuating hinged-raft.

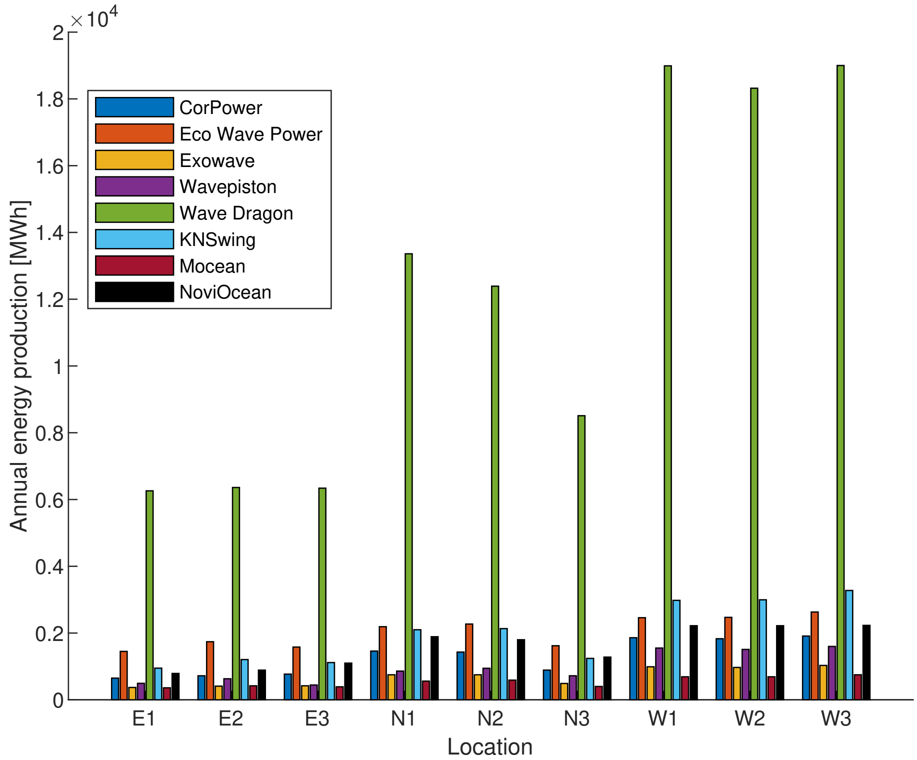

Figure 12: Annual energy production of each device at each location.

3.2. Capacity factor

The capacity factor of any renewable energy device is the ratio of average yearly produced power to rated power. Fig. 13 shows the capacity factor of each device at each location. The figure shows that the Mocean device has the largest capacity factor for the E1 and E2 locations, while for the E3 location the NoviOcean device has the largest capacity factor. For the north locations the NoviOcean device has the largest capacity factor, while for the west locations the CorPower device has the highest capacity factor.

At the opposite end, the Wavepiston device has the lowest capacity factor at all locations except the E2 location where Wave Dragon has the lowest value and having the second lowest at the other east and north locations. The Eco Wave Power has the second lowest capacity factor for the west locations.

The Eco Wave Power device is approximately in the middle compared to the other devices for the east and north locations, while for the west locations it is at the lower end. The Exowave device is mostly in the middle with regards to capacity factor compared to the other devices in all locations.

It is interesting to note that the best capacity factors in the most energetic western locations are comparable to the best values which have been obtained by offshore wind farms.

3.3. Levelised-cost-of-energy

The LCoE is probably the most important parameter for prospective investors in renewable energy, because it predicts the price of the energy. Fig. 14 shows the LCoE in EUR/MWh for each of the considered devices at each location. The Wavepiston device has the highest price of energy at E1, E2, E3, N1 and N2, while the KNSwing device has the highest energy price at N3 and the Mocean device has the highest energy price at all west locations. At the opposite end, the Eco Wave Power device has the lowest price of energy at the east locations E1 and E2, where the CorPower device has the second lowest and the Wave Dragon

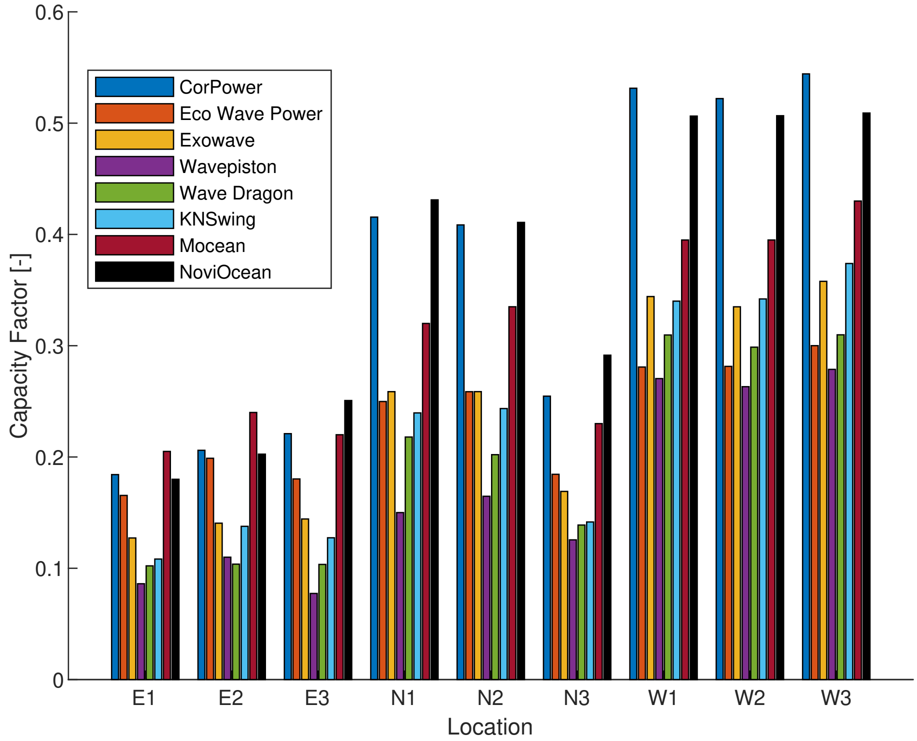

Figure 13: Capacity factor of each device at each location.

has the third lowest at these locations. For the north locations N1 and N2 the CorPower device is lowest just below the NoviOcean device, while the Wave Dragon has the third lowest energy price. At the west locations the CorPower device, the Wave Dragon device and the NoviOcean device have by far the lowest price of energy at approximately 61-62 EUR/MWh and 62-64 EUR/MWh and 68 EUR/MWh, respectively. In the west locations the KNSwing, Exowave, Wavepiston and Eco Wave Power come in somewhat higher at 83, 91 and 92 EUR/MWh for KNSwing, 84, 88 and 89 EUR/MWh for Exowave, 94, 96 and 99 EUR/MWh for Wavepiston and 96, 102 and 103 EUR/MWh for Eco Wave Power.

It is important to highlight, that the assumptions behind the cost estimates for each of the devices vary from developer to developer, as some devices are better suited for some locations compared to others. Furthermore, the numbers provided on CAPEX and OPEX from the developers are based on estimates, and not on in-depth analyses of the actual costs for installation and maintenance. Also the cost estimates are based on installation capacities of several 10's of MW and in some cases 100's of MW, and not on single device deployment as these would not make any sense with regards to commercialization. Given the inherent uncertainties in such cost projections, the numbers shown in Fig. 14 should be taken as indicative of the likely range for LCoE at each of these locations rather than precise values for these specific concepts.

3.4. Comparing the Faroe Islands case with other locations

As mentioned in the Introduction, several studies have been conducted to assess the economics of wave energy in different parts of the world. Therefore, it is natural to compare the results from these studies with the Faroe Islands assessment to determine the suitability of deploying wave energy converters in the Faroe Islands compared to other locations worldwide.

As only a few of the wave energy devices investigated in this study have been analysed in other regions of the world, we will here focus on the ones that have been analysed elsewhere.

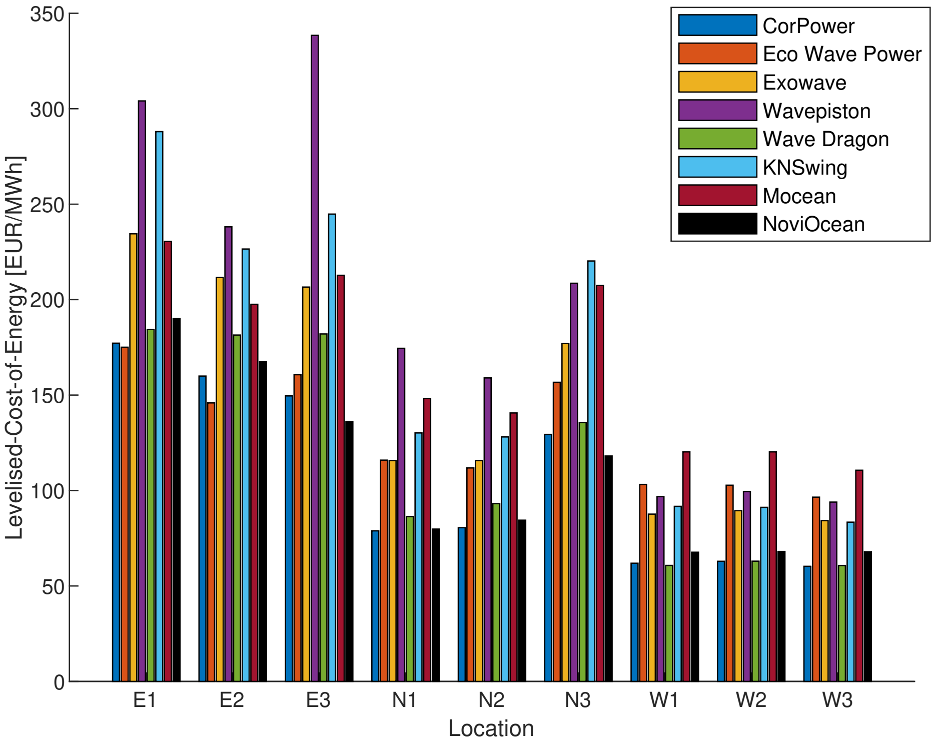

Figure 14: Levelised-cost-of-energy of each device at each location.

The Wave Dragon device has been analysed for the Portuguese coast in [17], for the Atlantic coast of Spain in [16] and for the coast of Brazil in [15]. Table 2 compares the LCoE of the Wave Dragon for the different locations. As Table 2 shows, the numbers vary a lot. This is partly associated with the difference

Table 2: LCoE for the Wave Dragon device at different locations.

Faroe Islands	Portugal	Spain	Brazil
[EUR/MWh]	[EUR/MWh]	[EUR/MWh]	[EUR/MWh]
61.8	316.9	513.17	129.95

in wave energy flux at the different locations, along with different assumptions behind the CAPEX behind the calculations.

The NoviOcean NO500 device has been analyzed for a number of places around the globe. On the company's website, they've presented numbers for LCoE in terms EUR/MWh and the capacity factor in percentage. Furthermore, they provide a rather detailed cost model for the CAPEX and OPEX, based on the array power rating, the water depth and the distance to the nearest port. From this it is possible to derive values for the LCoE, CF, AEP, etc. We have compared the NoviOcean NO500 device at a number of sites presented on the company's website and for the most favorable site in this study in terms of LCoE. Table 3 shows the LCoE in EUR/MWh for the selected sites compared with the Faroese site. Table 3 shows that the numbers for the LCoE are in the same order of magnitude - indicating that the assumptions for

Table 3: LCoE for the NO500 device at different locations.

Faroe Islands	Haltenbanken	Belmullet	Lisbon
[EUR/MWh]	[EUR/MWh]	[EUR/MWh]	[EUR/MWh]
68	84	68	79

the calculation of the LCoE are identical. Therefore it can be stated that this is a more realistic comparison compared to the one in Table 2.

Many of the companies owning the devices analyzed in this study have a long term projection of the LCoE in order commercialize their devices. These long term projections are derived from expected and estimated trends in the global economy, which we see now has taken a turn towards higher inflation in the aftermath of the COVID-19 pandemic. CorPower Ocean states in the presentation of the EUScores project [43] that the LCoE for their device will drop to 70 EUR/MWh when they have an installation capacity of 600 MW - which is well in line with the results for the more favorable locations in this study. Wavepiston presents on their website that at pre-commercial scale in 2025 they've reached a LCoE of 200 EUR/MWh, while their utility scale energy price will be as low as 40 EUR/MWh in 2032. This is also well in line with the results obtained in this study - which are taken to be estimates for 2028-2030 landing on a LCoE of 94 EUR/MWh for the most favorable location.

It is worth noting that the internal differences between the devices, mostly in terms of LCoE and slightly in terms of capacity factor, vary to quite a significant extent from location to location. This is due to the suitability of each device for each of the analyzed locations. The scale and size of the analyzed devices are given beforehand and not optimized to each of the locations, leading to a significant "waste" in materials, due to the inability of the device to produce energy to their full potential. Therefore, each analyzed device should be optimized with regards to the intended deployment location, such that the resonance period of the respective device is as close as possible to the most frequently occurring wave period at the location. This was done in [21] where the authors analyzed four types of wave energy devices in Faroese coastal waters in terms of the capture width ratio (CWR) of each device, allowing for the possibility of varying the size of the devices in order to match optimal energy production conditions. As the aim of this current study was to analyze wave energy conversion devices currently under commercial development, we did not want to alter any of the dimensions of the devices in order to suit the specific deployment location.

3.5. Comparison with offshore floating wind power

As the offshore wind power industry has already reached a commercial level and is in rapid growth [44], this is the main competitor for the wave power industry to reach commercialization. Tidal power is also making a large impact and significant progress [45], but this technology is approximately at the same maturity level as the wave power industry. Some studies have been conducted in order to map out the levelised-cost-of-energy of wind power in the Northeast Atlantic Ocean, e.g. [46] and [47]. In [46] the authors conclude that the LCoE of offshore floating wind power in locations close to the Faroe Islands are approximately 95 EUR/MWh. These number are valid for locations some kilometers off the shore in the Faroe Islands. Comparing this to the LCoE for some of the lowest values from the wave energy converters analyzed in this study (62 EUR/MWh for CorPower, 62 EUR/MWh for Wave Dragon and 68 EUR/MWh for NoviOcean NO500), deployment of wave energy conversion devices is truly a competitor to the offshore floating wind power industry.

However, the authors in [46] highlight from their background review that experts anticipate 20-30% cost reduction by 2030 in offshore floating wind, leading to a LCoE level for offshore floating wind in the same range as for the above mentioned wave energy conversion devices.

4. Conclusions

In this work we have analyzed eight different wave energy converters at nine different locations in the Faroe Islands to assess their performance. The assessment is based on the annual energy production, capacity factor and the levelised-cost-of-energy. The numbers for the aforementioned parameters vary a lot between the devices, but also from location to location. The western lying locations all yield the most favorable LCoE values for all the devices.

The three most favorable devices in terms of LCoE are the CorPower device, Wave Dragon and the NoviOcean NO500 devices. These have LCoE values of 62 EUR/MWh, 62 EUR/MWh and 68 EUR/MWh, respectively, at the most energetic locations. Comparison of these values with other locations in the world, where economic feasibility studies have been conducted, the Faroe Islands are truly a suitable location for wave energy converter deployment.

Comparing the assessment of the wave energy converters with offshore floating wind power, this work concludes that wave energy is truly a competitor to offshore floating wind power in terms of levelised-cost-of-energy.

CRediT author contribution statement

Bárður Joensen: Methodology, Validation, Formal analysis, Investigation, Data curation, Writing – original draft, Writing – review & editing, Funding acquisition. **Harry B. Bingham:** Writing - original draft, Writing - review & editing, Supervision, Project administration.

Declaration of competing interests

The authors declare that they have no known competing financial interests or personal relationships that could have appeared to influence the work reported in this paper.

Acknowledgements

This study is based on project supported by the Research Council of the Faroe Islands, grant number 02010. The same project is also financially supported by Betri Research Support Group, SEV, Bakkafrost Farming, Hiddenfjord and MOWI Faroes.
The authors would also like to express gratitude to Michael Henriksen from Wavepiston, Kim Nielsen from development of the KNSwing device, Matias Sigal from EcoWave Power, Lars Wigant from Exowave, Erik Friis-Madsen from Wave Dragon, Jan Skjoldhammer from NoviOcean, Anders Jansson from CorPower Ocean and Cameron McNatt, Andrea Caio and Gabriel Scarlett from Mocean Energy for providing information on the analyzed wave energy devices.

References

[1] Metoffice, https://www.metoffice.gov.uk/about-us/press-office/news/weather-and-climate/2022/red-extreme-heat-warning-ud (Accessed 2023-02-27).
URL `https://www.metoffice.gov.uk/about-us/press-office/news/weather-and-climate/2022/red-extreme-heat-warning-ud`

[2] D. Keiner, O. Salcedo-Puerto, E. Immonen, W. G. van Sark, Y. Nizam, F. Shadiya, J. Duval, T. Delahaye, A. Gulagi, C. Breyer, Powering an island energy system by offshore floating technologies towards 100% renewables: A case for the Maldives, Applied Energy 308 (2022) 118360. `doi:10.1016/j.apenergy.2021.118360`.

[3] CorPower Ocean, https://corpowerocean.com/ (Accessed 2023-02-27).

[4] Mocean Energy, https://www.mocean.energy/ (Accessed 2023-02-27).

[5] EcoWave Power, https://www.ecowavepower.com/ (Accessed 2023-02-27).

[6] Wavedragon, https://wavedragon.net/ (Accessed 2023-02-27).

[7] Wavepiston, https://wavepiston.dk/ (Accessed 2023-02-27).

[8] Exowave, https://exowave.com/ (Accessed 2023-02-27).

[9] H. B. Bingham, D. Ducasse, K. Nielsen, R. Read, Hydrodynamic analysis of oscillating water column wave energy devices, Journal of Ocean Engineering and Marine Energy 1 (4) (2015) 405–419. doi:10.1007/s40722-015-0032-4.

[10] NoviOcean, https://noviocean.energy/concept-general-innovation-marine-blue-energy-non-resonant-buoyant/technology (Accessed 2023-02-27).
URL https://noviocean.energy/concept-general-innovation-marine-blue-energy-non-resonant-buoyant/#technology

[11] S. Astariz, A. Vazquez, G. Iglesias, Evaluation and comparison of the levelized cost of tidal, wave, and offshore wind energy, Journal of Renewable and Sustainable Energy 7 (5) 053112. doi:10.1063/1.4932154.

[12] R. P. Patel, G. Nagababu, S. S. Kachhwaha, V. V. A. K. Surisetty, M. Seemanth, Techno-economic analysis of wave energy resource for india, Journal of the Indian Society of Remote Sensingdoi:10.1007/s12524-022-01538-3.

[13] V. Ramos, G. Giannini, T. Calheiros-Cabral, M. López, P. Rosa-Santos, F. Taveira-Pinto, Assessing the effectiveness of a novel WEC concept as a co-located solution for offshore wind farms, Journal of Marine Science and Engineering 10 (2) 267. doi:10.3390/jmse10020267.

[14] M. A. Saheli, K. Lari, G. Salehi, M. T. Azad, Techno-economic assessment of a hybrid on grid PV-wave system: A case study in caspian sea, Renewable Energy 186 596–608. doi:10.1016/j.renene.2021.12.146.

[15] L. de Oliveira, I. F. S. dos Santos, N. L. Schmidt, G. L. T. Filho, R. G. R. Camacho, R. M. Barros, Economic feasibility study of ocean wave electricity generation in brazil, Renewable Energy 178 1279–1290. doi:10.1016/j.renene.2021.07.009.

[16] L. Castro-Santos, A. Bento, C. G. Soares, The economic feasibility of floating offshore wave energy farms in the north of spain, Energies 13 (4) 806. doi:10.3390/en13040806.

[17] L. Castro-Santos, D. Silva, A. Bento, N. Salvação, C. G. Soares, Economic feasibility of wave energy farms in portugal, Energies 11 (11) 3149. doi:10.3390/en11113149.

[18] L. Castro-Santos, G. P. Garcia, A. Estanqueiro, P. A. Justino, The levelized cost of energy (LCOE) of wave energy using GIS based analysis: The case study of portugal, International Journal of Electrical Power & Energy Systems 65 21–25. doi:10.1016/j.ijepes.2014.09.022.

[19] S. Oliveira-Pinto, P. Rosa-Santos, F. Taveira-Pinto, Electricity supply to offshore oil and gas platforms from renewable ocean wave energy: Overview and case study analysis, Energy Conversion and Management 186 556–569. doi:10.1016/j.enconman.2019.02.050.

[20] S. Oliveira-Pinto, P. Rosa-Santos, F. Taveira-Pinto, Assessment of the potential of combining wave and solar energy resources to power supply worldwide offshore oil and gas platforms, Energy Conversion and Management 223 113299. doi:10.1016/j.enconman.2020.113299.

[21] B. Joensen, B. A. Niclasen, H. B. Bingham, Wave power assessment in faroese waters using an oceanic to nearshore scale spectral wave model, Energy 235 (2021) 121404. doi:10.1016/j.energy.2021.121404.

[22] H. M. Tróndheim, Ensuring supply reliability and grid stability in a 100 % renewable electricity sector in the faroe islands, Ph.D. thesis.

[23] A. Pecher, J. P. Kofoed (Eds.), Handbook of Ocean Wave Energy, Springer International Publishing. doi:10.1007/978-3-319-39889-1.

[24] J. P. Kofoed, P. Frigaard, E. Friis-Madsen, H. C. Sørensen, Prototype testing of the wave energy converter wave dragon, Renewable Energy 31 (2) 181–189. doi:10.1016/j.renene.2005.09.005.

[25] L. Margheritini, D. Vicinanza, P. Frigaard, SSG wave energy converter: Design, reliability and hydraulic performance of an innovative overtopping device, Renewable Energy 34 (5) 1371–1380. doi:10.1016/j.renene.2008.09.009.

[26] S. Parmeggiani, J. Kofoed, E. Friis-Madsen, Experimental update of the overtopping model used for the wave dragon wave energy converter 6 (4) 1961–1992. doi:10.3390/en6041961.

[27] D. Vicinanza, L. Margheritini, J. P. Kofoed, M. Buccino, The SSG wave energy converter: Performance, status and recent developments 5 (2) 193–226. doi:10.3390/en5020193.

[28] N. P. Juan, V. N. Valdecantos, M. D. Esteban, J. S. L. Gutiérrez, Review of the influence of oceanographic and geometric parameters on oscillating water columns 10 (2) 226. doi:10.3390/jmse10020226.

[29] M. Folley, P. Lamont-Kane, Optimum wave regime for lift-based wave energy converters, in: Proceedings of the European Wave and Tidal Energy Conference.

[30] LiftWEC, https://liftwec.com/ (Accessed 2023-02-27).
URL https://liftwec.com/

[31] S. G. Siegel, Numerical benchmarking study of a cycloidal wave energy converter, Renewable Energy 134 390–405. doi:10.1016/j.renene.2018.11.041.

[32] Atargis, https://atargis.com/ (Accessed 2023-02-27).
URL https://atargis.com/

[33] S. K. Poguluri, I.-H. Cho, Y. H. Bae, A study of the hydrodynamic performance of a pitch-type wave energy converter–rotor 12 (5) 842. doi:10.3390/en12050842.

[34] J. Wu, On power-absorption degrees of freedom for point absorber wave energy converters 8 (9) 711. doi:10.3390/jmse8090711.

[35] K. Nielsen, J. Thomsen, KNSwing—on the mooring loads of a ship-like wave energy converter, Journal of Marine Science and Engineering 7 (2) (2019) 29. doi:10.3390/jmse7020029.

[36] S. H. Salter, Wave power, Nature 249 (5459) 720–724. doi:10.1038/249720a0.

[37] Salter's Nodding Duck, Online (Accessed 2023-02-27).
URL https://baonguyen1994.wordpress.com/introduction-to-wave-energy/ocean-wave-technologies/terminators/salters-nodding-duck/

[38] DHI, MIKE 21 Wave modelling, spectral waves FM, short description, DHI, Agern Allé 5, 2970 Hørsholm, Denmark (2017).

[39] A. Babarit, J. Hals, M. Muliawan, A. Kurniawan, T. Moan, J. Krokstad, Numerical benchmarking study of a selection of wave energy converters, Renewable Energy 41 44–63. doi:10.1016/j.renene.2011.10.002.

[40] A. Têtu, J. F. Chozas, A proposed guidance for the economic assessment of wave energy converters at early development stages, Energies 14 (15) 4699. doi:10.3390/en14154699.

[41] B. Joensen, H. B. Bingham, R. Read, K. Nielsen, J. B. Trevino, Hydrodynamic analysis of a one-way energy capture of an oscillating water column wave energy device, Journal of Energy Reports (In review) (2022).

[42] G. Dalton, R. Alcorn, T. Lewis, Case study feasibility analysis of the Pelamis wave energy convertor in ireland, portugal and north america, Renewable Energy 35 (2) 443–455. doi:10.1016/j.renene.2009.07.003.

[43] EU Scores, https://euscores.eu/ (Accessed 2023-02-27).
URL https://euscores.eu/co-location-of-offshore-wind-wave-and-offshore-solar-energy-could-lead-to-

[44] C.-H. Chen, N.-J. Su, Global trends and characteristics of offshore wind farm research over the past three decades: A bibliometric analysis 10 (10) 1339. doi:10.3390/jmse10101339.

[45] M. S. Chowdhury, K. S. Rahman, V. Selvanathan, N. Nuthammachot, M. Suklueng, A. Mostafaeipour, A. Habib, M. Akhtaruzzaman, N. Amin, K. Techato, Current trends and prospects of tidal energy technology 23 (6) 8179–8194. doi:10.1007/s10668-020-01013-4.

[46] A. Martinez, G. Iglesias, Mapping of the levelised cost of energy for floating offshore wind in the european atlantic, Renewable and Sustainable Energy Reviews 154 111889. doi:10.1016/j.rser.2021.111889.

[47] A. Martinez, G. Iglesias, Site selection of floating offshore wind through the levelised cost of energy: A case study in ireland 266 115802. doi:10.1016/j.enconman.2022.115802.

Chapter 7

Conclusions

General

This Ph.D. thesis has looked into the possibility of using wave energy conversion devices for energy production in the Faroe Islands. The aim was to investigate the suitability of the Faroe Islands as a potential deployment location for commercial scale wave energy conversion devices. Before any consideration of wave energy conversion deployment, it is important to assess the wave energy potential at the given location. As the range of selection of different wave energy devices available for energy absorption is quite large, there is a need for an evaluation of the performance and suitability of the devices at the given location. Optimization of the performance of devices is a topic of great attention, since this will most likely drive production up and the cost down. The economics involved in the deployment of wave energy devices is a dominant factor of consideration, as the price of energy is usually the driving parameter considering the choice of technology for energy absorption. Therefore, the focus of this thesis has been to address these topics.

The characterization of the wave resource is of great importance and could prove a complex matter to assess at an acceptable level. There are several methods available, e.g. satellite observations, in-situ measurements and numerical modelling. For large scale wave resource characterization numerical modelling tools are preferred, but must be validated against measurements. Choosing the right tools for this task is crucial, since this will serve as a quality assurance for the accuracy of the characterization. The first and second research questions have been answered through these topics. The first paper assessed the accuracy of the numerical spectral wave model used in the second paper, where it was found that the spectral wave model performed satisfactorily, although it had some shortcomings. The spectral wave model used for the wave resource characterization was validated through wave buoy measurements and it was found that the model performed sufficiently.

Evaluating the performance of a wave energy conversion device is necessary before considering deployment and could prove to be a tricky matter. The size or scale of the device is essential, since the resonance period of the device depends on the size of the device. This device should be designed such that it gives a best possible match to the most frequently occurring wave period at a considered deployment location. The third paper focuses on this, where it is shown that the optimal power production is highly dependent on the wave conditions at the possible site location.

Innovative strategies for optimization of existing devices could prove to drive power absorption up and material cost down. The fourth paper considered implementing a one-way valve in an oscillating water column wave energy device. Numerical calculations predicted that the power absorption would increase compared to having no valve, while the experiments did not show this same trend. This highlights the need for a very efficient release valve system, as well as improved accuracy in measurement tools.

The economics of wave energy is of great importance, since the price of energy is usually the dominant factor when considering which technologies to deploy. The wave energy sector is still at a pre-commercial stage and has to compete with other renewable technologies which are at a utility scale stage, e.g. wind power, solar power and hydro power. The fifth paper addresses the economic feasibility of wave energy converters and concludes that the Faroe Islands is a potential candidate for wave energy conversion deployment and is able to compete with, e.g. offshore wind power in terms of price of energy.

Future perspectives

For the optimization strategy implemented in the fourth paper, a need for a more efficient valve system was identified. One possibility would be to implement an active valve system, to efficiently close and open through an efficient control algorithm. This would potentially confirm the same trend as seen in the numerical calculations.

In order to efficiently assess the economics regarding wave energy conversion, an optimization of the different technologies would lead to a more cost effective solution, as the technology would be fitted to the location in consideration. Furthermore, a more in depth analysis of the costs of the devices would potentially lead to more transparent results.

References

[1] Chia-Hsiang Chen and Nan-Jay Su. "Global Trends and Characteristics of Offshore Wind Farm Research over the Past Three Decades: A Bibliometric Analysis". In: *Journal of Marine Science and Engineering* 10.10 (Sept. 2022), p. 1339. DOI: 10.3390/jmse10101339.

[2] Ånund Killingtveit. "Hydroelectric Power". In: *Future Energy*. Elsevier, 2014, pp. 453–470. DOI: 10.1016/b978-0-08-099424-6.00021-1.

[3] Dominik Keiner et al. "Powering an island energy system by offshore floating technologies towards 100% renewables: A case for the Maldives". In: *Applied Energy* 308 (Feb. 2022), p. 118360. DOI: 10.1016/j.apenergy.2021.118360.

[4] Gunnar Mork et al. "Assessing the Global Wave Energy Potential". In: *29th International Conference on Ocean, Offshore and Arctic Engineering: Volume 3*. ASMEDC, Jan. 2010. DOI: 10.1115/omae2010-20473.

[5] Kester Gunn and Clym Stock-Williams. "Quantifying the global wave power resource". In: *Renewable Energy* 44 (Aug. 2012), pp. 296–304. DOI: 10.1016/j.renene.2012.01.101.

[6] Nicolas Guillou, George Lavidas, and Georges Chapalain. "Wave Energy Resource Assessment for Exploitation—A Review". In: *Journal of Marine Science and Engineering* 8.9 (Sept. 2020), p. 705. DOI: 10.3390/jmse8090705.

[7] SeWave. *Front End Engineering Design, Tunneled Wave Energy Converter for the Faroe Islands*. Tech. rep. SeWave Ltd., 2005.

[8] Landsverk. *Webpage*. Ed. by Landsverk. Accessed February 27, 2023. URL: https://www.landsverk.fo.

[9] B.A. Niclasen and K. Simonsen. *High resolution wave climate of the Faroe Islands*. Tech. rep. Fróðskaparsetrið, 2012.

[10] G. J. Komen et al. *Dynamics and Modelling of Ocean Waves*. Cambridge University Press, Sept. 1994. DOI: 10.1017/cbo9780511628955.

[11] H. U. Sverdrup and Walter H. Munk and. *Wind, sea and swell : theory of relations for forecasting / by H.U. Sverdrup and W.H. Munk*. U.S. Navy Hydrographic Office, 1947. DOI: 10.5962/bhl.title.38751.

[12] Willard J. Pierson, Gerhard Neuman, and Richard W. James. *Practical Methods for Observing and Forecasting Ocean Waves by Means of Wave Spectra and Statistics. (Reprinted 1971)*. en. 1955. DOI: 10.25607/OBP-985.

[13] Klaus Hasselmann et al. "Measurements of wind-wave growth and swell decay during the Joint North Sea Wave Project (JONSWAP)". In: *Deut. Hydrogr. Z.* 8 (Jan. 1973), pp. 1–95.

[14] G. J. Komen. "Activities of the WAM (Wave Modelling) Group". In: *Oceanology*. Springer Netherlands, 1986, pp. 121–127. DOI: 10.1007/978-94-009-4205-9_15.

[15] The WAMDI Group. “The WAM Model—A Third Generation Ocean Wave Prediction Model”. In: *Journal of Physical Oceanography* 18.12 (Dec. 1988), pp. 1775–1810. ISSN: 0022-3670. DOI: 10.1175/1520-0485(1988)018<1775:TWMTGO>2.0.CO;2.

[16] R. C. Ris, L. H. Holthuijsen, and N. Booji. “A third-generation wave model for coastal regions: 2. Verification”. In: *Journal of Geophysical Research: Oceans* 104.C4 (Apr. 1999), pp. 7667–7681. DOI: 10.1029/1998jc900123.

[17] The WAVEWATCH III® Development Group. *User manual and system documentation of WAVEWATCH III® version 5.16*. Tech. Note 329. 326 pp. + Appendices. NOAA/NWS/NCEP/MMAB, 2016.

[18] DHI. *MIKE 21 Spectral Wave Module, Scientific documentation*. 2017.

[19] Michel Benoit, Frédéric Marcos, and Françoise Becq. “Development of a Third Generation Shallow-Water Wave Model with Unstructured Spatial Meshing”. In: *Coastal Engineering 1996*, pp. 465–478. DOI: 10.1061/9780784402429.037. eprint: https://ascelibrary.org/doi/pdf/10.1061/9780784402429.037. URL: https://ascelibrary.org/doi/abs/10.1061/9780784402429.037.

[20] Arthur Pecher and Jens Peter Kofoed, eds. *Handbook of Ocean Wave Energy*. Springer International Publishing, 2017. DOI: 10.1007/978-3-319-39889-1.

[21] S. H. Salter. “Wave power”. In: *Nature* 249.5459 (June 1974), pp. 720–724. DOI: 10.1038/249720a0.

[22] I. Glendenning. “Ocean wave power”. In: *Applied Energy* 3.3 (July 1977), pp. 197–222. DOI: 10.1016/0306-2619(77)90036-8.

[23] David V. Evans. *Hydrodynamics of Ocean Wave-Energy Utilization IUTAM Symposium Lisbon/Portugal 1985. IUTAM Symposium Lisbon/Portugal 1985*. Springer Berlin Heidelberg, 1986. ISBN: 9783642826665.

[24] S. H. Salter. “World progress in wave energy—1988”. In: *International Journal of Ambient Energy* 10.1 (Jan. 1989), pp. 3–24. DOI: 10.1080/01430750.1989.9675119.

[25] M.T. Pontes et al. “An Atlas of the Wave Energy Resource in Europe”. In: *Journal of Offshore Mechanics and Arctic Engineering* Vol. 118, (Nov. 1996), pp. 307–309. DOI: 10.1115/1.2833921.

[26] Joao Cruz. *Ocean Wave Energy Current Status and Future Prespectives. Current Status and Future Prespectives*. Springer, 2007. ISBN: 9783540748953.

[27] Evangelia Dialyna and Theocharis Tsoutsos. “Wave Energy in the Mediterranean Sea: Resource Assessment, Deployed WECs and Prospects”. In: *Energies* 14.16 (Aug. 2021), p. 4764. DOI: 10.3390/en14164764.

[28] Aurélien Babarit. “Wave Energy Conversion Historical Perspective”. In: *Ocean Wave Energy Conversion: Resource,* Elsevier, 2017, pp. 37–98. DOI: 10.1016/b978-1-78548-264-9.50002-1.

[29] T. V. Heath. “A review of oscillating water columns”. In: *Philosophical Transactions of the Royal Society A: Mathematical, Physical and Engineering Sciences* 370.1959 (Jan. 2012), pp. 235–245. DOI: 10.1098/rsta.2011.0164.

[30] Yoshio Masuda. “Wave-activated generator”. In: *Int. Coll. on the Expositions of the Oceans (Trans.), Bordeaux, France* (1971).

[31] António F. de O. Falcão. “Wave energy utilization: A review of the technologies”. In: *Renewable and Sustainable Energy Reviews* 14.3 (Apr. 2010), pp. 899–918. DOI: 10.1016/j.rser.2009.11.003.

[32] Johannes Falnes. *Ocean Waves and Oscillating Systems*. Cambridge University Press, Apr. 30, 2002. 288 pp. ISBN: 0521017491. URL: https://www.ebook.de/de/product/3895081/johannes_falnes_ocean_waves_and_oscillating_systems.html.

[33] Wanan Sheng. “Wave energy conversion and hydrodynamics modelling technologies: A review”. In: *Renewable and Sustainable Energy Reviews* 109 (July 2019), pp. 482–498. DOI: 10.1016/j.rser.2019.04.030.

[34] Matt Folley. *Numerical Modelling of Wave Energy Converters. State-Of-the Art Techniques for Single WEC and Converter Arrays.* Elsevier Science Technology Books, 2016, p. 306. ISBN: 9780128032107.

[35] António F.O. Falcão and João C.C. Henriques. “Oscillating-water-column wave energy converters and air turbines: A review”. In: *Renewable Energy* 85 (Jan. 2016), pp. 1391–1424. DOI: 10.1016/j.renene.2015.07.086.

[36] M. Rosati, J.C.C. Henriques, and J.V. Ringwood. “Oscillating-water-column wave energy converters: A critical review of numerical modelling and control”. In: *Energy Conversion and Management: X* 16 (Dec. 2022), p. 100322. DOI: 10.1016/j.ecmx.2022.100322.

[37] Francois-Xavier Faÿ et al. “Review of control strategies for oscillating water column wave energy converters”. In: *Proceedings of the 11th European Wave and Tidal Energy Conference*. Sept. 2015.

[38] Nicola Delmonte et al. “Review of Oscillating Water Column Converters”. In: *IEEE Transactions on Industry Applications* (2015), pp. 1–1. DOI: 10.1109/tia.2015.2490629.

[39] Sadegh Khaleghi, Tek Tjing Lie, and Craig Baguley. “An Overview of the Oscillating Water Column (OWC) Technologies: Issues and Challenges”. In: *Journal of Basic &amp Applied Sciences* 18 (Dec. 2022), pp. 98–118. DOI: 10.29169/1927-5129.2022.18.11.

[40] Bingyong Guo and John V. Ringwood. “A review of wave energy technology from a research and commercial perspective”. In: *IET Renewable Power Generation* 15.14 (Oct. 2021), pp. 3065–3090. DOI: 10.1049/rpg2.12302.

[41] O. Malmo and A. Reitan. “Development of the Kvaerner Multiresonant OWC”. In: *Hydrodynamics of Ocean Wave-Energy Utilization*. Springer Berlin Heidelberg, 1986, pp. 57–67. DOI: 10.1007/978-3-642-82666-5_4.

[42] T.W. Thorpe. *A brief review of wave energy. A report produced for UK Department of Trade and Industry*. Report. Department of Trade and Industry, 1999.

[43] A.F. de O.Falcão. “The shoreline OWC wave power plant at the Azores”. In: *Proceedings of the 4th European Wave Energy Conference, Aalborg, Denmark*. 2000.

[44] The Queen’s University of Belfast. *Islay Limpet Wave Power Plant-Publishable Report*. Tech. rep. The Queen’s University of Belfast, 2002.

[45] L.I. Lopez de Aguileta Y. Torre-Enciso I. Ortubia and J. Marqués. “Mutriku Wave Power Plant: from the thinking out to the reality”. In: *Proceedings of the 8th European Wave and Tidal Energy Conference, Uppsala, Sweden*. 2009.

[46] Bárdur Joensen et al. “Hydrodynamic analysis of a one-way energy capture of an oscillating water column wave energy device”. In: *Journal of Energy Reports (In review)* (2022).

[47] AA Wells. “Fluid driven rotary transducer”. In: *British patent spec* 1 (1976), pp. 595–700.

[48] Ivan Andreevich Babintsev. *Apparatus for converting sea wave energy into electrical energy*. US Patent 3,922,739. Dec. 1975.

[49] Fabio Licheri et al. “Wells turbine efficiency improvements: experimental application of a speed control strategy”. In: *Journal of Physics: Conference Series* 2385.1 (Dec. 2022), p. 012132. DOI: 10.1088/1742-6596/2385/1/012132.

[50] Tapas K. Das et al. “Performance improvement of a Wells turbine through an automated optimization technique”. In: *Energy Conversion and Management: X* 16 (Dec. 2022), p. 100285. DOI: 10.1016/j.ecmx.2022.100285.

[51] João S. Alves et al. “Experimental investigation on performance improvement by mid-plane guide-vanes in a biplane-rotor Wells turbine for wave energy conversion”. In: *Renewable and Sustainable Energy Reviews* 150 (Oct. 2021), p. 111497. DOI: 10.1016/j.rser.2021.111497.

[52] Paolo Boccotti. “Comparison between a U-OWC and a conventional OWC”. In: *Ocean Engineering* 34.5-6 (Apr. 2007), pp. 799–805. DOI: 10.1016/j.oceaneng.2006.04.005.

[53] Paolo Boccotti. “Design of breakwater for conversion of wave energy into electrical energy”. In: *Ocean Engineering* 51 (Sept. 2012), pp. 106–118. DOI: 10.1016/j.oceaneng.2012.05.011.

[54] Iván López et al. “Design Selection and Geometry in OWC Wave Energy Converters for Performance”. In: *Energies* 14.6 (Mar. 2021), p. 1707. DOI: 10.3390/en14061707.

[55] Murat Barış Mandev and Abdüsselam Altunkaynak. “Advanced efficiency improvement of a sloping wall oscillating water column via a novel streamlined chamber design”. In: *Energy* 259 (Nov. 2022), p. 124927. DOI: 10.1016/j.energy.2022.124927.

[56] Jens Peter Kofoed and Peter Frigaard. *Hydraulic evaluation of the LEANCON wave energy converter*. 2008.

[57] Luca Martinelli, Paolo Pezzutto, and Piero Ruol. “Experimentally based model to size the geometry of a new OWC device, with reference to the Mediterranean Sea wave environment”. In: *Energies* 6.9 (2013), pp. 4696–4720.

[58] Pierre Benreguig et al. “Modelling Approaches of a Closed-Circuit OWC Wave Energy Converter”. In: *Journal of Marine Science and Engineering* 7.2 (Jan. 2019), p. 23. DOI: 10.3390/jmse7020023.

[59] Pierre Benreguig et al. “Wave-to-Wire Model Development and Validation for Two OWC Type Wave Energy Converters”. In: *Energies* 12.20 (Oct. 2019), p. 3977. DOI: 10.3390/en12203977.

[60] Wave Swell Energy. *https://www.waveswell.com/*. [accessed 23.03.2021].

[61] Alan Fleming et al. “Power Performance Prediction for a Vented Oscillating Water Column Wave Energy Converter with a Unidirectional Air Turbine Power Take-off”. In: *Proceedings of the 12th European Wave and Tidal Energy Conference*.

[62] Nazanin Ansarifard et al. “A radial inflow air turbine design for a vented oscillating water column”. In: *Energy* 166 (Jan. 2019), pp. 380–391. DOI: 10.1016/j.energy.2018.10.068.

[63] “Power performance prediction for a vented oscillating water column wave energy converter with a unidirectional air turbine power take-off”. In: *Proceedings of the 12th European Wave and Tidal Energy Conference*. EWTEC. 2017, pp. 1204–1.

[64] H.G. Tolland and J.F. Walker. “The Economic Analysis of Wave Energy”. In: *Alternative Energy Systems*. Elsevier, 1984, pp. 139–161. DOI: 10.1016/b978-0-08-031639-0.50019-2.

[65] Julia Fernández Chozas. “Technical and Non-Technical Issues towards the Commercialisation of Wave Energy Converters”. In: *Technical and Non-Technical Issues towards the Commercialisation of Wave Energy Converters*. River Publisher, 2013, pp. 1–107. DOI: 10.13052/rp-9788793102538.

[66] S. Astariz and G. Iglesias. “The economics of wave energy: A review”. In: *Renewable and Sustainable Energy Reviews* 45 (May 2015), pp. 397–408. DOI: 10.1016/j.rser.2015.01.061.

[67] Amélie Têtu and Julia Fernandez Chozas. “A Proposed Guidance for the Economic Assessment of Wave Energy Converters at Early Development Stages”. In: *Energies* 14.15 (Aug. 2021), p. 4699. DOI: 10.3390/en14154699.

[68] Bárdur Joensen and Harry B. Bingham. “Economic feasibility study for wave energy conversion device deployment in Faroese waters”. Submitted.

[69] Bárdur Joensen and Harry B. Bingham. “Comparison of a spectral wave model with a fully nonlinear potential flow wave model”. Submitted.

[70] A. P. Engsig-Karup et al. *OceanWave3D; an efficient coastal engineering tool for nonlinear waves.* https://github.com/apengsigkarup/OceanWave3D-Fortran90. Lyngby, Denmark: Technical University of Denmark, 2023.

[71] Bárður Joensen, Bárður A. Niclasen, and Harry B. Bingham. “Wave power assessment in Faroese waters using an oceanic to nearshore scale spectral wave model”. In: *Energy* 235 (Nov. 2021), p. 121404. DOI: 10.1016/j.energy.2021.121404.

[72] Bárdur Joensen, Harry B. Bingham, and Bárdur A. Niclasen. “Evaluation of the power performance of various wave energy conversion concepts for Faroese coastal waters”. In: *Developments in Renewable Energies Offshore*. CRCPress/Balkema, 2021, pp. 96–102. ISBN: 9780367681319.

[73] Bárdur Joensen et al. “Performance predictions of one-way energy capture by an oscillating water column device in Faroese waters”. In: *Proceedings of the 14th European Wave and Tidal Energy Conference*. Ed. by D.M. Greaves. ISSN: 2309-1983. 2021.

[74] M. Rosati et al. “A data-based modelling approach for a vented oscillating water column wave energy converter”. In: *Trends in Renewable Energies Offshore*. Ed. by C. Guedes Soares. Marine Technology and Ocean Engineering Series. Proceedings of the 5th International Conference on Renewable Energies Offshore (Renew 2022). CRC Press, 2023, pp. 339–350. ISBN: 978-1-032-42003-5.

DTU Construct
Section of Fluid Mechanics, Coastal and Maritime Engineering
Technical University of Denmark

Koppels Allé, Bld. 403
DK-2800 Kgs. Lyngby
Denmark
Tlf.: +45 4525 1360
Fax: +45 4525 1961

www.construct.dtu.dk

Febuary 2023

ISBN: 978-87-7475-719-1

DCAMM
Danish Center for Applied Mathematics and Mechanics

Koppels Allé, Bld. 404
DK-2800 Kgs. Lyngby
Denmark
Phone (+45) 4525 4250
Fax (+45) 4525 1961

www.dcamm.dk

DCAMM Special Report No. S327

ISSN: 0903-1685